INVESTIGATION INTO REYNOLDS NUMBER EFFECTS ON A BIOMIMETIC FLAPPING WING

THESIS

Daniel K. Hope, 2d Lt, USAF

AFIT-ENY-MS-16-M-219

DEPARTMENT OF THE AIR FORCE
AIR UNIVERSITY

AIR FORCE INSTITUTE OF TECHNOLOGY

Wright-Patterson Air Force Base, Ohio

DISTRIBUTION STATEMENT A
APPROVED FOR PUBLIC RELEASE; DISTRIBUTION UNLIMITED.

The views expressed in this document are those of the author and do not reflect the official policy or position of the United States Air Force, the United States Department of Defense or the United States Government. This material is declared a work of the U.S. Government and is not subject to copyright protection in the United States.

AFIT-ENY-MS-16-M-219

INVESTIGATION INTO REYNOLDS NUMBER EFFECTS ON A BIOMIMETIC FLAPPING WING

THESIS

Presented to the Faculty

Department of Aeronautics and Astronautics

Graduate School of Engineering and Management

Air Force Institute of Technology

Air University

Air Education and Training Command

in Partial Fulfillment of the Requirements for the

Degree of Master of Science in Aeronautical Engineering

Daniel K. Hope, B.S.A.E.

2d Lt, USAF

March 9, 2016

DISTRIBUTION STATEMENT A
APPROVED FOR PUBLIC RELEASE; DISTRIBUTION UNLIMITED.

AFIT-ENY-MS-16-M-219

INVESTIGATION INTO REYNOLDS NUMBER EFFECTS ON A BIOMIMETIC FLAPPING WING

THESIS

Daniel K. Hope, B.S.A.E.
2d Lt, USAF

Committee Membership:

Lt Col Anthony M. DeLuca, PhD
Chair

Lt Col Michael L. Anderson, PhD
Member

Maj Ryan P. O'Hara, PhD
Member

Abstract

Previous research at the Air Force Institute of Technology has shed light into the stability, control, micro-manufacturing, and aerodynamic performance of a Manduca Sexta inspired biomimetic wing. This research investigated how the nature of the wing changed as a function of Reynolds number by measuring the forces produced by wings with varying characteristic lengths, tested at varying air densities. The base line 50 mm wing span was compared against wings manufactured with 55, 60, 65, and 70 mm spans, while maintaining a constant aspect ratio. Tests were conducted in a sealed vacuum chamber at air densities between 0.5% and 100% of atmospheric pressure.

Increasing the wing span increased the overall weight of the wing, which reduced the 1st natural frequency; and did not result in an increase in vertical force over the baseline 50 mm wing. However; if the decrease in natural frequency corresponding to the increased wing length was counteracted by increasing the thickness of the joint material in the linkage mechanism, vertical force production did increase over the baseline wing planform. Equipped with the more robust flapping mechanism, the 55 mm wing span produced 96% more vertical force at a 26% higher flapping frequency, while the 70 mm wing span produced 188% more vertical force at a 10% lower natural frequency than the baseline wing. Negligible forces and moments were measured at vacuum conditions, where the wing was demonstrating purely inertial motion, revealing the flight forces measured in atmosphere are wholly limited to its interaction with the surrounding air. Lastly, there was clear correlation between Reynolds number and vertical force production, indicating Reynolds number is a suitable parameter to predict the expected lift production for a specific wing design.

Acknowledgements

I would like to thank my thesis advisor, Lieutenant Colonel Anthony DeLuca, for giving me guidance throughout the course of my research. I would also like to thank Major Ryan O'Hara for providing me support, especially regarding the fabrication of the FWMAV and the proper use of the FWMAV lab equipment and instrumentation. Mr. Philip Smith and Mr. Randall Sharp greatly assisted in my research efforts by making a large portion of the flapper assemblies used in this research. Finally, I would like to thank my fellow Second Lieutenants graduating with me from AFIT, especially my fellow classmates from the United States Air Force Academy class of 2014, for nearly two years of shared memories and good times in Dayton.

Daniel K. Hope

Table of Contents

Page

Abstract iv

Acknowledgements v

List of Figures viii

List of Tables xiv

List of Symbols xvi

List of Abbreviations xviii

I. Introduction 1

1.1 Overview 1
1.2 Motivation 2
1.3 Research Challenges For Flapping Wing Micro Air Vehicles 3
1.4 Objectives 4
1.5 Thesis Organization 5

II. Literature Review 6

2.1 Chapter Introduction 6
2.2 Flapping Wing Aerodynamics 6
2.3 Stability and Control 12
2.4 Mechanical Considerations for Biomimicry 14
2.5 Previous AFIT FWMAV Research 17
2.6 Chapter Summary 24

III. Experimental Methodology 25

3.1 Construction of Constant Aspect Ratio, Longer Span Wings 25
3.2 Lab Setup and Instrumentation 29
3.3 Flapper Operationalization 35
3.4 Vacuum Testing 39
3.5 Chapter Summary 43

IV. Results and Analysis 44

4.1 Chapter Introduction 44
4.2 Driving Amplitude and Stroke Angle 44
4.3 Length Modification 47

Page

4.4 4-Bar Linkage Modification . . . 52
4.5 Altered Wings and Linkages . . . 56
4.6 Nano-17 Extension Cord . . . 62
4.7 Vacuum Tests . . . 65
4.8 Near Absolute Vacuum Test . . . 69
4.9 Reynolds Number . . . 73
4.10 Stroke Angle Measurement and Symmetry . . . 78
4.11 Chapter Summary . . . 85

V. Conclusion . . . 86

5.1 Summary . . . 86
5.2 Research Conclusions . . . 88
5.3 Significant Contributions . . . 91
5.4 Recommendations for Future Research . . . 93

VI. Appendix . . . 94

Bibliography . . . 110

List of Figures

Figure		Page
1.	Differences in Speed and Weight Between Aircraft [10]	7
2.	Inclined Stroke Plane Angle (β) [7]	8
3.	Horizontal Stroke Plane Angle (β) [7]	9
4.	Numerical Visualization of LEV Structure [20]	11
5.	Top Left: Amplitude Modulation; Top Right: Bias Modulation; Bottom: Split-Cycle Parameter [2]	13
6.	Drive Mechanism of a Primitive FWMAV Vehicle [4]	14
7.	4-Bar Linkage Design [16]	15
8.	Passive Rotation Joint Schematic [19]	16
9.	Locations of Cross-Sectional Cuts Made to Measure Venation Dimensions Across the Wing [18]	18
10.	Nanoindentation Locations for Measuring Membrane Properties [18]	19
11.	Flapper Base Fabrication Process [18]	20
12.	Biological *Manduca Sexta* Wing vs Biomimetic *Manduca Sexta* Wing	21
13.	30, 45, and 60 Degree Angle Stops Used to Modify the Angle of Attack [5]	21
14.	PIV Images of LEV Formation and Shedding [5]	22
15.	BEM Mean Aerodynamic Coefficients For Various Angle Stops [5]	23
16.	CAD Geometry of 50, 55, 60, 65, and 70 mm Wings	25
17.	CAD Passive Rotation Joints of 50, 55, 60, 65, and 70 mm Wings	26

Figure Page

18. Wing Geometries For Separate Fabrication Steps. 1 and 2 are for Carbon Fiber, 3 is for Kapton, and 4 is for Combined Carbon Fiber, Kapton, and Carbon Fiber 26

19. Four Separate CAD Images Overlaid to Ensure Synchronous Alteration 27

20. Comparison Between R, Used to Calculate L, and R_2, Used To Calculate V 28

21. The 50, 55, 60, 65, and 70 mm Wings 29

22. Nano-17 Coordinate System [5] 30

23. Nano-17 and optoNCDT Placement 31

24. Displacement Sensor Calibration Rig 32

25. Lab Instrumentation Setup 33

26. NI Box 35

27. GUI Input for *Chirp* 36

28. GUI Input for *Autotune* 37

29. Vacuum Chamber 40

30. Pressure Display, Release Valve, and Extension Cords 41

31. Vacuum Pump 42

32. Driving Amplitude vs Stroke Angle of 50 mm Wing Flapping at 17.29 Hz 45

33. Driving Amplitude and Stroke Angle vs Forces of 50 mm Wing Flapping at 17.29 Hz 46

34. Driving Amplitude and Stroke Angle vs Moments of 50 mm Wing Flapping at 17.29 Hz 46

35. Driving Amplitude and Stroke Angle vs Power of 50 mm Wing Flapping at 17.29 Hz 47

Figure Page

36. Forces of 50 mm Wing Flapping at 17.29 Hz, 55 mm Wing Flapping at 15.72 Hz, and 60 mm Wing Flapping at 9.44 Hz 49

37. Moments of 50 mm Wing Flapping at 17.29 Hz, 55 mm Wing Flapping at 15.72 Hz, and 60 mm Wing Flapping at 9.44 Hz 50

38. Power of 50 mm Wing Flapping at 17.29 Hz, 55 mm Wing Flapping at 15.72 Hz, and 60 mm Wing Flapping at 9.44 Hz 51

39. Forces of 50 mm Wing with 4-Bar Linkage Kapton Thicknesses of 12.5 μm Flapping at 17.29 Hz, 25 μm Flapping at 22 Hz, and 50 μm Flapping at 25.9 Hz 53

40. Moments of 50 mm Wing with 4-Bar Linkage Kapton Thicknesses of 12.5 μm Flapping at 17.29 Hz, 25 μm Flapping at 22 Hz, and 50 μm Flapping at 25.9 Hz 54

41. Power of 50 mm Wing with 4-Bar Linkage Kapton Thicknesses of 12.5 μm Flapping at 17.29 Hz, 25 μm Flapping at 22 Hz, and 50 μm Flapping at 25.9 Hz 55

42. Angle of Attack Comparison for 12.5 μm Linkage (Top) and 50 μm Linkage (Bottom) 56

43. Forces: 50 mm 17.29 Hz Wing with 12.5 μm Linkage, 55 mm 22.794 Hz Wing With 50 μm Linkage and 45 Degree Angle Stop, 60 mm 19.65-20.44 Hz Wing with 50 μm Linkage, 65 mm 11 Hz Wing with 25 μm Linkage, 70 mm 9.43 Hz Wing with 25 μm Linkage, 70 mm 15.72 Hz Wing with 50 μm Linkage 59

44. Moments: 50 mm 17.29 Hz Wing with 12.5 μm Linkage, 55 mm 22.794 Hz Wing With 50 μm Linkage and 45 Degree Angle Stop, 60 mm 19.65-20.44 Hz Wing with 50 μm Linkage, 65 mm 11 Hz Wing with 25 μm Linkage, 70 mm 9.43 Hz Wing with 25 μm Linkage, 70 mm 15.72 Hz Wing with 50 μm Linkage 60

Figure Page

45. Power: 50 mm 17.29 Hz Wing with 12.5 μm Linkage, 55 mm 22.794 Hz Wing With 50 μm Linkage and 45 Degree Angle Stop, 60 mm 19.65-20.44 Hz Wing with 50 μm Linkage, 65 mm 11 Hz Wing with 25 μm Linkage, 70 mm 9.43 Hz Wing with 25 μm Linkage, 70 mm 15.72 Hz Wing with 50 μm Linkage 61

46. Difference in Vertical Force, Yaw Moment, Side Force, Pitch Moment, Axial Force, and Roll Moment of 50 mm Wing With and Without an Extension Cord, with the Extension Cord Value Subtracted From the Non-Extension Cord Value 64

47. Forces of 50 mm Wing at 100% atm and 17.29 Hz, 85% atm and 18.84 Hz, 70% atm and 18.86 Hz, 55% atm and 16.51 Hz, 40% atm and 18.08 Hz, and 25% atm and 18.05 Hz 66

48. Moments of 50 mm Wing at 100% atm and 17.29 Hz, 85% atm and 18.84 Hz, 70% atm and 18.86 Hz, 55% atm and 16.51 Hz, 40% atm and 18.08 Hz, and 25% atm and 18.05 Hz 67

49. Power of 50 mm Wing at 100% atm and 17.29 Hz, 85% atm and 18.84 Hz, 70% atm and 18.86 Hz, 55% atm and 16.51 Hz, 40% atm and 18.08 Hz, and 25% atm and 18.05 Hz 68

50. Comparison of Forces of 50 mm Wing at 100% atm and 17.29 Hz, 0.57% atm and 17.29 Hz, and 0.57% atm and 17.29 Hz with Altered Y-Axis Range 70

51. Comparison of Moments of 50 mm Wing at 100% atm and 17.29 Hz, 0.57% atm and 17.29 Hz, and 0.57% atm and 17.29 Hz with Altered Y-Axis Range 71

52. Comparison of Power of 50 mm Wing at 100% atm and 17.29 Hz, 0.57% atm and 17.29 Hz, and 0.57% atm and 17.29 Hz with Altered Y-Axis Range 72

53. Reynolds Number Data of 50, 55, and 60 mm Wings with Original Linkages. Vertical Force is Shown on the Left, and Vertical Force is Shown on the Right 74

Figure Page

54. Reynolds Number Data of 50 mm Wing with Three Separate Linkages. Vertical Force is Shown on the Left, and Vertical Force is Shown on the Right 75

55. Reynolds Number Data of Wings of Various Sizes and Linkages at Atmospheric Pressure. Vertical Force is Shown on the Left, and Vertical Force is Shown on the Right 75

56. Reynolds Number Data of Vacuum Tests. Vertical Force is Shown on the Left, and Vertical Force is Shown on the Right 76

57. Reynolds Number Data of All Test Points. Vertical Force is Shown on the Left, and Vertical Force is Shown on the Right 77

58. Reynolds Number vs Vertical Force for All Test Cases Except the 60 mm Wing With the 50 μm Linkage and 50 mm Wing With the 50 μm Linkage 77

59. Driving Amplitude vs Optical and Kinematic Stroke Angle of 50 mm 17.29 Hz Wing, 55 mm 15.72 Hz Wing, and 60 mm 9.44 Wing 80

60. Driving Amplitude vs Optical and Kinematic Stroke Angle of 50 mm Wing with 12.5 μm Thick Kapton Linkage Flapping at 17.29 Hz, 25 μm Thick Kapton Linkage Flapping at 22 Hz, and 50 μm Thick Kapton Linkage Flapping at 25.9 Hz 81

61. Driving Amplitude vs Optical and Kinematic Stroke Angle: 50 mm 17.29 Hz Wing with 12.5 μm Linkage, 55 mm 22.794 Hz Wing With 50 μm Linkage and 45 Degree Angle Stop, 60 mm 19.65-20.44 Hz Wing with 50 μm Linkage, 65 mm 11 Hz Wing with 25 μm Linkage, 70 mm 9.43 Hz Wing with 25 μm Linkage, 70 mm 15.72 Hz Wing with 50 μm Linkage 82

62. Driving Amplitude vs Optical and Kinematic Stroke Angle: 50 mm Wing at 100% atm and 17.29 Hz, 85% atm and 18.84 Hz, 70% atm and 18.86 Hz, 55% atm and 16.51 Hz, 40% atm and 18.08 Hz, and 25% atm and 18.05 Hz 83

Figure Page

63. Driving Amplitude vs Optical and Kinematic Stroke Angle of 50 mm Wing at 100% atm and 17.29 Hz, 0.57% atm and 17.29 Hz, and 0.57% atm and 17.29 Hz with Altered Y-Axis Range 84

List of Tables

Table		Page
1.	R vs. R_2 Length	28
2.	Wing Length, Wing Mass, and Natural Frequency of Wings With an Aspect Ratio of 14.42	48
3.	Wing Length, Wing Mass, and Natural Frequency of Modified Wing Designs With an Aspect Ratio of 14.42	57
4.	Vertical Force and Power Consumption of Original Design vs Two Best Improved Designs at 105 Degree Stroke Angle	62
5.	Driving Amplitude, Bias, and Stroke Angle of 50 mm Wing with 12.5 μm Kapton 4-Bar Linkage	94
6.	Driving Amplitude, Bias, and Stroke Angle of 50 mm Wing with 25 μm Kapton 4-Bar Linkage	95
7.	Driving Amplitude, Bias, and Stroke Angle of 50 mm Wing with 50 μm Kapton 4-Bar Linkage	96
8.	Driving Amplitude, Bias, and Stroke Angle of 55 mm Wing with 12.5 μm Kapton 4-bar Linkage	97
9.	Driving Amplitude, Bias, and Stroke Angle of 55 mm Wing with 50 μm Kapton 4-Bar Linkage	98
10.	Driving Amplitude, Bias, and Stroke Angle of 60 mm Wing with 12.5 μm Kapton 4-Bar Linkage	99
11.	Driving Amplitude, Bias, and Stroke Angle of 60 mm Wing with 50 μm Kapton 4-Bar Linkage	100
12.	Driving Amplitude, Bias, and Stroke Angle of 65 mm Wing with 25 μm Kapton 4-Bar Linkage	101
13.	Driving Amplitude, Bias, and Stroke Angle of 70 mm Wing with 25 μm Kapton 4-Bar Linkage	102
14.	Driving Amplitude, Bias, and Stroke Angle of 70 mm Wing with 50 μm Kapton 4-Bar Linkage	103

Table Page

15. Driving Amplitude, Bias, and Stroke Angle of Wing at 85% of Atmospheric Pressure 104

16. Driving Amplitude, Bias, and Stroke Angle of wing at 70% of Atmospheric Pressure 105

17. Driving Amplitude, Bias, and Stroke Angle of Wing at 55% of Atmospheric Pressure 106

18. Driving Amplitude, Bias, and Stroke Angle of Wing at 40% of Atmospheric Pressure 107

19. Driving Amplitude, Bias, and Stroke Angle of Wing at 25% of Atmospheric Pressure 108

20. Driving Amplitude, Bias, and Stroke Angle of Wing at 0.57% of Atmospheric Pressure 109

List of Symbols

Symbol		Page
Re	Reynolds Number	7
L	Characteristic Length	7
ρ	Air Density	7
V	Wingtip Velocity	7
μ	Dynamic Viscosity	7
β	Stroke Plane Angle	8
θ	Elevation Angle	10
ϕ	Wing Position Angle	10
α	Angle of Attack	10
Φ	Stroke Angle	10
f	Flapping Frequency	10
R	Wing Length	10
AR	Aspect Ratio	10
A	Driving Amplitude	13
η	Bias	13
τ	Split-Cycle Parameter	13
δ	Piezo Tip Displacement	14
T	Transmission Ratio	15
θ	Phase Shift	34
w_n	Natural Frequency	35
k_{eq}	Wing Stifness	35
m_{eq}	Wing Mass	35

Symbol		Page
q	Dynamic Pressure	73
S	Planform Area	73

List of Abbreviations

Abbreviation		Page
FWMAV	Flapping Wing Micro Air Vehicles	1
MAV	Micro Air Vehicles	1
AFIT	Air Force Institute of Technology	1
DoD	Department of Defense	2
ISR	Intelligence Surveillance Reconnaissance	3
LEV	Leading Edge Vortex	11
BEM	Blade Element Model	12
BABM	Biharmonic Amplitude and Bias Modulation	12
DoF	Degrees of Freedom	14
PZT	Piezo Electric Actuators	14
CAD	Computer Aided Design	20
PIV	Particle Image Velocimetry	21
CKC	Carbon Fiber, Kapton, and Carbon Fiber	27
fps	frames per second	30
NI	National Instruments	33
USB	Universal Serial Bus	34
GUI	Graphical User Interface	35
Hz	Hertz	36
FRF	Frequency Response Function	36
mg	milligrams	48

INVESTIGATION INTO REYNOLDS NUMBER EFFECTS
ON A BIOMIMETIC FLAPPING WING

I. Introduction

1.1 Overview

The field of Flapping Wing Micro Air Vehicles (FWMAV) is relatively understudied and underdeveloped in the greater discipline of aeronautical engineering. The needs of the Department of Defense and industry over the past century have necessarily entailed the design of large fixed-wing or rotary aircraft capable of carrying people and cargo over long distances. Likewise, the technology in this area has largely matured, as can be demonstrated by the continued use of airframes which were originally designed in the 1950s and 1960s. However, Micro Air Vehicles (MAV) present a promising field for future application. Bird or insect sized aircraft have several advantages. MAVs are much more maneuverable, are much harder to detect, and are much smaller than conventional aircraft. This leads to several promising niche mission uses.

The immature nature of flapping wing technology means there are several potential avenues of inquiry for researchers to pursue. Past researchers at the Air Force Institute of Technology (AFIT) made the decision to look at one specific design: *Manduca Sexta*, which is a species of hawkmoth. *Manduca Sexta* is commonly used in research in various disparate fields, primarily due to the convenience of growing and rearing such insects in a laboratory environment. Focusing research on the blueprint of this one specific type of insect encourages a more focused and productive research effort

towards the final goal of fielding FWMAVs.

1.2 Motivation

The United States Armed Forces possess a global ability to project force, which has never before been seen in history. This military edge, which stands as a cornerstone of American strength, is driven largely by the technological advantage the US military has over its adversaries. The United States Air Force in particular, relies heavily on innovation to provide global power. This technological exists with the help of a constant development of new innovative technologies, which can could further improve the capabilities of the Air Force. In such an environment MAVs stand as a new potential cornerstone of future air power.

Flapping wing micro air vehicles are a continuation of the trend in recent decades of the DoD relying more heavily on unmanned systems. The Department of Defense Unmanned Systems Integrated Roadmap lists several key areas in which unmanned systems hold an advantage over manned systems, to include "long-duration undertakings with mundane tasks that are ill suited for manned systems", missions which "have the potential to unnecessarily expose personnel to hazardous conditions", and "capabilities that are inherently dangerous" [17]. MAVs fit deeply into this paradigm, offering further potential advantages, to include a smaller logistics footprint, augmentation to existing weapons systems, delivering capabilities to smaller units which typically do not have advanced technology at their disposal, and several tactical applications in the asymmetric battlefield typified by the recent conflicts throughout the Middle East [11]. The potential advantages MAVs offer on the battlefield make them a good candidate for investigation in the continuous art of military innovation.

1.3 Research Challenges For Flapping Wing Micro Air Vehicles

Flapping wing flight and miniturization are two related, but distinct engineering challenges for FWMAV design. As previously stated, throughout aviation history, the focus in research, production, and operation has been on fixed and rotary wing aircraft weighing at least in the thousands of kilograms. As a result, the actual science behind the workings of such lift mechanisms has become canon within the aeronautics discipline. The relatively new innovation of FWMAVs provides unique opportunities but also involves several engineering challenges inherent in any immature novel technological field of study.

First, the small size of FWMAVs presents several challenges. The Reynolds number, used to describe the ratio of inertial to viscous forces in a flow field, is consistently lower in Micro Air Vehicles, due to low velocities and short characteristic lengths. This separates the flow characteristics of MAVs from that of aircraft in "conventional" flight conditions. The low absolute value of the lift and thrust generated in MAVs makes the issue of reducing weight extremely critical. Optimizing the structures, selecting the lightest available materials, which still fulfill other design requirements, and leaving enough excess lift for the attachment of a payload become important issues. Additionally, the inherent limitations of small energy sources present a problem with autonomous flight. A MAV cannot carry heavy fuels, engines, or batteries like conventional aircraft. However, small batteries in their current state do not store enough energy for a MAV to operate for extended periods of time. MAVs also must carry miniturized optical systems for control and Intelligence Surveillance Reconnaissance (ISR) purposes.

Second, engineering challenges exist with operationalizing the flapping mechanism itself. This method of lift and propulsion generation has not been extensively used in contrast with the pervasive use of conventional mechanisms. Flapping wings also

present a control challenge. In recent decades more and more aircraft are "fly-by-wire", in that they are ultimately controlled by computer algorithms rather than the simple mechanical input of a pilot. Stability and control is an entire sub-field within the discipline of aeronautics. Flapping wings are inherently different from fixed-wings in many ways, which leads to a need to reexamine the issue of designing algorithms which provide sufficient control, static stability, and dynamic stability for both autonomous and human-operated flight.

1.4 Objectives

Previous research at AFIT and other institutions have already answered many of the important fundamental questions regarding FWMAV flight. The big-picture understanding of the flapping wing aerodynamics, open-loop and closed-loop control, and fabrication of the flapping mechanism and wings has been explored by previous students. However, within these domains various details remain which must be clearly identified, verified, and tested before a flight-worthy FWMAV is ready to execute missions for the Air Force and Department of Defense.

The objective of this research is to gain further understanding of the aerodynamics of the *Manduca Sexta* wing by measuring the performance of the wing in variable air density tests and with varying wing spans. This will assist in illuminating the effects of Reynolds number scaling on the aerodynamic performance of the wing, determine whether directly scaling the wing to larger sizes will be effective in generating larger lift forces, and determine the power requirements and force and moment response of the flapper assembly under purely inertial motion.

1.5 Thesis Organization

The thesis will be organized by chapter. Chapter II examines the fundamentals of flapping wing aerodynamics, controls, and design and also reviews previous research conducted at AFIT. Chapter III examines the methodology, to include wing and flapper construction, instrumentation, and experimental setup. Chapter IV details, explains, and interprets the obtained experimental results. Chapter V will summarize the results, present the major contributions made in the research process, and offer recommendations for future work.

II. Literature Review

2.1 Chapter Introduction

The following chapter will consist of a summary of the FWMAV technology as well as a review of past literature pertaining to the research at hand. This will include an examination of the fundamentals of FWMAV flight, to include the aerodynamics of flapping wing flight, the stability and control of FWMAVs, and the mechanical construction of a typical FWMAV. There will also be a review of the research done recently at AFIT regarding these topics.

2.2 Flapping Wing Aerodynamics

One difference between conventional flight and flapping wing flight is the contrast in Reynolds number between the two regimes. However, as Figure 1 shows, flapping wing flight itself is not a singular phenomena, in the sense that flight conditions can vary greatly between two separate flapping wing designs. In nature, winged animals can range in size from small insects, such as gnats and fruit flies, to large soaring birds such as eagles, condors, and the albatross. One could intuitively surmise there are appreciable differences in flight characteristics between animals of such different size and wing configurations.

Ellington discusses the differences in aerodynamics based on Reynolds number [6]. The Reynolds number, shown in Equation 1, describes the ratio of inertial forces to viscous forces affecting an aircraft.

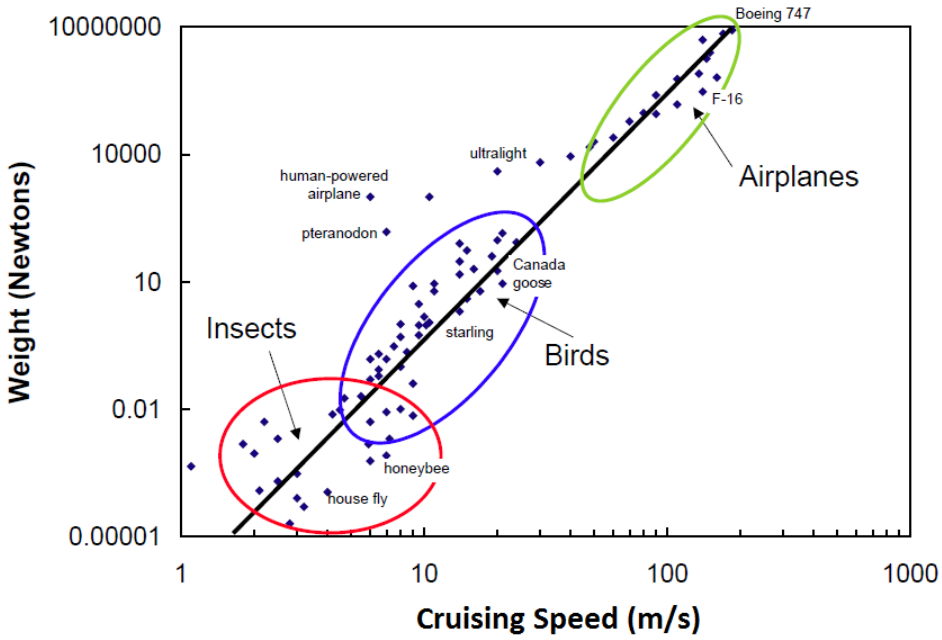

Figure 1. Differences in Speed and Weight Between Aircraft [10]

$$Re = \frac{\rho V L}{\mu} \tag{1}$$

ρ = air density

V = velocity

L = characteristic length

μ = dynamic viscosity

Higher Reynolds numbers, signifying turbulent flying conditions, occur in aircraft operating in high density (ρ), high velocity (V), and low viscosity (μ) environments. Furthermore, aircraft with a longer characteristic length (L) tend to operate in high Reynolds number conditions. The Reynolds number also has the added benefit of acting as a measure of similarity between flows. Although an equal Reynolds number does not guarantee similar flow, it does assist in comparisons such as testing smaller scale models of aircraft in wind tunnels.

Ellington roughly divides flapping wing flight between turbulent regimes, characteristic of most birds, and laminar regimes involving strong vortices, which are characteristic of most insects. Despite both consisting of flapping motion, these two flight regimes must be approached as distinct phenomena from a research standpoint. Ellington's research shows large insects reach Reynolds numbers of 10,000. At this point turbulence begins, which completely destroys the insect flight dynamics at a Reynolds number of 20,000. This low Reynolds number regime encompasses fliers of up to 20 grams. Anything greater than this Reynolds number and mass range is beyond the scope AFIT's research effort [6].

Alternatively, flapping flight can further be differentiated based on wing kinematics [7]. Birds, bats, and a few insects have an inclined stroke plane angle (β). The stroke plane describes the angle between the horizontal and the mean plane along which the chord travels. Inclined stroke plane flight entails a flapping motion in which the wings flex on the upstroke, as seen in Figure 2.

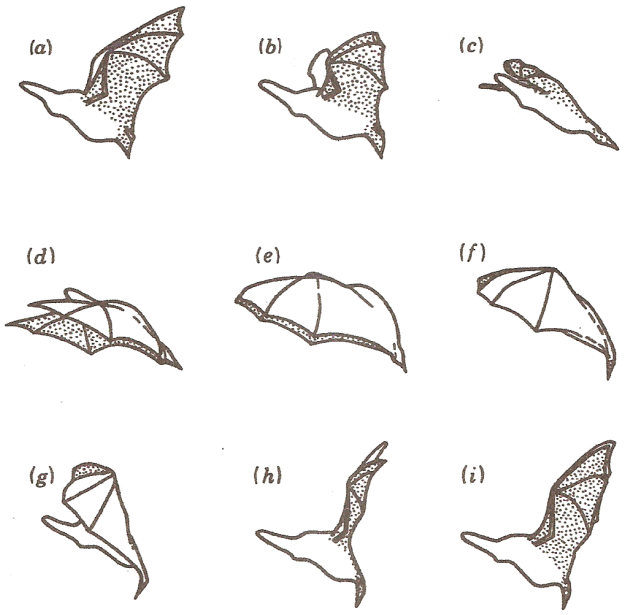

Figure 2. Inclined Stroke Plane Angle (β) [7]

Hummingbirds and the vast majority of insects have a horizontal stroke plane. These wings flap in a figure eight pattern in which the wings rotate a large amount. Figure 3 shows the flapping of a wing with a horizontal stroke plane.

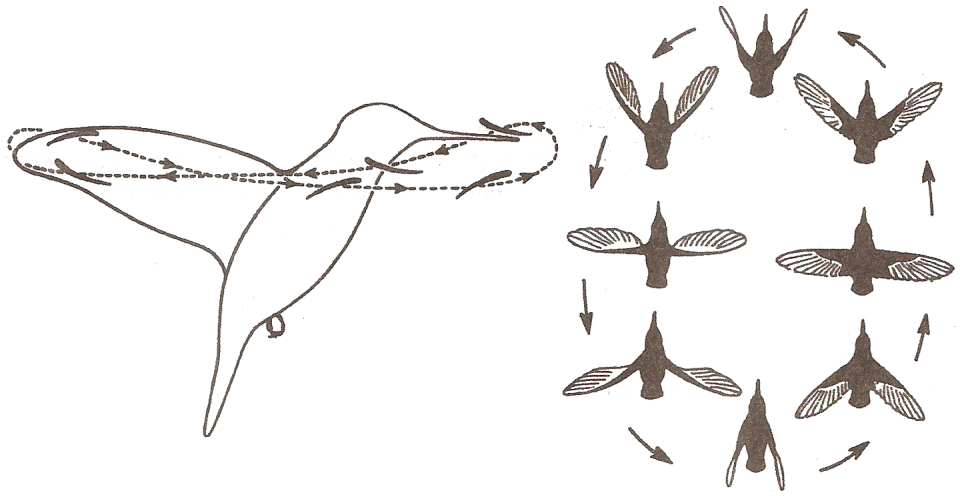

Figure 3. Horizontal Stroke Plane Angle (β) [7]

Ellington focused particularly on the aerodynamics of hovering insect flight [7, 8, 9]. In hovering flight the lift force is exactly equal and opposite to the weight of the insect, with no directional force or motion. Because of the simplicity of this flight condition, understanding the nature of hovering is a natural starting point in understanding flapping wings.

The wing movement of a horizontal stroke plane wing consists of four distinct phases [8]. The wing beats in one direction, and then at the end of the half stroke, it undergoes a rotation along the longitudinal axis called supination. The wing then flaps in the other direction, and then at the end of the half stroke, it undergoes another rotation called pronation. The two rotational movements occur predominantly during a period of rapid acceleration, and low wing velocity at the end of the upstroke and the downstroke. The pronation and supination at the end of each half stroke, combined with the horizontal flapping motion, ensures the wing's leading edge moves into the

relative wind during each half stroke [7]. All together this movement, as previously stated, resembles a figure eight pattern. Although this motion is complicated, it can be described with three kinematic angles. These are the elevation angle (θ), the wing position angle (ϕ), and the angle of attack (α). The elevation angle is the angle between the mean chord and the stroke plane angle. The wing position angle describes the position of the wing along the stroke plane at a specific moment. The angle of attack is the angle between the mean chord of the wing and the relative wind. The angle between stroke angle position at pronation and supination is the stroke angle (Φ), which describes the amplitude of the flapping motion.

Conn [3] presents a modified Reynolds number for flapping wings, first by defining the velocity as the wingtip velocity, shown.in Equation 2:

$$\bar{V}_{tip} = 2\Phi f R \tag{2}$$

The flapping frequency (f) describes the number of times the wing flaps per second, while the wing length (R) describes the length of one wing from the base to the tip. Conn defines the characteristic length as the mean chord, shown below:

$$L = \frac{2R}{\text{Æ}R} \tag{3}$$

This leads to the following reformulated Reynolds number equation:

$$Re = \frac{4\rho\phi f R^2}{\mu \text{Æ}R} \tag{4}$$

The assumption of quasi-steady flow postulates the forces produced by a moving wing are identical to the forces produced by an identical stationary wing at each particular position, suggesting steady state aerodynamics can be used to predict unsteady behavior. Researchers have found this assumption could not explain the lift

generated by flapping wings, suggesting various unsteady phenomena are responsible for the production of lift. Four particular mechanisms were identified, which were the clap-and-fling, leading edge vortices, pitching-up rotation, and wake-capturing [20].

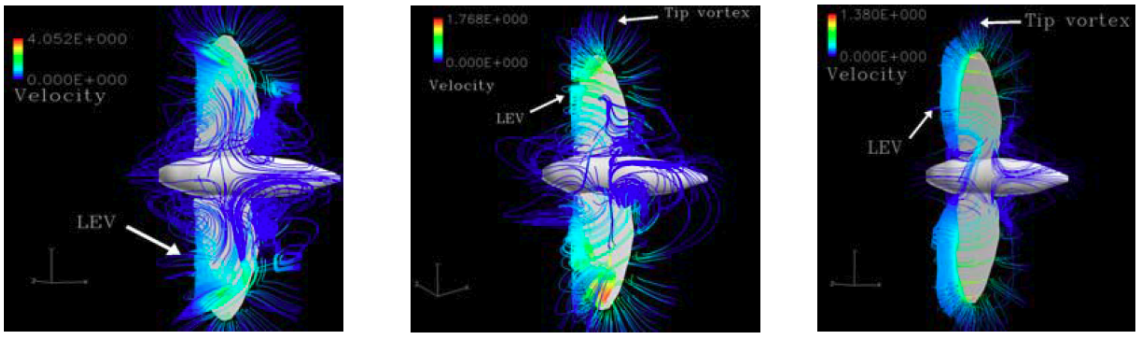

Figure 4. Numerical Visualization of LEV Structure [20]

Of these, the Leading Edge Vortex (LEV), shown in Figure 4, has been studied at length because it greatly contributes to the lift of *Manduca Sexta* wings. The existence of the LEV on the *Manduca Sexta* has been visually analyzed both with live specimens [23], and with the AFIT designed biomimetic wing [5]. The LEV consists of a vortex with appreciable span-wise flow held in a roughly stable position at the leading edge of the wing during the upstroke and downstroke. At pronation and supination, the vortex is shed, after which a new vortex is quickly formed. The LEV causes a low pressure area above the wing which delays the onset of stall. The LEV also increases circulation and increases the apparent camber of the wing from the perspective of the relative wind [5]. The development and formation of the LEV provides an unsteady mechanism through which the Manduca Sexta can produce greater lift than the quasi-steady model would indicate [5].

2.3 Stability and Control

The stability and control of insects is also a vital area of continued research. The ability to measure the stability of insects has proven to be challenging. The control mechanisms insects use to maneuver in flight are impractical to directly measure.

Stable flight has been demonstrated on tailed FWMAVs [4]. However, this stability depends on the flow of air over the tail, and thus limits such vehicles from certain types of flight, such as hovering or backwards flight. Most insects do not make use of any sort of horizontal or vertical structures aside from their wings, which suggests the nature of their stability is entirely different from that of birds or fixed wing aircraft.

Researchers originally assumed a quasi-steady Blade Element Model (BEM) was sufficient to characterize flapping wing flight. Blade element theory is a method of analyzing the forces produced by propellers or helicopter rotors. In BEM, the blade is divided into several smaller cross sections, whose constituent forces are integrated to determine the overall forces caused by the blade. Some research has suggested there are appreciable similarities between flapping wing flight and rotary flight, suggesting a quasi-steady blade element model may be appropriate [14].

The quasi-steady blade element analysis makes two major assumptions; first, the unsteady effects of flapping can be ignored, and second, any side forces produced can also be ignored. However, research shows quasi-steady blade element theory under-predicts the performance of flapping wing flight, which suggests the simplifying assumptions are not accurate. Flapping wings have both a number of unsteady effects, as well as small, but measurable side forces. Although quasi-steady blade element theory was a good first order approximation, it is clear this model needs to be further modified for FWMAV use.

Anderson [1] utilized a control technique known as Biharmonic Amplitude and Bias Modulation (BABM) which aims to control the motion of the wing by varying

the key parameters which determine the wing motion. A sinusoidal electrical signal is utilized to flap the wing. The driving amplitude (A) modifies the amplitude of the sinusoidal signal, and thus modifies the stroke angle of the wing. The bias (η) offsets the driving amplitude value in either the positive or negative direction, and thus shifts the wing stroke angle along the stroke plane without changing the total stroke angle. The split-cycle parameter (τ) increases the flapping frequency of the wing for one portion of the sinusoidal signal, and thus allows the upstroke and downstroke to have distinct velocities [1]. Figure 5 shows how the three parameters alter the sinusoidal signal used to move the wing.

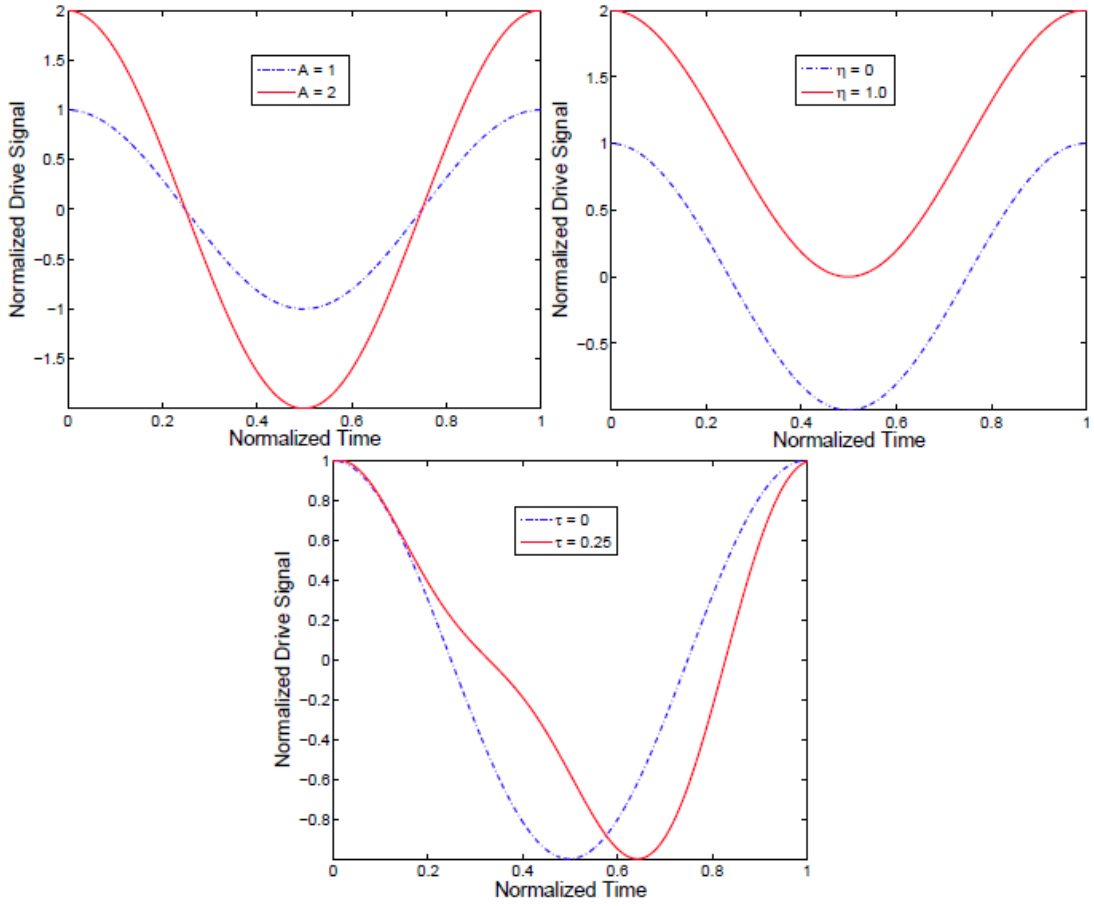

Figure 5. Top Left: Amplitude Modulation; Top Right: Bias Modulation; Bottom: Split-Cycle Parameter [2]

Anderson's research has shown that BABM can control the flight of a flapping wing vehicle in five separate Degrees of Freedom (DoF).

2.4 Mechanical Considerations for Biomimicry

Extensive research has been conducted in replicating the flapping motion of an insect. Insects use their muscular systems to flap their wings. However, the mechanical analogue to this was difficult for researchers to replicate. Past researchers used various kinds of engines, motors, and gears to create flapping motion, such as the example seen in Figure 6 [4, 12].

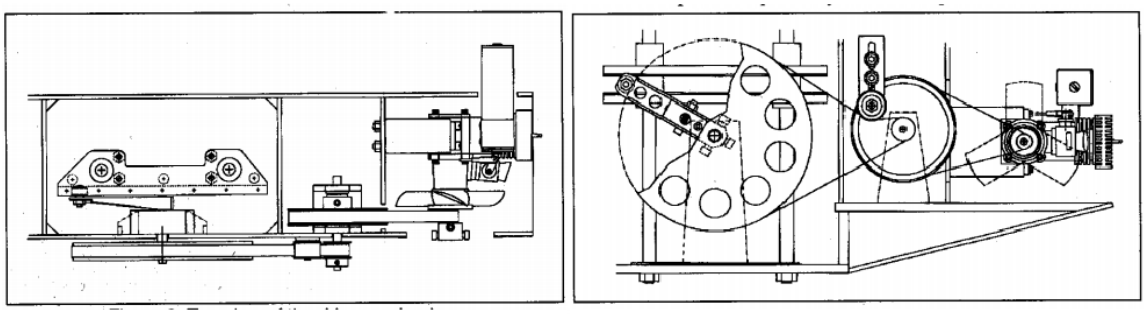

Figure 6. Drive Mechanism of a Primitive FWMAV Vehicle [4]

However, these mechanisms are heavy and unwieldy compared to their natural analogues. Moreover, most of these mechanisms were only capable of flapping two wings in symmetry, thus precluding any control mechanism based on asymmetric flapping. In contrast, Piezo Electric Actuators (PZT) have proven to be better for creating flapping motion [13]. PZTs have several advantages for FWMAV use, which include their lighter weight compared to previous mechanisms, and their ability to easily produce oscillatory motion in response to an electric signal. Wood designed a 4-bar linkage which transmits the approximately linear motion at the tip of the PZT (δ) into angular motion of the wing. Figure 7 demonstrates the design of the 4-bar linkage [24]. The 4-bar linkage consists of four segments, labeled L_1, L_2, L_3, and L_4.

The stroke angle is determined through the following equation.

$$\phi = -\frac{\pi}{2} + arccos[(L_3^2 + (L_1 + L_2 - L_4 - \delta)^2 + L_3^2 + (L_2 - L_4)^2 - L_1^2) \\ (2\sqrt{L_3^2 + (L_2 - L_4)^2}\sqrt{L_3^2 + (L_1 + L_2 - L_4 - \delta)^2})^{-1}] \\ + arctan(\frac{L_3}{L_1 + L_2 - L_4 - \delta}) + arctan(\frac{L_2 - L_4}{L_3}) \tag{5}$$

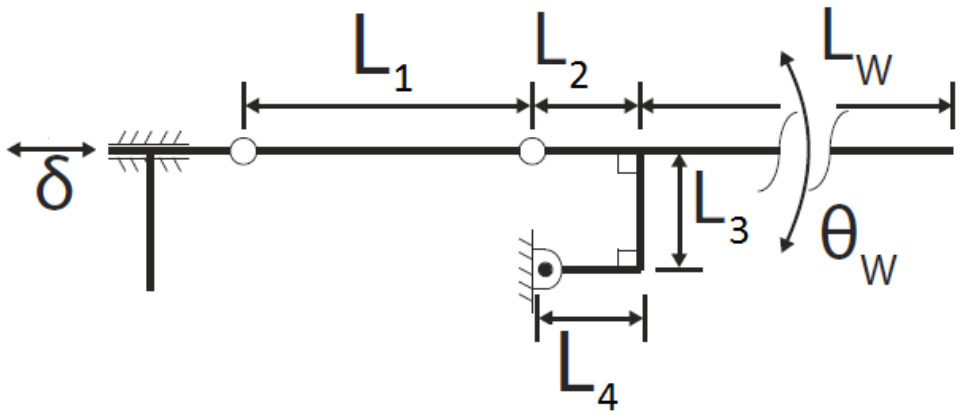

Figure 7. 4-Bar Linkage Design [16]

The L_2 and L_4 linkage are of equal length and held opposite of each other. They are both perpendicular to L_3. There are three free joints. One joint is attached to L_4, one joint links L_1 to L_2, and one joint links L_1 to the translating material attached to the tip of the piezo. The transmission ratio, which describes the ratio of stroke angle to displacement angle, is shown in the equation below. L_3 linkage directly determines the total stroke angle for a given piezo displacement.

$$T \approx \frac{1}{L_3} \tag{6}$$

Whitney outlined the use of passive rotation to simulate the four-step flapping movement of the wing [22]. With passive rotation, a flexible rotation joint attaches the wing to the 4-bar linkage, allowing the wing's angle of attack to change as a

result of the flapping motion. At the end of the stroke the kinetic energy of the wing is transferred into motion about the joint, thus enabling pronation and supination. Passive rotation greatly simplifies the flapping mechanism, as it enable a wing to operate with a single degree of freedom. Figure 8 shows a schematic of a passive rotation joint, while the equation following demonstrates the torsional stiffness of the joint.

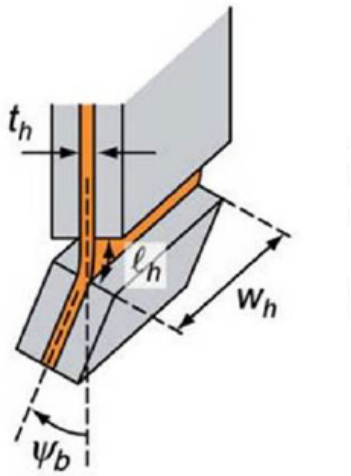

Figure 8. Passive Rotation Joint Schematic [19]

$$G = \frac{E_h w_h {t_h}^3}{12 l_h} \tag{7}$$

G (N/radian^{-1}) is the torsional stiffness of the rotation joint. The stiffness of the passive rotation joint must be properly modulated. An excessively stiff joint will fail to rotate, causing the wing to paddle rather than flap. A joint of insufficient stiffness will rotate chaotically, instead of pronating or supinating at the end of each stroke.

2.5 Previous AFIT FWMAV Research

Anderson and Lindholm investigated the relatively unexplored area of active control of flapping wing vehicles [1, 16]. Insect-sized tailless flapping wing vehicles present several challenges of stability and control which are not an issue for conventional aircraft. The unsteady aspects of flapping wing flight, coupled with the fact the lifting and propulsive surfaces are the same, complicate FWMAV control. Previous research efforts utilized quasi-steady blade element analysis and computer simulations, rather than experimental tests.

Several conclusions were reached through this research effort. First, it was shown quasi-steady blade element analysis provided an adequate first-order approximation for the forces and moments of the FWMAV, but failed to predict certain aspects of the flapping wing kinematics such as coupling between degrees of freedom and the generation of spanwise side forces. Second, limited tethered motion experiments demonstrated the BABM technique could alter the yaw and pitch moments of the FWMAV in order control the attitude of the FWMAV. Overall, Anderson proved BABM can be used to control forces and moments in five degrees of motion. His research showed BABM is a promising control technique for insect-sized MAVs, and is thus ideal for further exploration.

Lindholm's research continued exploring Anderson's BABM control methodology through a continued look at how to employ a control architecture. He measured the power generated by the actuators, studied passive rotation joint optimization, and conducted a series of closed loop tests to study the BABM control method [16]. The constrained close loop experiments were successful for three BABM parameters. These were symmetric split-cycle parameter modulation, symmetric bias modulation, and symmetric amplitude modulation. Lindholm's research contributed greatly to advancing the BABM control scheme. He reiterated the need to further work on

hardware and software related to the control of the flapper, as well as a need to optimize the existing parts of the flapper mechanism, such as strengthening the joint or reducing the weight of the actuators.

O'Hara conducted a morphological study of *Manduca Sexta* forewing specimens for the purpose of constructing a biomimetic wing with comparable material and structural properties and similar flapping performance [18]. The study began with measurements of the mass and shape of the various parts of several hawkmoth specimens. The individual body parts of the *Manduca Sexta* were removed after which length, chord, area, and mass were determined.

Afterwards, the scales of the hawkmoth were removed and the nature of the venation of the wings was determined. This was done by capturing top-down images of the wing as well as images of cross-sectional cuts of the wing to measure venation thickness, as shown in Figure 9.

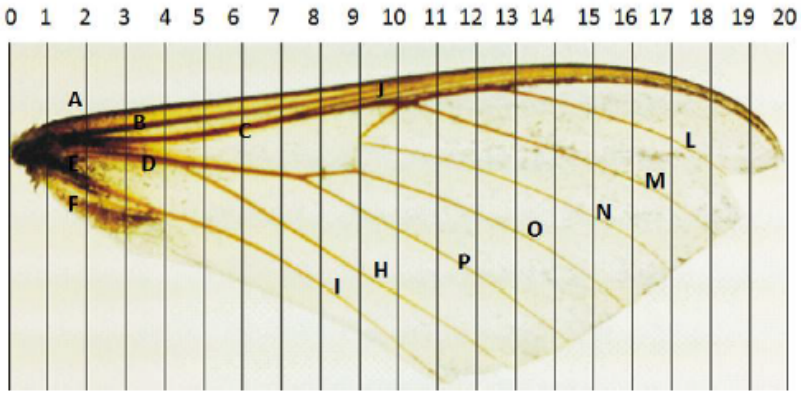

Figure 9. Locations of Cross-Sectional Cuts Made to Measure Venation Dimensions Across the Wing [18]

The material properties of the veins and wing membrane, to include the elastic modulus and hardness, were then measured. The radial vein was held in a cantilever configuration and then underwent excitation with a shaker. A scanning laser vibrom-

eter measured the response of the vein, after which this data was used to calculate the elastic modulus. An indentation machine measured the elastic modulus of the membrane at several locations shown in Figure 10.

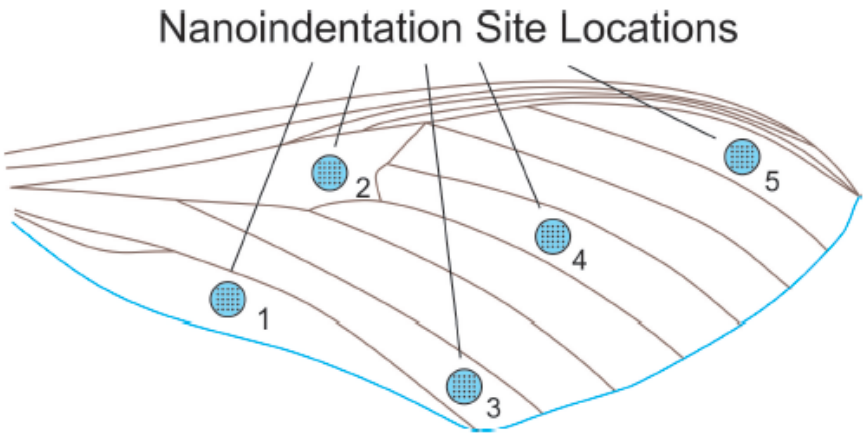

Figure 10. Nanoindentation Locations for Measuring Membrane Properties [18]

Finally, a laser was used to measure the three dimensional structure of the wing, including camber. This completed a thorough morphological study of the material and structural properties of the forewing of the *Manduca Sexta*. Following the morphological study, OHara conducted scanning laser vibrometry tests to determine the dynamics of the forewing, to include a determination of the first bending mode and first torsional mode. After developing a proper understanding of the wing, OHara selected various materials which would best match the properties of the Manduca Sexta forewing. Through consideration of the material properties of the biological wing, conclusions reached by previous research, and measurement of the properties of various materials, it was determined that 12.5 μm Mylar is a suitable material to mimic the membrane, while a 0/90/0 YSH-70A carbon fiber laminate best replicates the strength and stiffness of the venation pattern.

Following this, OHara detailed a step-by-step method for in-house fabrication of the biomimetic wing. The construction of the wing included the pressing of the carbon

fiber laminate, the development of CAD designs of the venation pattern, the use of laser ablation to cut the CAD patterns into the carbon fiber, the pressing together of carbon fiber and Kapton, and thermosetting of the mylar membrane.

The fabrication of the flapper base, shown in Figure 11, was similarly described. This included the construction of a carbon fiber and Kapton stack-up and laser-cutting of the flapper base. The wing was then attached to the flapper base, which in turn attached to a rapid-prototype base, thus completing the flapper.

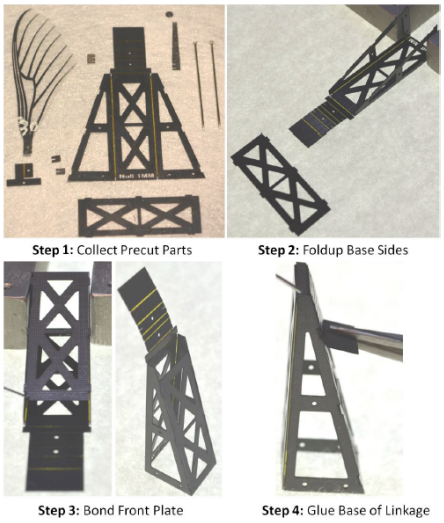

Figure 11. Flapper Base Fabrication Process [18]

Once complete biometric wings were constructed, testing was conducted to compare the engineered wing to the biological wing, shown in Figure 12. This testing determined the aerodynamic performance of the engineered wing matched the biological wing without scales, thereby showing that the final wing and flapper design is suitable for future FWMAV research in the 50 mm length wing configuration.

DeLuca used the O'Hara wing design to conduct a series of tests to provide a comprehensive understanding of the forces and moments as well as aerodynamic effects produced by the new wing design [5]. An ATI Nano-17 Titanium Force Torque

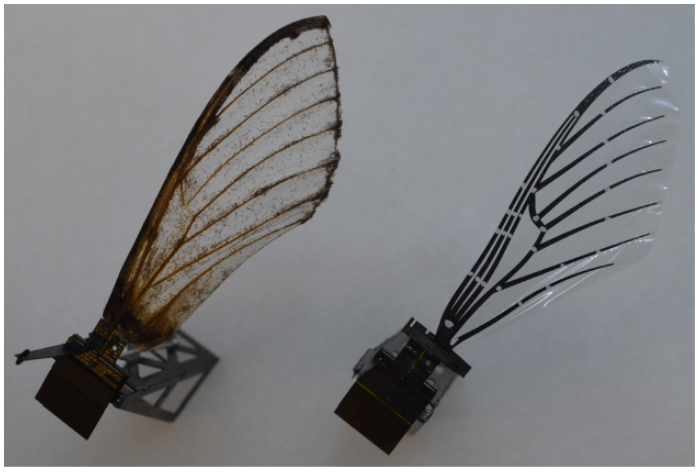

Figure 12. Biological *Manduca Sexta* Wing vs Biomimetic *Manduca Sexta* Wing

sensor was used to measure the forces on the wing, while a stereo PIV system was used to capture images of the airflow. The tests utilized various angle stops, used to alter the angle of attack of the wing by limiting the range of rotation at pronation and supination. Figure 13 shows the 30, 45, and 60 degree angle stops used.

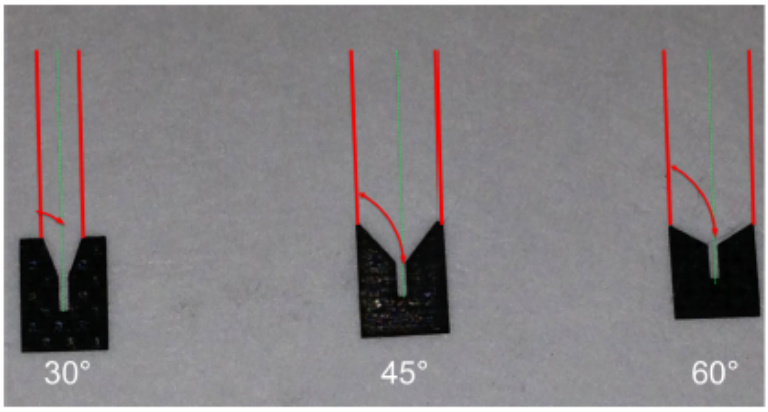

Figure 13. 30, 45, and 60 Degree Angle Stops Used to Modify the Angle of Attack [5]

The tests led to several insights into the biomimetic *Manduca Sexta* wing. First, it disproved Anderson's assumption that the 45 degree angle stop would provide optimal performance for flapping wings of this size. Instead, testing showed the 60 degree

angle stop required lower driving amplitudes to obtain the maximum linkage stroke angle, while having a similar force to power ratio to the 45 degree wing. Second, it was determined small, but non-negligible side forces were generated by the wing due to span-wise airflow, which contradicts the BEM assumption of no side forces. Third, the PIV imagery, shown in Figure 14, and force/moment measurements together conclusively determined the nature of the unsteady aerodynamic airflow, how exactly the vortices form and shed, and why exactly the quasi-steady assumption failed to provide accurate predictions for the forces and moments of the wing.

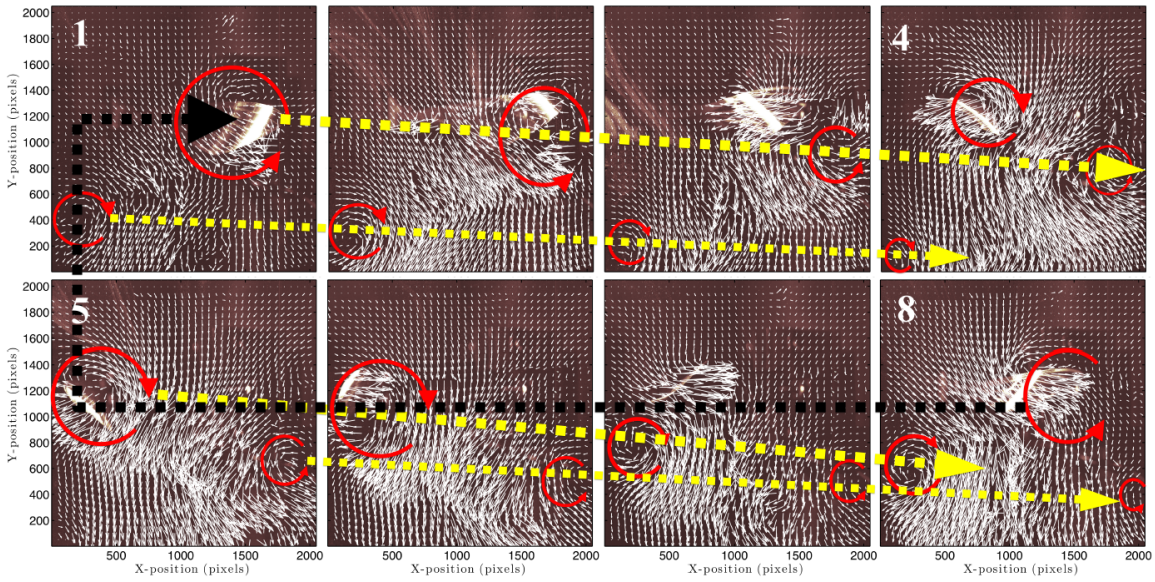

Figure 14. PIV Images of LEV Formation and Shedding [5]

Finally, empirical dimensionless coefficients were calculated which are available for use for future control models. The kinematic angles were calculated using high speed camera imagery and an edge detection algorithm, through which instantaneous lift and drag coefficients were calculated with BEM theory. These coefficients were also utilized to estimate lift and drag using lifting line theory. Figure 15 shows a summary of the BEM values gathered using the aforementioned data.

Table 4.2: Summary of Blade Element Model Mean Aerodynamic Coefficients

Parameter	30° wing	45° wing	60° wing
$\bar{\alpha}$	59.6°	49.7°	40.1°
$\bar{\Phi}$	88°	99°	107°
$\overline{C_L}$	0.5	0.8	1.0
$\overline{C_D}$	08	1.1	1.3
$\overline{L/D}$	0.4	0.5	0.6

Figure 15. BEM Mean Aerodynamic Coefficients For Various Angle Stops [5]

Lt. Cmmndr Brown [2] addressed an issue delineated by previous AFIT researchers; namely, the need to increase the lift to weight ratio of the wing. Attempts at achieving this by designing lighter actuators have been made with mixed results [15]. Brown's research investigated reducing the weight of the wing using finite element analysis. In his research, Brown analyzed the areas of lowest stress in the wing, and created several alternative designs in an attempt to reduce the weight of the wing without degrading its strength and stiffness to an appreciable degree.

Several of the alternative designs had superior vertical force to weight, and vertical force to power ratios, compared to the originally biomimetic wing design. However, none of the wings, to include the original wing design, were able to match the vertical force production measured independently by O'Hara and DeLuca [18, 5]. The small weight reduction achieved through venation removal suggests a renewed attempt at reducing the weight of the piezo would remain the most promising route in maximizing the vertical force to weight ratio of a FWMAV.

2.6 Chapter Summary

The preceding chapter outlined the basics of insect-sized flapping wing research, and more specifically overviewed the research done at AFIT regarding the *Manduca Sexta* inspired biomimetic FWMAV. A thorough overview of the aerodynamics of flapping wing flight was given, to include a review of the flapping dynamics and kinematics and the unsteady vortices which contribute to producing lift. The stability and control problem applied to FWMAVs was also reviewed. The complexity of stability and control for such insects was highlighted, and a review of the quasi-steady BEM assumptions and the BABM control scheme was conducted. A review of the mechanical issues surrounding biomimetic wings was made, which highlighted the promising nature of piezoelectric actuators. The use of a 4-bar linkage to translate the actuator's motion into angular flapping motion was also described, as well as the use of a passive rotation joint to enable pronation and supination of a flapping wing. Finally, the research done by AFIT students was described at length. This included the contributions in control made by Anderson and Lindholm, the contributions in fabrication and assembly made by O'Hara, the advancements in aerodynamics made by DeLuca, and the improvement in lift to weight ratio made by Brown. The following chapter will examine the methodology used in the present research, to include the fabrication of elongated wings, laboratory set-up and instrumentation, flapper operationalization, and vacuum testing procedures.

III. Experimental Methodology

3.1 Construction of Constant Aspect Ratio, Longer Span Wings

The flapper assemblies used in this research were all fabricated as prescribed by O'Hara and Lindholm [18, 16]. The materials used in the fabrication process were carbon fiber, Pyralux, 12.5 μm, 25 μm, and 50 μm Kapton, Mylar, porous and nonporous Teflon, and Airweave SS FR bleeder cloth. The hardware used in the fabrication process include an LPKF Multipress S, LPKF Proto Laser U, and Eden 500V rapid prototype machine. Additional CAD drawings were made in order to fabricate larger wings for the purposes of this researcher.

The geometries used to cut the carbon fiber and Kapton pieces were designed in CorelDraw by previous students. Four larger wings geometries were created, all based on the CAD files of the original wing. The new wings, shown in Figure 16, were 55, 60, 65, and 70 mm in length.

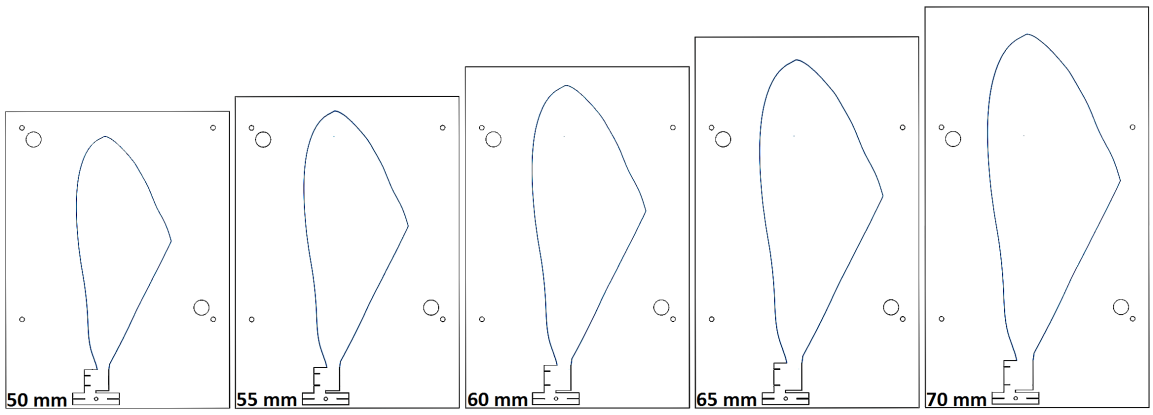

Figure 16. CAD Geometry of 50, 55, 60, 65, and 70 mm Wings

The width of the passive rotation joint, defined in Equation 7, was modified to increase the joint's stiffness in proportion to the increase in the length of the wing. Hence a 40% longer wing, measured from where the rotation joint meets the wing

base, also had a 40% wider rotation joint. All five passive rotation joint designs are show in Figure 17.

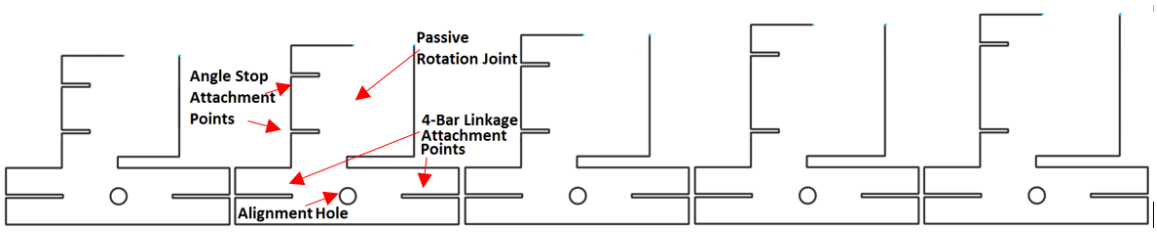

Figure 17. CAD Passive Rotation Joints of 50, 55, 60, 65, and 70 mm Wings

The slits through which the angle stops are placed were moved further apart as the passive rotation joint widens. The attachment point to the 4-bar linkage remained unchanged in dimensions. The wing planform area was scaled in equal proportions in both directions, to ensure the aspect ratio remained constant. The rectangular boundary of the CAD drawings was lengthened to accommodate the increased length of the wing. However, the boundary was not widened, to ensure the two alignment holes remained identical for all CAD drawings. Because each wing was made with four separate CAD drawings, as shown in Figure 18, it was critical all four drawings were altered in complete synchrony with one another.

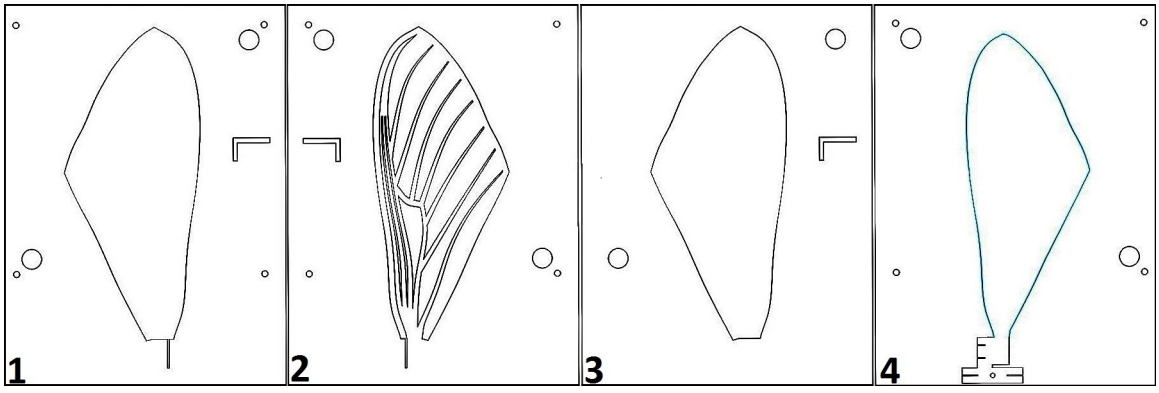

Figure 18. Wing Geometries For Separate Fabrication Steps. 1 and 2 are for Carbon Fiber, 3 is for Kapton, and 4 is for Combined Carbon Fiber, Kapton, and Carbon Fiber

The four separate CAD drawings were used for laser ablation of carbon fiber, Kapton, and combined Carbon Fiber, Kapton, and Carbon Fiber (CKC). The separate CAD drawings for each wing length were visually overlaid in Microsoft Paint, as shown in Figure 19, to ensure perfect overlap for all four rectangles, wings, alignment holes, and fiducal holes. This step often revealed discrepancies between the separate CAD images caused by errors in the lengthening process.

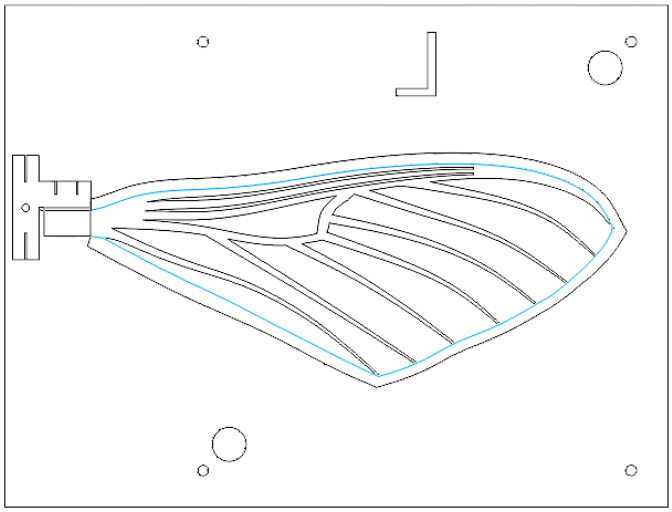

Figure 19. Four Separate CAD Images Overlaid to Ensure Synchronous Alteration

The elongation of the passive rotation joint also brought to focus the definition of wing length (R). The wingtip velocity was calculated by measuring the distance between the wingtip and the point about which the wing rotated. The wing did not rotate about the wing root, which was used to measure R. Rather, the wing rotated at the 4-bar linkage. Therefore, a more accurate distance for measuring the wingtip velocity was from the tip of the wing to the edge of the attachment point to the 4-bar linkage. This new wing length was named R_2, shown in Figure 20.

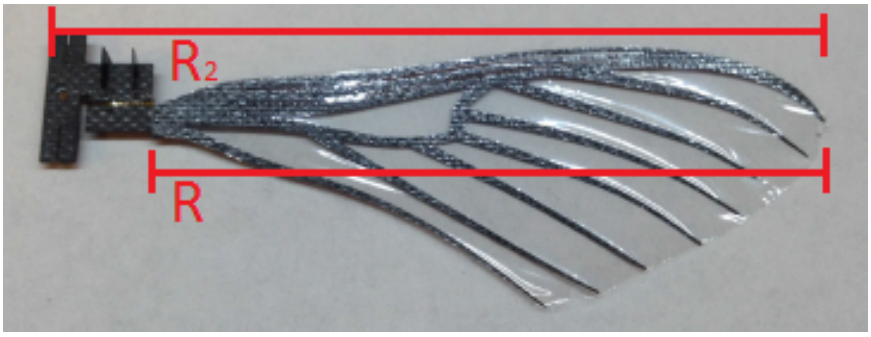

Figure 20. Comparison Between R, Used to Calculate L, and R_2, Used To Calculate V

Table 1 compares the two lengths for the five wings. The discrepancy varied from 7.5 mm for the smallest wing to 9.3 mm for the largest wing, with the increase in the defined length varying from 15% for the smallest wing to 13.3% for the largest wing. R was used to calculate the characteristic length L, which was the mean chord of the wing, while R_2 was used to calculate the wingtip velocity. Equation 4 was reformulated to account for the two seperate lengths.

Table 1. R vs. R_2 Length

R (mm)	50	55	60	65	70
R_2 (mm)	57.5	63	68.4	73.9	79.3

$$Re = \frac{4\rho\Phi f R R_2}{\mu \mathcal{AR}} \tag{8}$$

Φ = stroke angle

f = flapping frequency

$\mathcal{AR}$ = aspect ratio

ρ = air density

R = wing length

R_2 = length from wingtip to 4-bar linkage attachment point

μ = dynamic viscosity

Figure 21 shows the final assembled flapper assemblies. The wings are enlarged but attached to carbon fiber bases and rapid prototype bases of the same size.

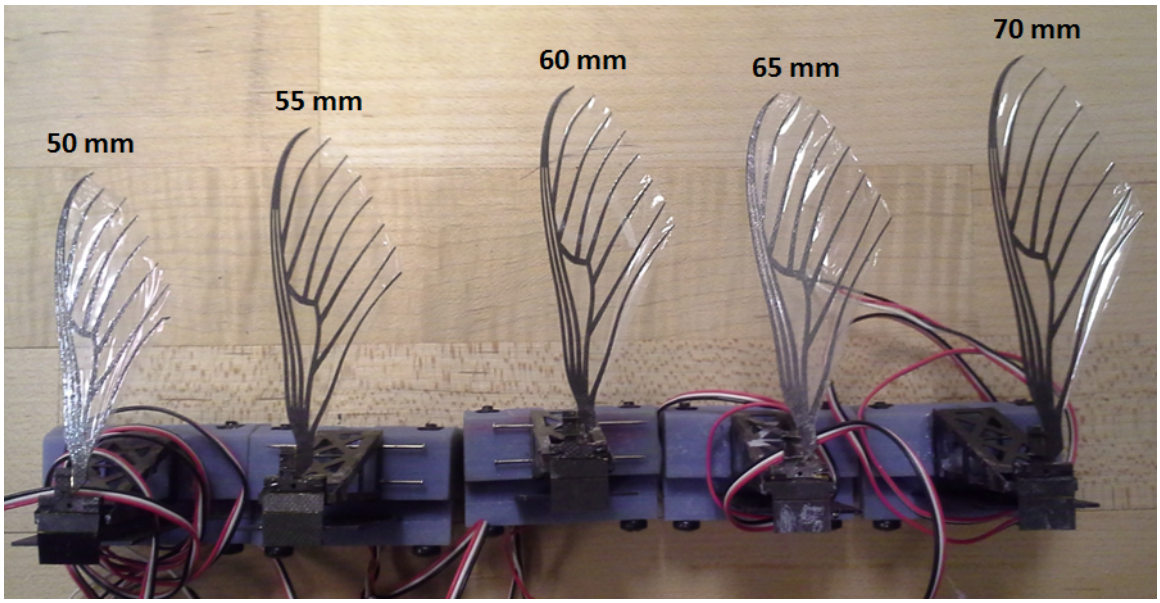

Figure 21. The 50, 55, 60, 65, and 70 mm Wings

3.2 Lab Setup and Instrumentation

Six hardware components were used to collect the force, moment, velocity, position, and optical data; three high-speed cameras, the Nano-17 force transducer, the Micro-Epsilon optoNCDT 1800 displacement sensor, and the Polytec OFV-5 vibrometer.

There were three high-speed cameras. A X-Stream XS4 camera was mounted above the flapper and provided a top-down view, a NanoSense MKII camera was mounted across from the flapper, and another X-Stream XS4 camera was mounted on a tripod. The three cameras, seen in Figure 25, were mounted in line with the

Cartesian coordinate system of the flapper, shown in Figure 22. The cameras had a frame rate of up to 5000 fps. The exposure, γ, and sensor gain was varied for each individual camera so all three cameras capture images of roughly equal brightness. The top camera was exposed to more light than the other two cameras, and thus required a lower sensor gain and exposure. The top mounted camera was wired as the "master" camera, while the other two cameras were designated "slave" cameras. This enabled all three cameras to record simultaneously if the "master" camera was triggered.

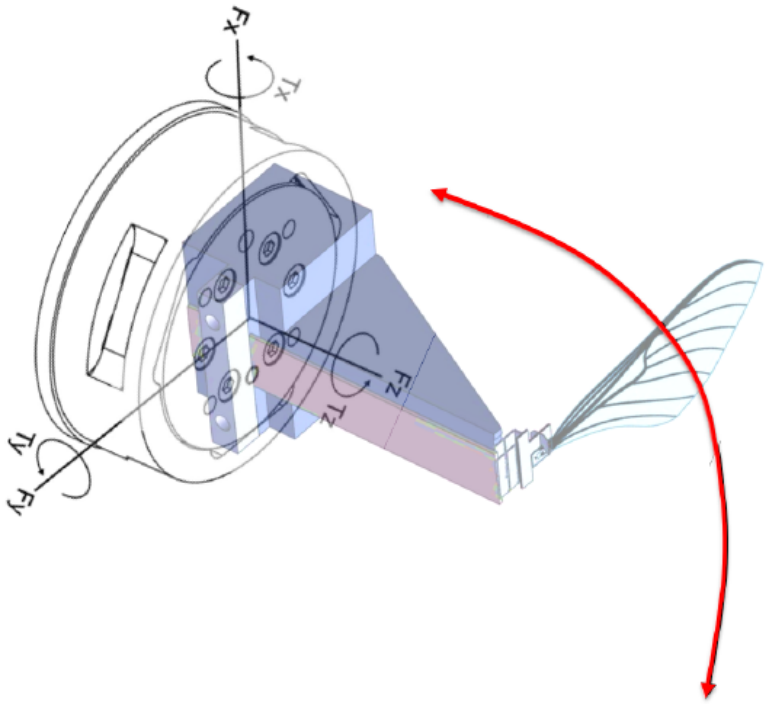

Figure 22. Nano-17 Coordinate System [5]

The cameras were used for two primary purposes. First, the high-speed footage was used in the flapper operationalization process to ensure the wings were flapping properly, to include symmetrical up and down strokes, and complete pronation and supination. Second, the video footage could be used to measure the kinematic angles of the wing.

The ATI Nano-17 transducer is a six degree of freedom transducer, shown in Figure 22. It measures forces and moments on three axes. The data was used to calculate the cycle averaged forces and moments over a single flap cycle. This included the cycle-averaged vertical (F_x), axial (F_z), and side (F_y) forces as well as the cycle-averaged pitch (M_y), roll (M_z), and yaw moments (M_x).

The Micro-Epsilon optoNCDT 1800 distance sensor, shown in Figure 23, was used to measure the displacement of the tip of the piezo. The sensor was mounted behind the wing on a rapid prototype base so the laser pointed at the leading edge of the piezo. The optical sensor detected the reflect laser energy and determined the distance from the emitter to the optoNCDT 1800. This distance was compared to a tared distance to determine the displacement of the piezo from the neutral position at a specific instant. This data was used to approximate the wing stroke angle using Equation 5, and was also used to determine the natural frequency of the wing in the flapper operationalization process. The sensor was calibrated to determine the relationship between the output voltage of the sensor and the displacement of the piezo from the neutral position.

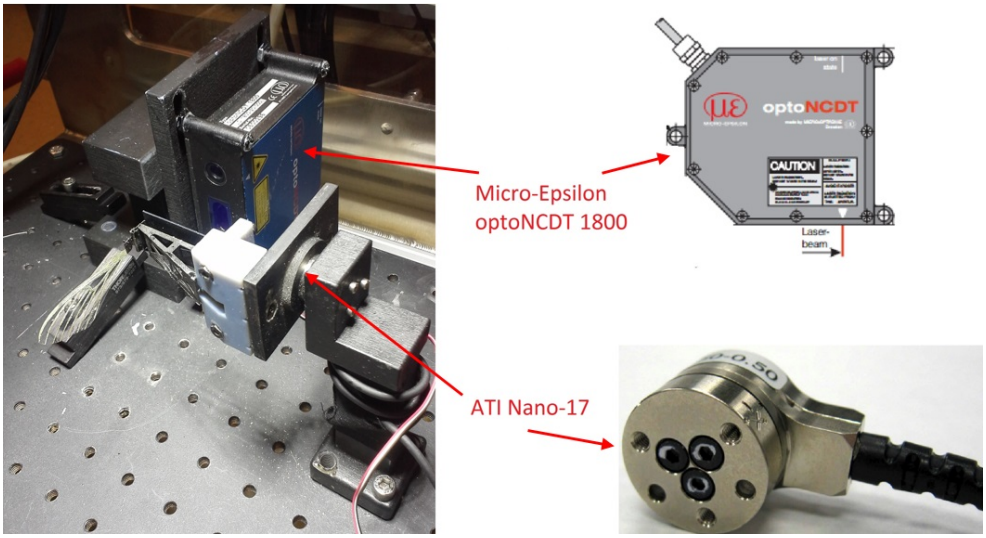

Figure 23. Nano-17 and optoNCDT Placement

During calibration, the sensor was attached to a specially designed rig at a specific distance from a thick sheet of black metal, show in Figure 24 below. The sensor output was measured with a voltage meter, with the voltage tared at one sheet of metal. Successive sheets of metal were placed in front of the first sheet of metal. The thickness was measured and recorded at each step with a digital caliper, while the voltage was similarly measured and recorded.

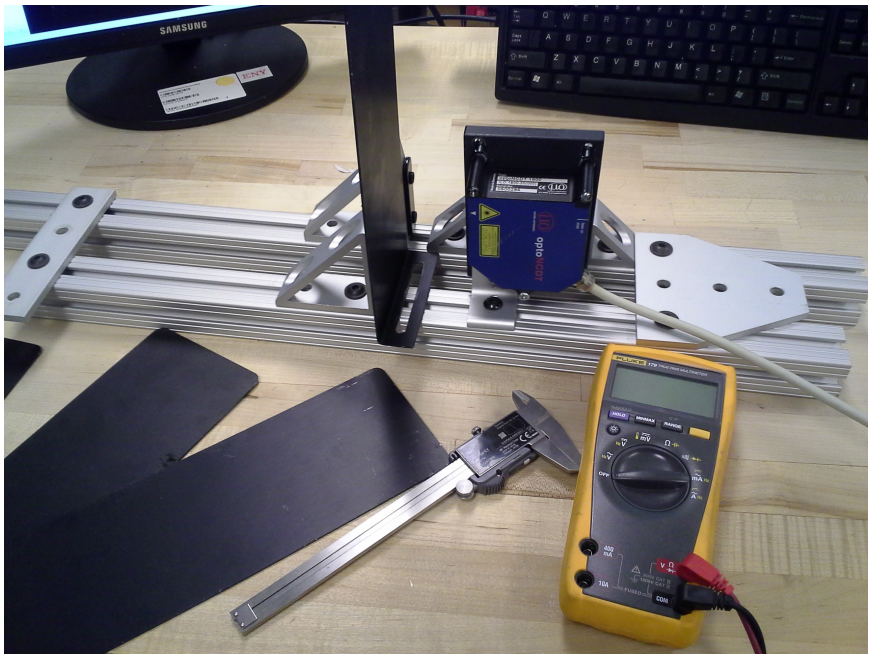

Figure 24. Displacement Sensor Calibration Rig

Four sheets of metal were used in this process. The data was plotted, and a linear curve fit was plotted through the measured data. This procedure was repeated two more times, which led to three separate scatter plots, with three separate linear curve fits. The slopes of the three curve fits were averaged, which gave a final slope of 13.03 volts per inch. The calibration ensured the voltage output by the optoNCDT during flap testing was accurately converted into displacement data.

A Polytec OFV-5 vibrometer measured the tip velocity of the piezo. This data was used to calculate the natural frequency of the wing in the operationalization process.

The voltage to distance ratio was be set to 10 mm/s per volt, as this conversion ratio was best suited for the velocities measured at the tip of the piezo. The Polytec OFV-505 vibrometer sensor head was placed as shown in Figure 25 so the laser was focused to a narrow dot on the leading edge of the piezo, opposite from where the distance sensor was focused on. An inclinometer measured the slope of the vibrometer head, which in this research effort was 3 degrees. This angle was accounted for when making velocity measurements with the vibrometer data.

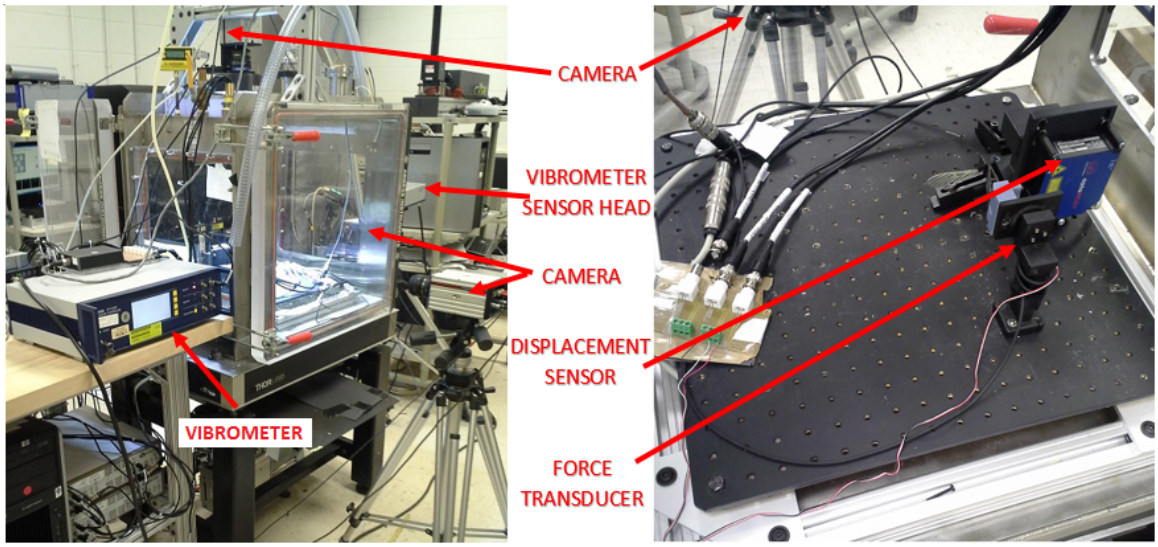

Figure 25. Lab Instrumentation Setup

The piezo is attached via three wires to cables which receive a signal from a Trek PZD700A amplifier. These are an AC signal and a DC signal. The amplifier receives the DC bias and AC signal from the computer via the National Instruments USB-6229 Data Acquisition Device, or NI Box, amplifies the signal by 30x, and then sends the signal to the flapper to induce flapping. The following equations describe the construction of the flap signal sent to the piezo.

$$Sinusoidal\ Drive\ Signal = (DC Bias\ Signal)(\frac{1}{2} + Sin(wt) + \eta) \tag{9}$$

$$DC Bias\ Signal = A(200V) \tag{10}$$

w = Frequency

η = Bias

The peak voltage, peak current, and phase shift (θ) data are used to calculate the power consumption using the equation below, where the phase shift, ϕ, is the angle between the two signals.

$$P = \frac{I_{peak} V_{peak} cos\theta}{2} \tag{11}$$

P = power

I_{peak} = peak current

V_{peak} = peak voltage

θ = phase shift

The NI Box, shown in Figure 26, facilitates the transmission of data and electrical signals. It sends and receives signals from the amplifier, and receives data from all of the instruments except for the cameras. It also connects to the computer via USB and thereby sends and receives data to and from MATLAB. The high-speed cameras are linked directly to the computer via USB.

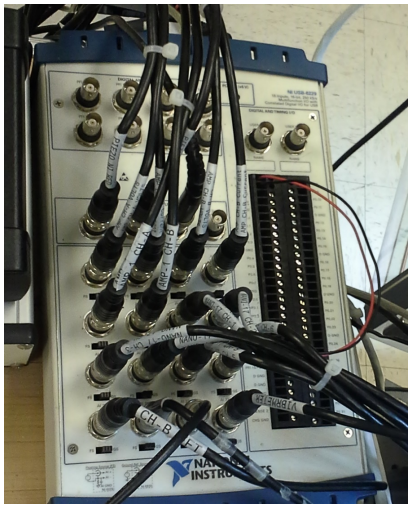

Figure 26. NI Box

3.3 Flapper Operationalization

The flapper operationalization consists of a three step process: finding the natural frequency, autotuning, and manual tuning. At the first natural frequency of the flapper system, the stroke angle is maximized, while the power required to drive the PZT is minimized, which maximizes vertical forces at a minimum power input. The natural fequency varies depending on the stiffness and the mass of the wing, shown in the following equation.

$$w_n \propto \sqrt{\frac{k_{eq}}{m_{eq}}} \tag{12}$$

$$w_n = \text{natural frequency}$$

$$k_{eq} = \text{equivalent stiffness}$$

$$m_{eq} = \text{equivalent mass}$$

From the flapper GUI main menu, written by DeLuca for operating the flapper, the *Chirp* function is selected [5]. The user inputs a driving amplitude, beginning and ending frequency, sampling rate, and sampling time, shown in Figure 27.

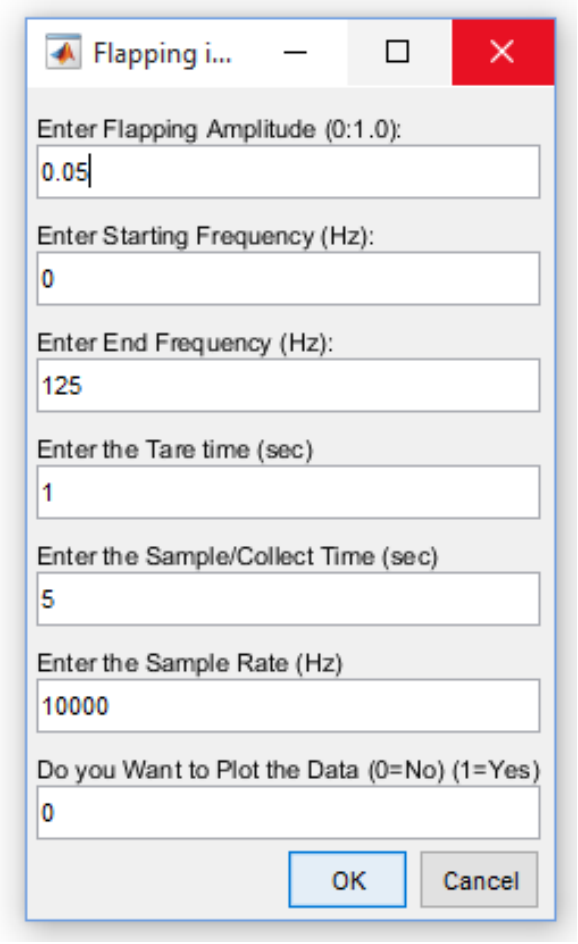

Figure 27. GUI Input for *Chirp*

In this research the driving amplitude is set at A=0.05, or 10 volts, the starting frequency is set to 0 Hz, the ending frequency is set to 125 Hz, the sampling rate is set at 10000 Hz, and the sampling time is set to 5 seconds. Once the chirp parameters are entered, the flapper will sweep through the frequency spectrum. The force transducer, displacement sensor, and vibrometer collect the response data during the sweep. This data is used to calculate the Frequency Response Function (FRF), which is used to compute the first bending mode and first torsional mode of the flapper and wing system. The force transducer data shows low coherence, suggesting the Nano-17 is unable to differentiate between actual forces, and signal noise at low driv-

ing amplitudes. The vibrometer and distance sensor consistently measured modal peaks at identical frequencies, suggesting both instruments were able to measure the natural frequency of the wing and flapper system. The frequency sweep was repeated five times for each new wing, and the data was averaged to obtain the first natural frequency of the wing.

Figure 28. GUI Input for *Autotune*

Once complete, a tuning process was conducted for each wing. The tuning of the wing was done to ensure symmetric flapping, meaning both the downstroke and upstroke were of equal angles. The inherent piezo bias made perfectly symmetric flapping difficult. Therefore the autotune MATLAB script was run. The GUI asked for a driving amplitude sweep, maximum acceptable piezo displacment, and an error tolerance between upstroke and downstroke piezo displacment, as shown in Figure 28.

The piezo was run at the lowest amplitude. The displacment sensor data was then used to measure the displacement symmetry, and the piezo was run with an automatically calculated bias (η) to negate the asymmetry. This process was continuously repeated until the script found an η value which lent itself to displacement symmetry between the up-stroke and down-stroke within the error tolerance. The autotuning program would then step up to the next driving amplitude increment, and repeat the previous process again, until the η values were established for all driving amplitudes for that wing.

Once the autotune process was complete, the wing was manually refined. Although the autotuning program ensured symmetric piezo bending, the inherent variability in the fabrication process led to asymmetric flapping at higher amplitudes, even after autotuning was complete. Therefore, the η value was manually refined in an iterative process. The high speed camera footage was used to find the pixel location of the focal point around which the wing flapped. The pixel locations of the wing's leading edge at maximum up-stroke and down-stroke were identified, ensuring that the x-axis values of these points were of equal distance from the root of the wing. After these three pixel locations were determined, basic trigonometry was used to compute the up-stroke and down-stroke angles respectively. The η value was adjusted to alter the flapping symmetry, with a positive value biasing the flapper towards the down-stroke,

and a negative η value biasing the flapper towards the up-stroke. The process was continued until flapping was exactly symmetrical, measured by the high-speed footage at a specific driving amplitude.

During the manual tuning process it was also important to look for any other possible issues with the flapper mechanism. The biggest issue monitored was whether the rotations during pronation and supination were occurring properly. Imperfections in manufacturing result in either a frozen rotation joint, or in unequal angles of attack, in which the wing rotated to a greater degree in one direction compared to the other. Since the pronation and supination process was critical for the formation of unsteady flow phenomena used to create lift, it was important to ensure the wing flapped properly in both directions. Reviewing the high-speed footage along with the measured force data helped to determine whether the particular wing was suitable for operational testing.

3.4 Vacuum Testing

The Nano-17 transducer, optoNCDT displacement sensor, and flapper assembly were placed in a 24x24 inch Abbess Instruments and Systems, Inc stainless steel vacuum chamber, shown in Figure 29 below. The vacuum chamber had glass doors on two sides, as well as glass windows on three sides. Tests done at atmospheric pressure were completed with the two doors open to enable easy access to the flapper assembly. For the vacuum tests, the two doors were clamped shut, and the pressure was monitored.

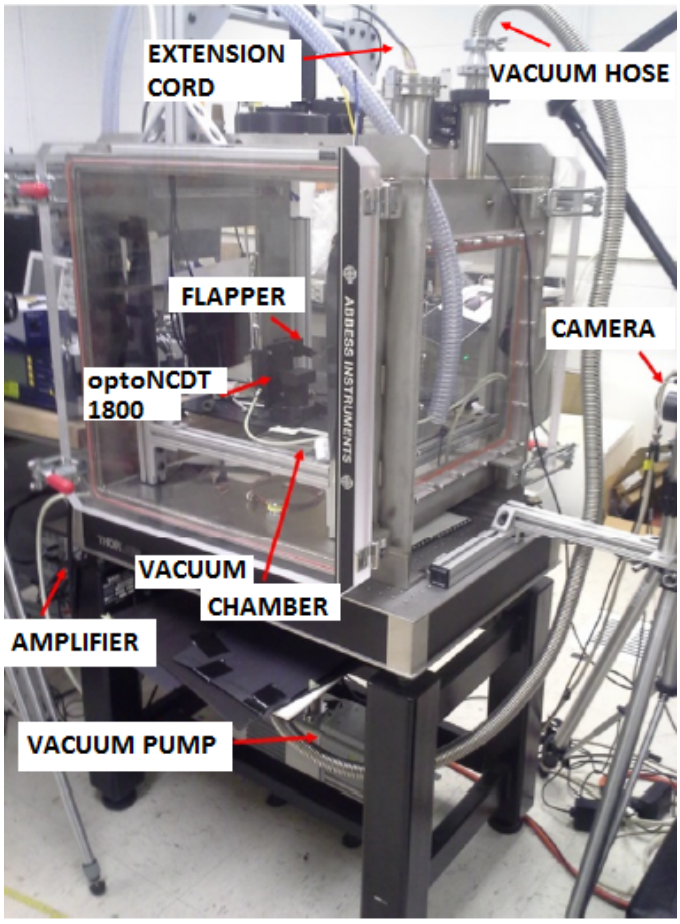

Figure 29. Vacuum Chamber

An Instrutech, Inc Superbee CVM201GAA gauge, shown in Figure 30, was used to measure the pressure of the air. The flapper, Nano-17, and optoNCDT data were relayed through five separate cables, which ran through the vacuum chamber. The optoNCDT and flapper were attached through these extension cables for both atmospheric and non-atmospheric tests to preserve consistency in the signal to noise ratios. The optoNCDT calibration was also accomplished while connected to its respective extension cable. The Nano-17, however, was connected via the extension cable only during vacuum tests. This was done because the Nano-17 gave less precise data when connected to its extension cable because of excessive signal loss. Therefore,

the wing length tests were accomplished without the cable, while the vacuum tests were done with the Nano-17 connected with the extension cable out of necessity. Comparison tests between the forces measured with and without the extension cable were completed to catalog the discrepancy caused by the extension cable.

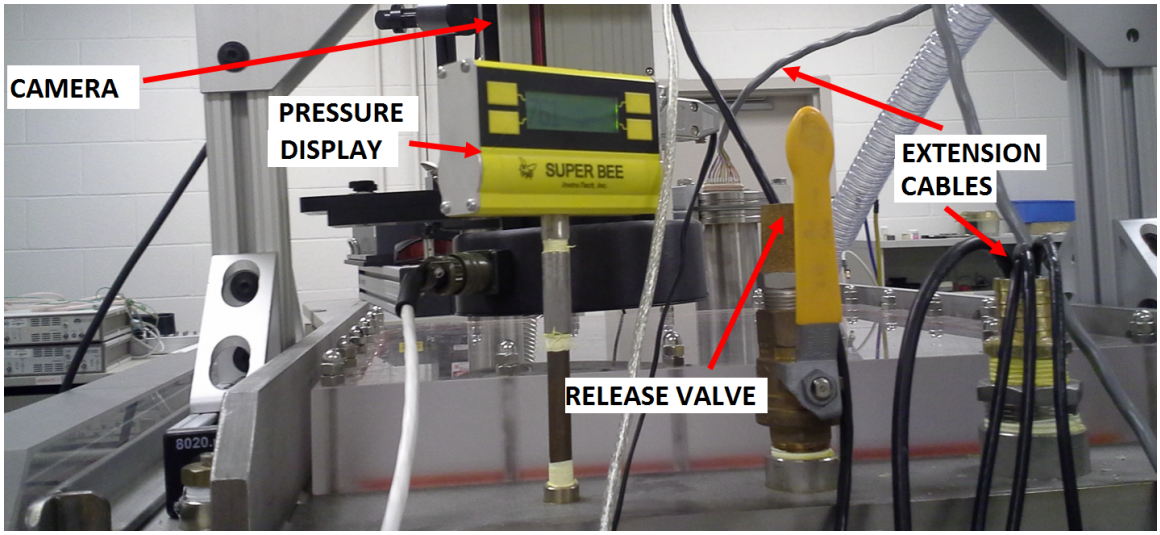

Figure 30. Pressure Display, Release Valve, and Extension Cords

For the vacuum tests, the wing was flapped at atmospheric pressure first at a small number of driving amplitudes to measure baseline data for the wing at normal conditions, as well as to detect if there were any defects in the wing and flapper assembly. After this was accomplished, the vacuum pump, shown in Figure 31, was opened until the chamber was at a pressure slightly lower than the specific test pressure. This was done because the chamber was not 100% sealed, and slowly leaked air. This made it necessary to begin at a lower pressure, and then open the valve to admit air as necessary to reach the desired pressure. Although air did leak from the vacuum chamber, this occurred at a low enough rate so data could be taken at desired pressures within 1% of the prescribed value for a test run of five successive flap cycles.

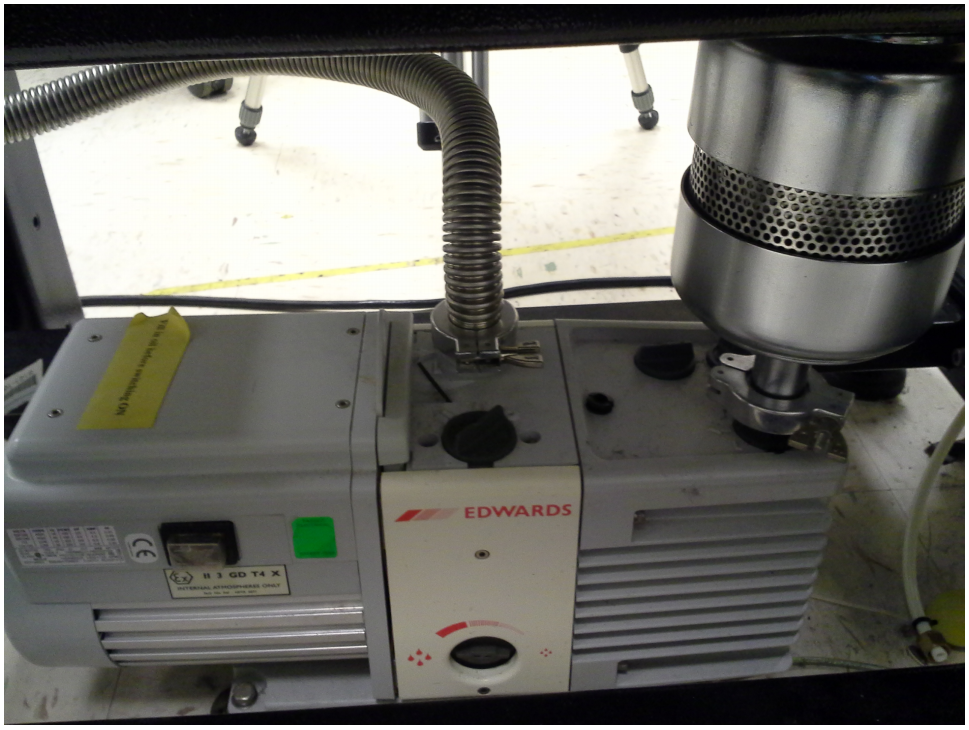

Figure 31. Vacuum Pump

Another consideration for testing at lower densities was the need to adjust the driving amplitude range. For atmospheric tests with the original wing, the driving amplitude voltage was varied between 0.2 A to 0.7 A, in increments of 0.025 A, for a total of 21 different driving amplitudes. However, when the air was at a lower density, less voltage was required to flap the wing at a particular stroke angle, as less drag was encountered by the wing. Therefore, the wing was flapped at various driving amplitudes to determine the value which would achieve the maximum designed stroke angle. The driving amplitude increment was then altered so the number of test points remained the same, given the new maximum driving amplitude. In effect, as the density of the air was decreased, the amplitude sweeps occurred over a smaller span of voltages, but with an evenly spaced number of test points. At the lowest densities, the minimum driving voltage was also be varied, as the wing would flap at

lower voltages. Again, the increments between amplitudes was varied to maintain an equal number of test points.

As previously mentioned, air pressure was maintained at specified values by alternatively engaging the vacuum pump, and opening the air release valve, both shown in Figure 30. Typically the pressure was lowered to slightly below the testing condition, and testing began once the pressure reached the desired levels. Once testing was complete, the vacuum pump was turned on for a few seconds to lower the air pressure, so the manual tuning and data collection could begin for the next driving amplitude. For the tests conducted at the lowest air density, the vacuum pump was operating for the entire test duration to ensure data was collected at the minimum possible air density. The pressure of the chamber leveled out to between 4.3 and 4.33 torr for these tests, or 573 to 577 Pa. This was as low as 0.57% of atmospheric pressure.

3.5 Chapter Summary

This chapter detailed the experimental methodology of this research. This included an explanation of the wing enlarging process, the instrumentation and lab setup, the operationalization process for testing the flappers, and specific considerations for the vacuum testing process. The following chapter will detail the results of the tests.

IV. Results and Analysis

4.1 Chapter Introduction

The research conducted aimed to answer three major questions. First, whether increasing the size of the wing is a suitable means for increasing the vertical force. Second, what the power requirements and force and moment response of the wing are under purely inertial motion, with no aerodynamic effects. Third, whether calculating Reynolds number data and comparing this to wing performance yields any useful trends.

The following tests assisted in answering the three questions. First, a series of tests were conducted with increasingly larger wings, to determine the effect increasing wing size has on vertical force, as well as to develop part of the aforementioned Reynolds number data. Second, a series of tests at partial vacuum were conducted to provide further data regarding Reynolds number. Finally, a test at the lowest possible pressure was conducted, to determine the power requirements, forces, and moments produced by the wing under purely inertial conditions.

The wing size tests required a modification of the 4-bar linkage, detailed later in this chapter. The vacuum chamber tests required a calibration procedure to account for the decrease in precision caused by the use of an extension cable for the Nano-17 transducer. Finally, the symmetry of the flapping motion and comparison of optical and kinematic stroke angles is detailed at length to provide a full picture of the test conditions in which the data was taken.

4.2 Driving Amplitude and Stroke Angle

The primary mechanisms of controlling the flapping of any wing consists of controlling the driving amplitude and bias (η) of the signal sent to the piezo. Figure

32 shows the relationship between driving amplitude and stroke angle for the 50 mm wing.

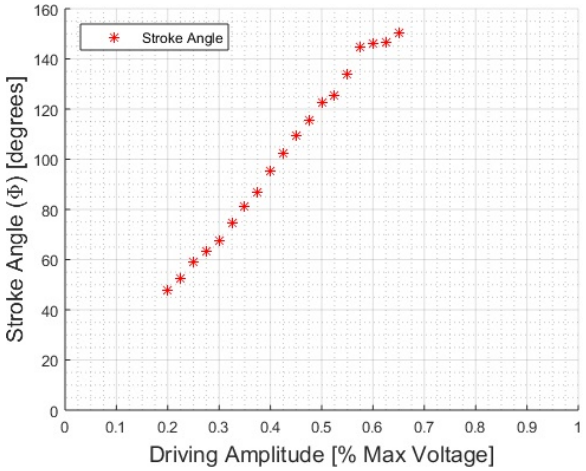

Figure 32. Driving Amplitude vs Stroke Angle of 50 mm Wing Flapping at 17.29 Hz

The driving amplitude is approximately linearly correlated with the stroke angle for most tests, with deviations from this pattern apparent for partial vacuum tests. The use of multiple wings to conduct testing for a single test condition also led to a departure from the perfectly linear ideal relationship. Under certain conditions the wing would shear off at the passive rotation joint, necessitating the use of multiple wings. Nevertheless, an increase in driving amplitude tends to signify an increase in stroke angle. As the driving amplitude determines the voltage, it stands as a reliable indicator of the power required to produce certain forces for a given wing. On the other hand, the stroke angle directly relates to the behavior of the wing itself, regardless of the power sent to the wing, and therefore stands as a better independent variable for comparing wings in different testing conditions. For this reason, the majority of graphs used to describe the behavior of the wings tested reference stroke angle, rather than driving amplitude. Figures 33 and 34 show the forces and moments produced by the wing in relation to both driving amplitude and stroke angle.

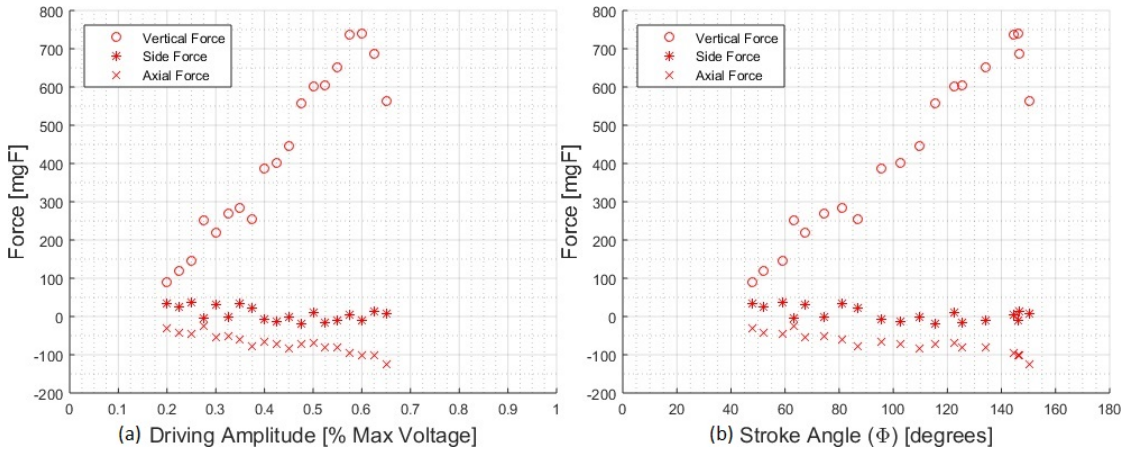

Figure 33. Driving Amplitude and Stroke Angle vs Forces of 50 mm Wing Flapping at 17.29 Hz

The manner in which the forces and moments change in relation to driving amplitude and stroke angle are nearly identical. The closer the relationship between driving amplitude and stroke angle is to a perfectly linear correlation, the more similar two graphs using the two separate variables tend to become. However, as previously mentioned, the relation fails to correlate well for certain test conditions, making stroke angle the appropriate variable to reference.

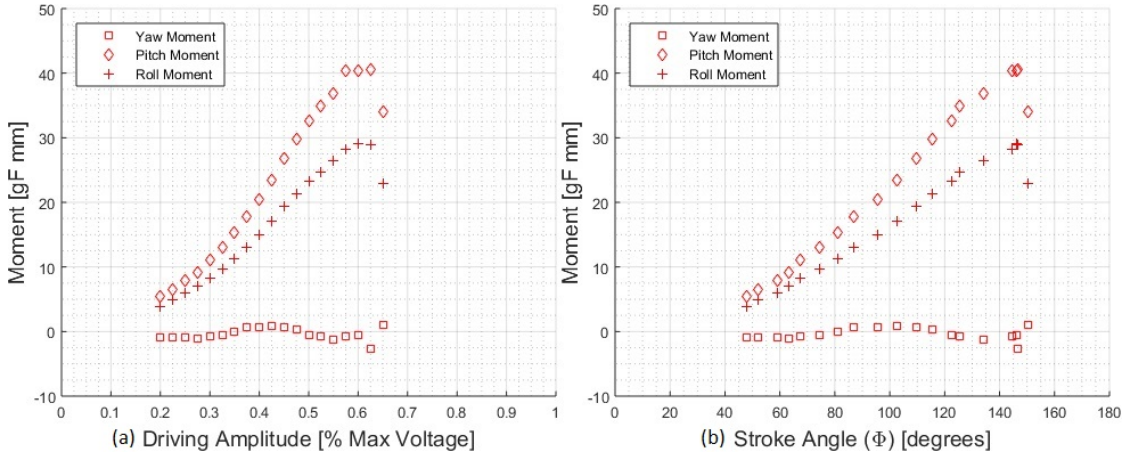

Figure 34. Driving Amplitude and Stroke Angle vs Moments of 50 mm Wing Flapping at 17.29 Hz

Figure 35 shows the power supplied to the wing as driving amplitude and stroke angle are increased. In this case there is a direct relationship between driving amplitude and power, as Equation 11 shows. The relationship between stroke angle and power is not direct, but still follows a roughly similar pattern.

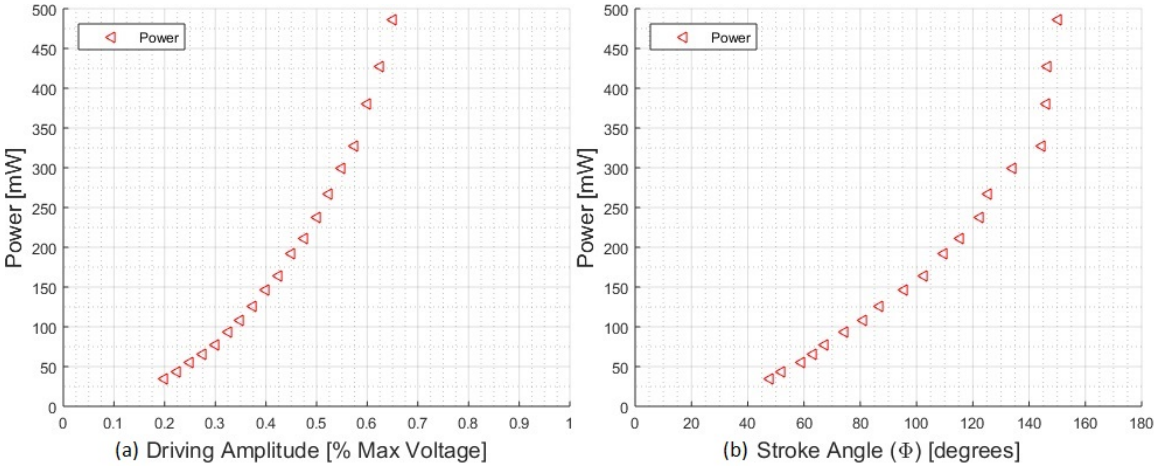

Figure 35. Driving Amplitude and Stroke Angle vs Power of 50 mm Wing Flapping at 17.29 Hz

Although the driving amplitude is directly manipulated through the GUI, the stroke angle is a superior variable for two reasons. First, stroke angle provides information about the relationship between the actual kinematic motion of the wing, and the resulting forces and moments. Second, it enables comparisons between wings with dissimilar driving amplitude vs stroke angle curves.

4.3 Length Modification

Four wings with longer spans were designed to examine the effect of larger scaled wings on vertical force production. Increasing the length of the wingspan leads to an increase in weight. Table 2 shows the weight and natural frequencies of the larger wing designs.

Table 2. Wing Length, Wing Mass, and Natural Frequency of Wings With an Aspect Ratio of 14.42

Wing Length (mm)	Wing Weight (mg F)	Natural Frequency (Hz)	Normalized Wingtip Velocity
50	68.7	17.29	1.0
55	78.1	15.72	1.0
60	94.3	9.43	0.65
65	105.9	8.0	0.59
70	111.5	6.5	0.52

For every 5 mm increase in length, there was a corresponding increase in weight of approximately 10 to 15 milligrams (mg). Testing of the larger wings showed there was a decrease in the natural frequency of the wing with increasing length. The wingtip velocity was calculated using Equation 2 and R_2, and normalized with respect to the 50mm wing wingtip velocity. There is a clear trend of the wingtip velocity decreasing with increasing length, showing the natural frequency decreases at a greater rate than the increase in wing length. Although the increase in surface area theoretically should increase vertical force production; however, the increase in weight of the wing and the decrease in wingtip velocity suggest simply increasing the wing length may not be sufficient alone to increase vehicle lift.

To determine the efficacy of the new designs, a maximum stroke angle assessment was conducted for each wing. The 65 mm and 70 mm wings produced negligible vertical forces even at the maximum stroke angle. This occurred primarily for two reasons: first, the dramatic decrease in tip velocity led directly to a corresponding decrease in force production, and second, the decreased kinetic energy of the wing combined with the stiffer passive rotation joint led to a reduction in the ability for

the largest wings to transition between pronation and supination properly. The 65 mm and 70 mm wings would paddle back and forth, rather than flap properly with the leading edge always in the direction of the oncoming air.

As the two largest wings lacked the capability to produce sufficient vertical forces, no further testing was conducted. Preliminary tests of the 55 mm and 60 mm wings showed sufficient force production to warrant data collection. Figures 36, 37 and 38 show the forces, moments, and power of the 55 and 60 mm wings in comparison to the original wing design.

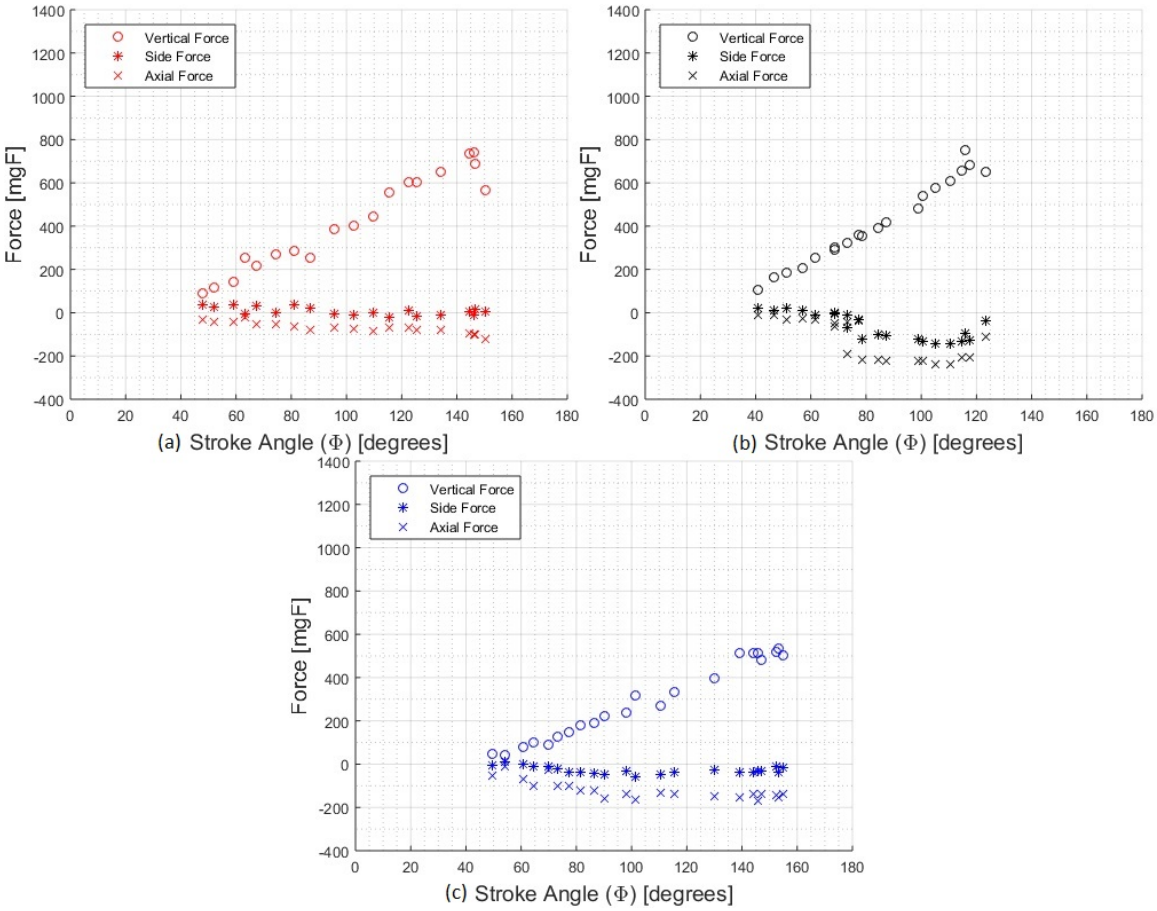

Figure 36. Forces of 50 mm Wing Flapping at 17.29 Hz, 55 mm Wing Flapping at 15.72 Hz, and 60 mm Wing Flapping at 9.44 Hz

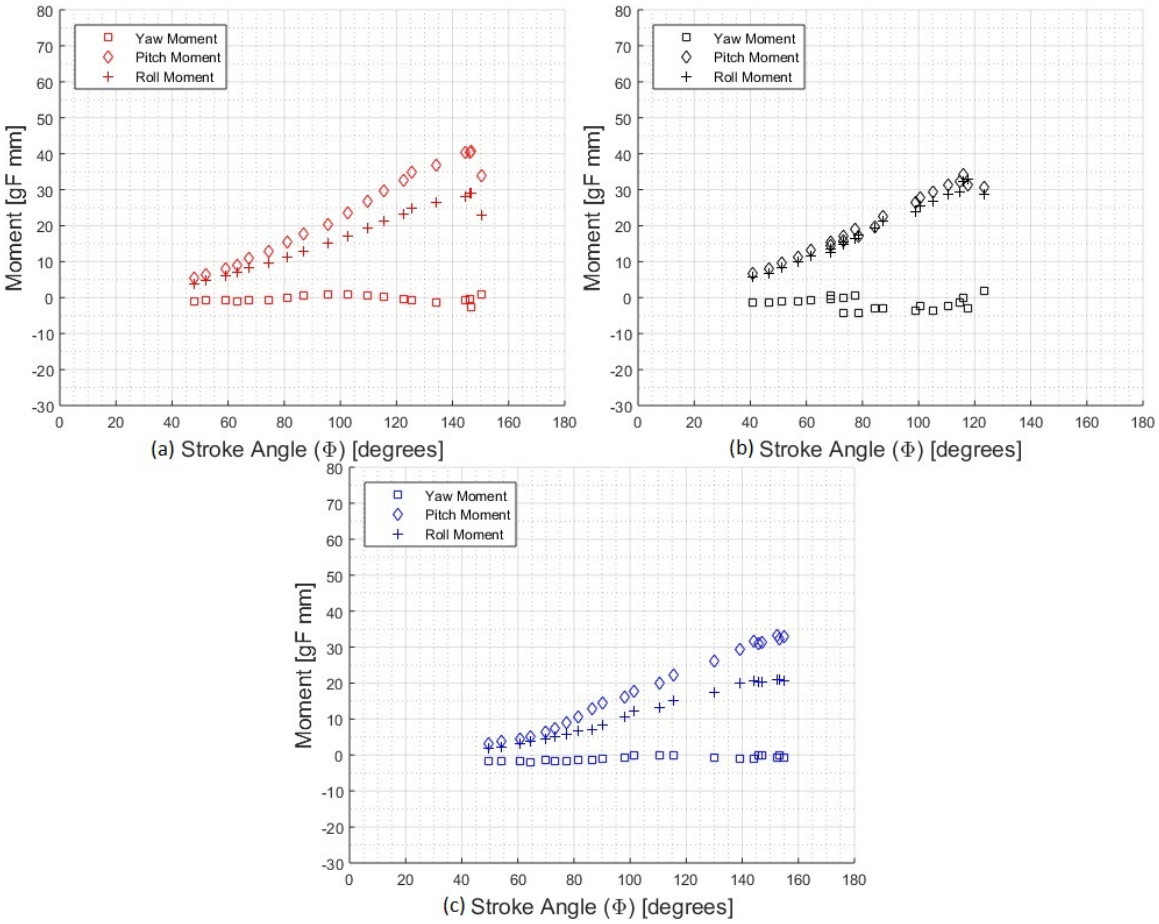

Figure 37. Moments of 50 mm Wing Flapping at 17.29 Hz, 55 mm Wing Flapping at 15.72 Hz, and 60 mm Wing Flapping at 9.44 Hz

The 55 mm wing redesign led to a modest increase in vertical force, ranging from about 50 to 100 mg F for a given stroke angle. This exceeds the 10 mg increase in weight, showing that the 55 mm wing is a superior wing, despite flapping at a lower frequency. The lower flapping frequency combined with the stiffer passive rotation joint provides a design more resistant to failure and wing separation from the joint. As the flappers are placed on the Nano-17 in an offset configuration, any change in vertical force leads to a corresponding change in the pitch and roll moment measured by the transducer, as shown in Figure 37. The 55 mm wing also consumed more power, as shown in Figure 38. The small, but consistent improvement in vertical force

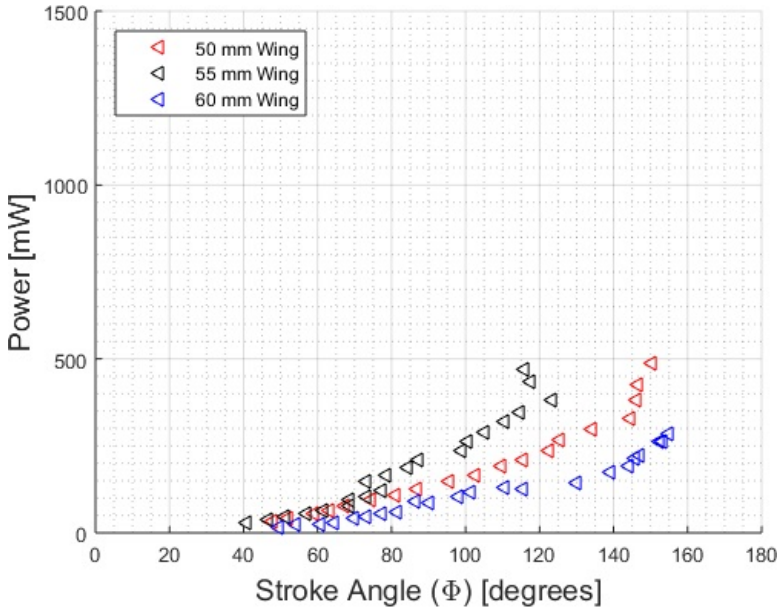

Figure 38. Power of 50 mm Wing Flapping at 17.29 Hz, 55 mm Wing Flapping at 15.72 Hz, and 60 mm Wing Flapping at 9.44 Hz

produced by the 55 mm wings are expected, as measurements of biological *Manduce Sexta* forewings by O'Hara showed a range in length from 42.59 mm to 57.85 mm [18]. One could intuitively surmise the range in wing lengths seen in nature within this single species corresponds with a similar range in total body mass, and hence total lift production. Therefore, the small range of wing sizes seen amongst moths of this species may represent a range in which wing length predominately determines the force production capabilities of the wing.

However, the 60 mm wing shows a clear reversal of this trend. The increased wing length leads to a decrease in vertical force, varying from 50 mg F at a stroke angle of 50 degrees, to 250 mg F for a stroke angle of 145 degrees. This decrease in force production is inexorably linked to the decrease in wingtip velocity due to the drop in natural frequency. As Figure 38 shows, the 60 mm wing consumed less power than the 50 mm wing, which is due to the lower kinetic energy of the flapping wing due to

the lower flapping frequency.

When only length was varied, the improvements in vertical force ceased, and reversed after the length of the wing increased by more than 10% over the baseline 50 mm wing. Reversing the decrease in natural frequency was necessary to produce greater vertical forces. This could be accomplished by increasing the stiffness of the system without an excessive increase in mass. Several possible methods were considered, such as a stiffer carbon fiber matrix, or new cross sectional geometries for the wing's internal venation pattern. However, such methods would have required an inordinate amount of time and effort which were beyond the scope of this research, and thus were not attempted. Several methods were attempted, however, with the already available materials and CAD geometries. This included producing 0/0/90/0 and 0/0/90/0/0 carbon fiber wings, and fabricating a unidirectional carbon fiber reinforcement which was attached to the leading edge of the wing. However, these efforts led to either negligible increases or even decreases in natural frequency, as any increase in stiffness was accompanied by an increase in the mass of the wing. However, efforts to increase natural frequency through altering the 4-bar linkage proved successful.

4.4 4-Bar Linkage Modification

The original 4-bar linkage design consisted of 12.5 μm thick Kapton. To determine whether the 4-bar linkage could be used to increase the natural frequency of the system, two additional 4-bar linkage designs were constructed. The new 4-bar linkages utilized 25 μm and 50 μm thick Kapton joints. The new linkages were fabricated in an identical manner as the original linkage, but with an increased Kapton thickness. Figures 39, 40, and 41 compare the forces, moments, and power of the three linkages, each used to flap the baseline 50 mm wing.

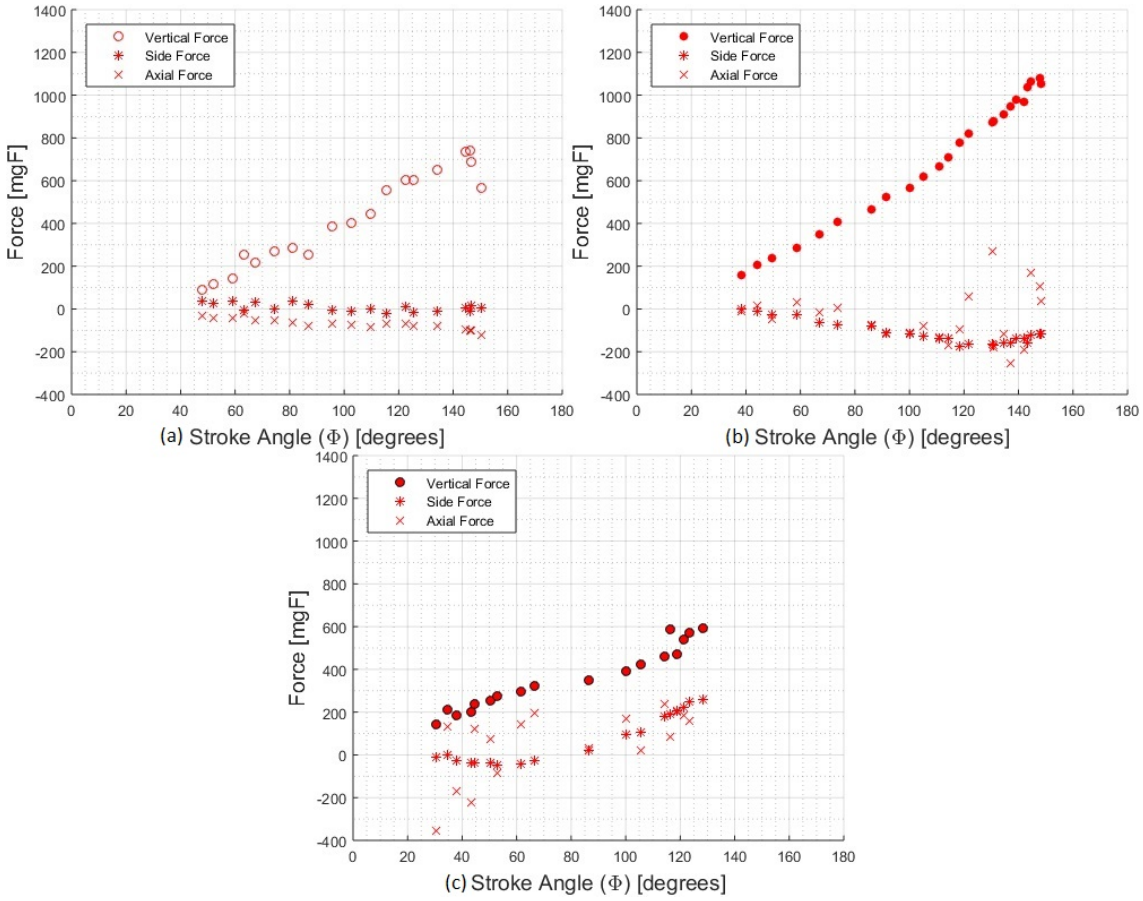

Figure 39. Forces of 50 mm Wing with 4-Bar Linkage Kapton Thicknesses of 12.5 μm Flapping at 17.29 Hz, 25 μm Flapping at 22 Hz, and 50 μm Flapping at 25.9 Hz

There was a clear increase in the natural frequency of the system. While the original wing flapped at approximately 17 to 19 Hz, the 25 μm linkage increased this frequency to 22 Hz, while the 50 μm linkage increased it to 25 Hz. The maximum stroke angle of the wing decreased from 160 to 130 degrees for the 50 μm linakge, possibly due to an increase in drag.

The 25 μm linkage increased the vertical force by 100 to 300 mg F for a given stroke angle, which is in line with theory which posits an increase in wing velocity corresponds to an increase in vertical force. The natural frequency of the 25 μm linkage design corresponded more closely with the natural frequency of the wing

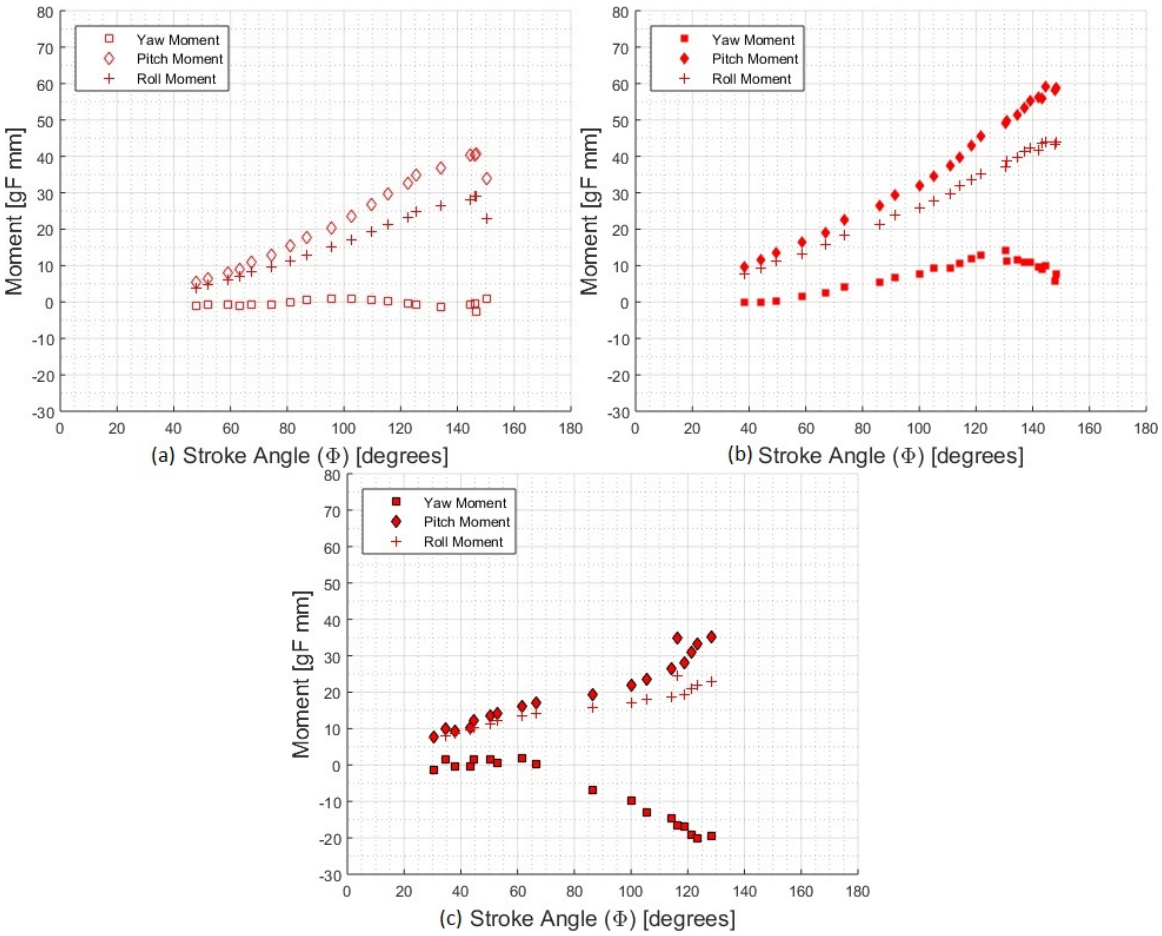

Figure 40. Moments of 50 mm Wing with 4-Bar Linkage Kapton Thicknesses of 12.5 μm Flapping at 17.29 Hz, 25 μm Flapping at 22 Hz, and 50 μm Flapping at 25.9 Hz

measured by previous researchers [2, 5, 18]. For an undetermined reason, the original baseline wings constructed for use in this research flapped 3-8 Hz lower compared to identical baseline wings used in previous research.

The 50 μm linkage, although successful in increasing the natural frequency even further, produced vertical forces of the same magnitude as the 12.5 μm linkage design. This can be attributed to the degradation in the general flapping motion of the wing which occurred, to include a vertical bouncing motion and a nearly horizontal angle of attack. A degradation in the correlation between stroke angle and vertical force

can also be seen in Figure 39, along with an unusual pattern of axial and side forces. An unusual amount of yaw moment can be seen as well, as shown in Figure 40.

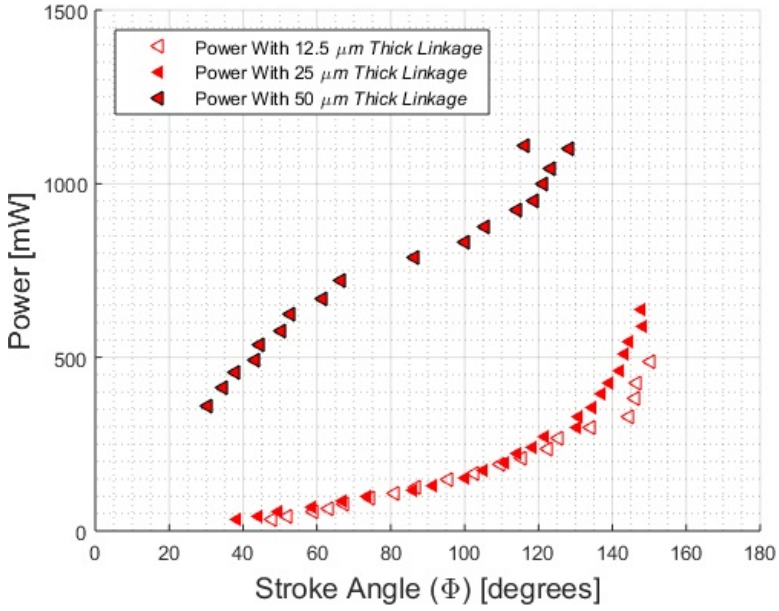

Figure 41. Power of 50 mm Wing with 4-Bar Linkage Kapton Thicknesses of 12.5 μm Flapping at 17.29 Hz, 25 μm Flapping at 22 Hz, and 50 μm Flapping at 25.9 Hz

One effect of increasing the thickness of the linkage, aside from increasing the natural frequency and reducing the stroke angle range, was the increase in power required to operate the wing, show in Figure 41. At a stroke angle of 130 degrees the power consumption increased 300% compared to the original design. However, the 25.9 Hz frequency of the wing was not particularly higher than wings utilized by previous researchers, which suggests the increased power delivered into the system was dissipated in other ways. This included the bending of the thicker Kapton joints, an extremely pronounced vertical bouncing motion of the wing, and an overpronation and oversupination in which the wing violently rotated at the end of each stroke. This excessive rotation led to the wing flapping at a nearly horizontal angle of attack, as shown in Figure 42, which inhibited the wing from producing greater vertical force

than it did at lower frequencies. Furthermore, the wing failed at the rotation joint very quickly.

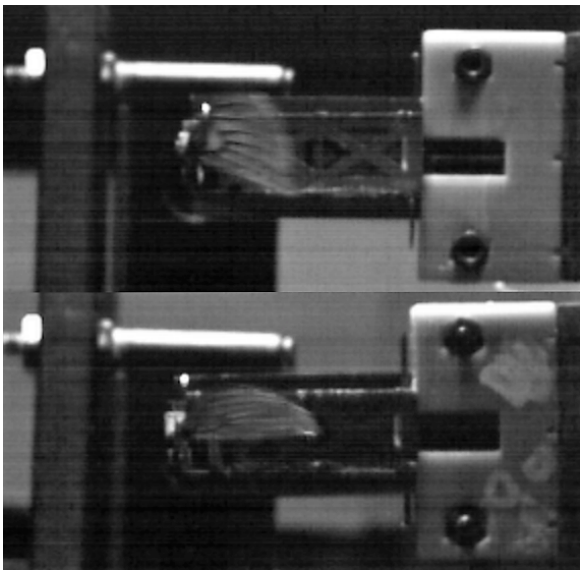

Figure 42. Angle of Attack Comparison for 12.5 μm Linkage (Top) and 50 μm Linkage (Bottom)

The results showed a limit to the benefits of increasing the natural frequency of the wing. The kinetic energy of the wing correlates with the velocity squared, while the mass simply correlates linearly. This means raising the natural frequency increases the kinetic energy much more than increasing the mass does. Instead of simply contributing to the smooth pronation and supination motion, the excess kinetic energy also contributed to vertical bouncing and a near horizontal angle of attack, which hindered vertical force production. The AFIT FWMAV design failed to operate as designed when excessive power was delivered to the system.

4.5 Altered Wings and Linkages

After the promising results of the new linkages, preliminary tests were conducted at maximum driving amplitude for each wing size with the two linkages, to determine

which linkage produced the maximum vertical force for each wing. The 50 μm linkage was chosen for the 55 mm and 60 mm wing, while the 25 μm linkage was chosen for the 65 mm and 70 mm wing. An additional test sweep was conducted for the 70 mm wing with the 50 μm linkage, as this would provide an upper limit for Reynolds number calculations. Table 3 shows the wing length, linkage thickness, natural frequency, and normalized wingtip velocity of the new wing designs.

Table 3. Wing Length, Wing Mass, and Natural Frequency of Modified Wing Designs With an Aspect Ratio of 14.42

Wing Length (mm)	4-Bar Linakge Thickness (μm)	Natural Frequency (Hz)	Normalized Wingtip Velocity
50	12.5	17.29	1.0
55	50	22.794	1.44
60	50	19.65-20.44	1.35-1.41
65	25	11	0.82
70	25	9.43	0.75
70	50	15.72	1.25

The driving amplitude was driven slightly past 1.0, or 200 volts, for several of the wings. For many of the designs neither the vertical force nor the stroke angle were maximized at the maximum driving amplitude. Therefore, the user interface GUI was changed to permit driving amplitudes of up to 1.2. This was deemed acceptable for three reasons. First, the voltage remained below the maximum voltage of the amplifier and NI Box. Second, the stroke angle was below the design limit, meaning further increasing the driving amplitude would not lead to structural damage to the linkage or the wing. Third, a new piezo was used for each test sweep, meaning any damage incurred by the piezo would not influence any other tests.

Another unforeseen alteration which had to be made was the use of a 45 degree angle stop for the 55 mm test. Every other test successfully used the 60 degree angle stop. However, the 55 mm wing failed to properly increase vertical forces with increasing driving amplitude. It was determined the wing flapped with a nearly horizontal angle of attack, which would prevent a LEV from properly forming and attaching to the wing. This was similar to the problem seen with the 50 mm wing with the 50 μm linkage. Therefore, the 45 degree angle stop was used only for the 55 mm wings. Figures 43, 44, and 45 illustrate the forces, moments, and power consumption of the new wing designs.

Because of the varying frequencies and wing lengths, there was not a clearly delineated progression of vertical force with increasing wing length. For example, the 65 mm 11 Hz wing and the 70 mm 9.43 Hz wing both produced roughly similar vertical forces to the 50 mm 22 Hz and 55 mm 15.72 Hz wings. However, there were two designs which produced clearly superior forces. The 55 mm 22.794 Hz wing with the 45 degree angle stop produced vertical forces between 300 and 650 mg F greater than the original wing for a given stroke angle. The 70 mm 15.72 Hz wing produced vertical forces between 250 and 800 mg F greater than the original wing for a given stroke angle. This wing produced vertical forces nearly 190% higher than the original wing at a stroke angle of 105 degrees, and likely would have produced even greater forces if the stroke angle was not constrained due to the thicker linkage. The increased vertical force was also accompanied by increased moments as well as extremely high power consumption.

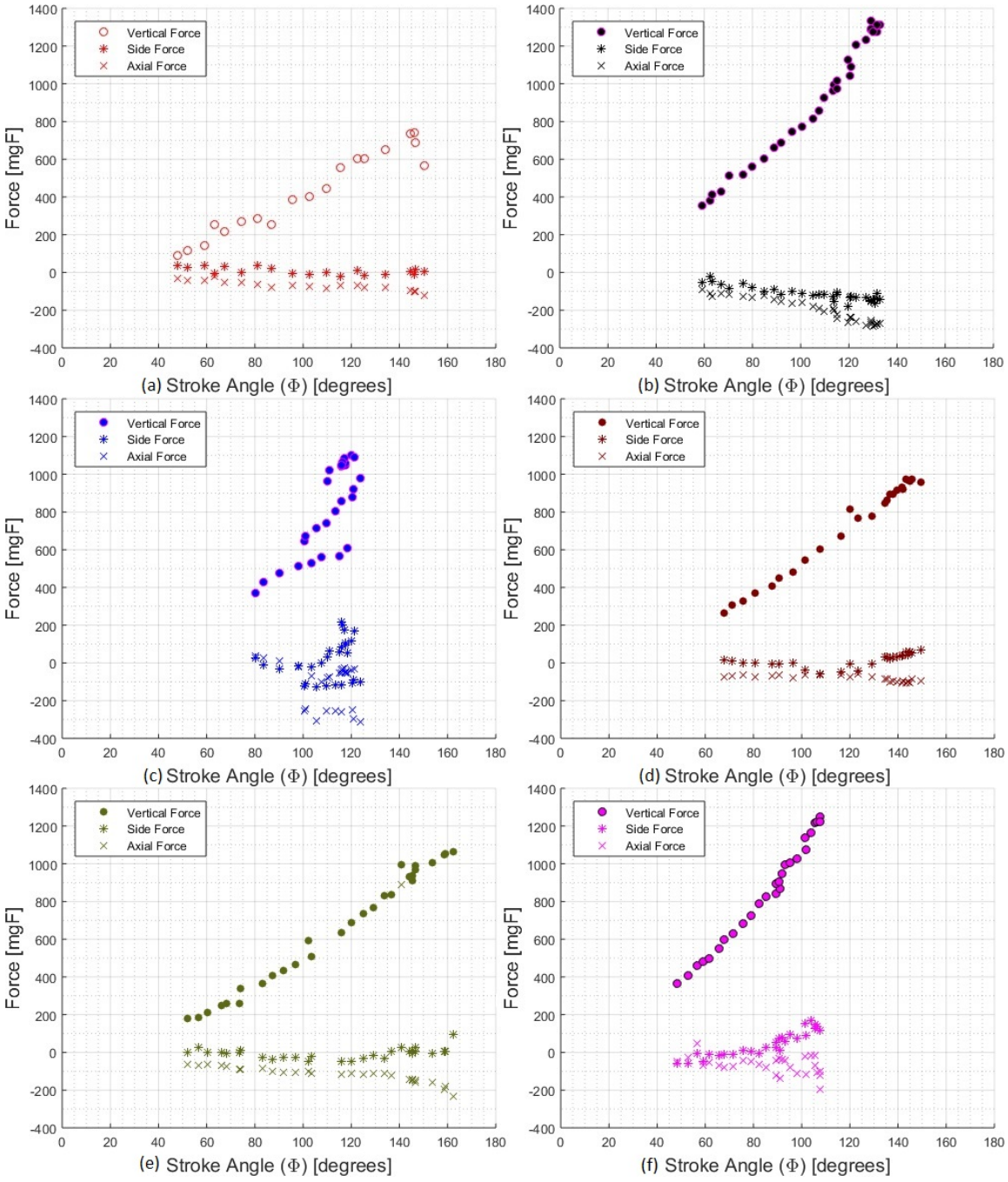

Figure 43. Forces: 50 mm 17.29 Hz Wing with 12.5 μm Linkage, 55 mm 22.794 Hz Wing With 50 μm Linkage and 45 Degree Angle Stop, 60 mm 19.65-20.44 Hz Wing with 50 μm Linkage, 65 mm 11 Hz Wing with 25 μm Linkage, 70 mm 9.43 Hz Wing with 25 μm Linkage, 70 mm 15.72 Hz Wing with 50 μm Linkage

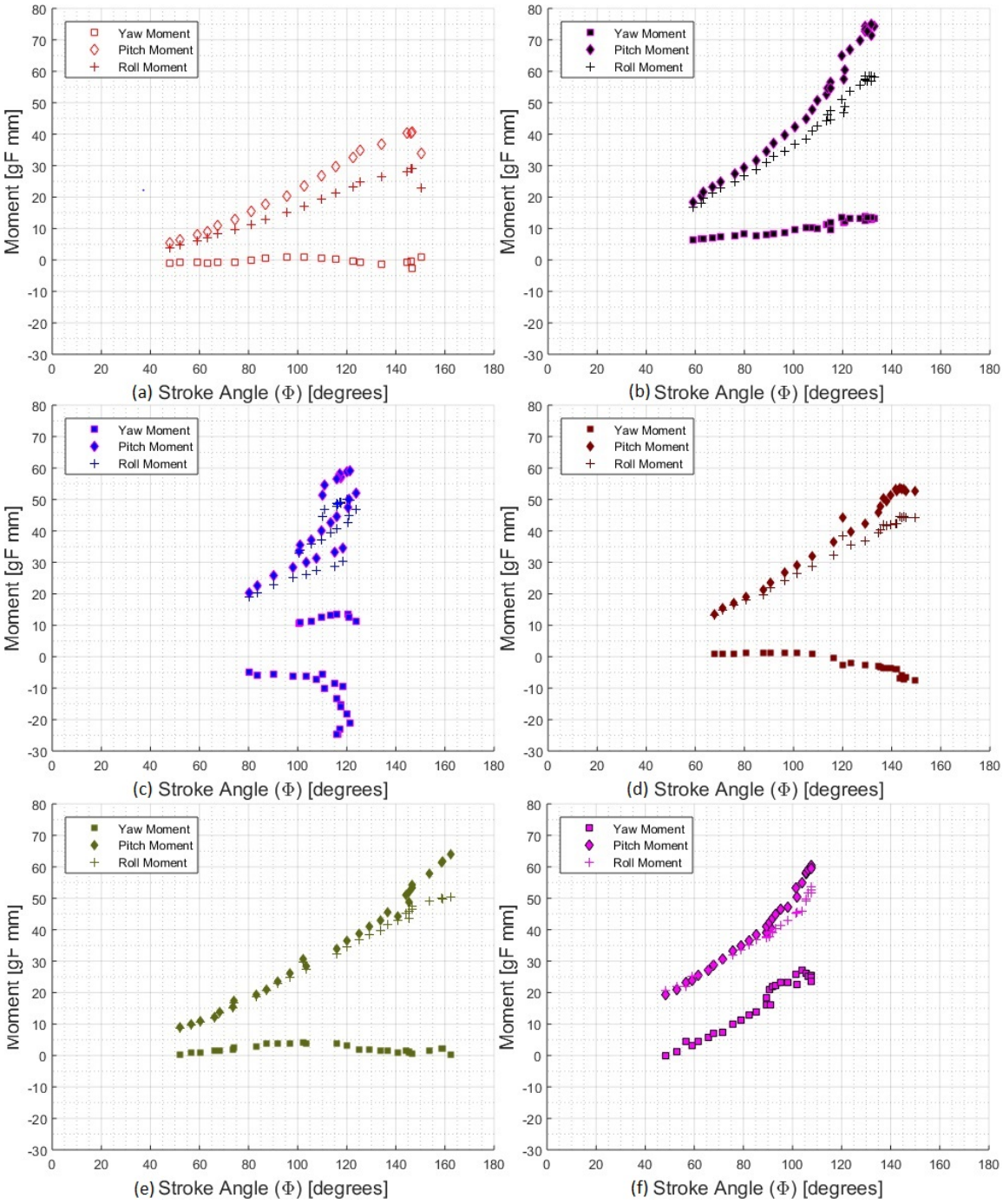

Figure 44. Moments: 50 mm 17.29 Hz Wing with 12.5 μm Linkage, 55 mm 22.794 Hz Wing With 50 μm Linkage and 45 Degree Angle Stop, 60 mm 19.65-20.44 Hz Wing with 50 μm Linkage, 65 mm 11 Hz Wing with 25 μm Linkage, 70 mm 9.43 Hz Wing with 25 μm Linkage, 70 mm 15.72 Hz Wing with 50 μm Linkage

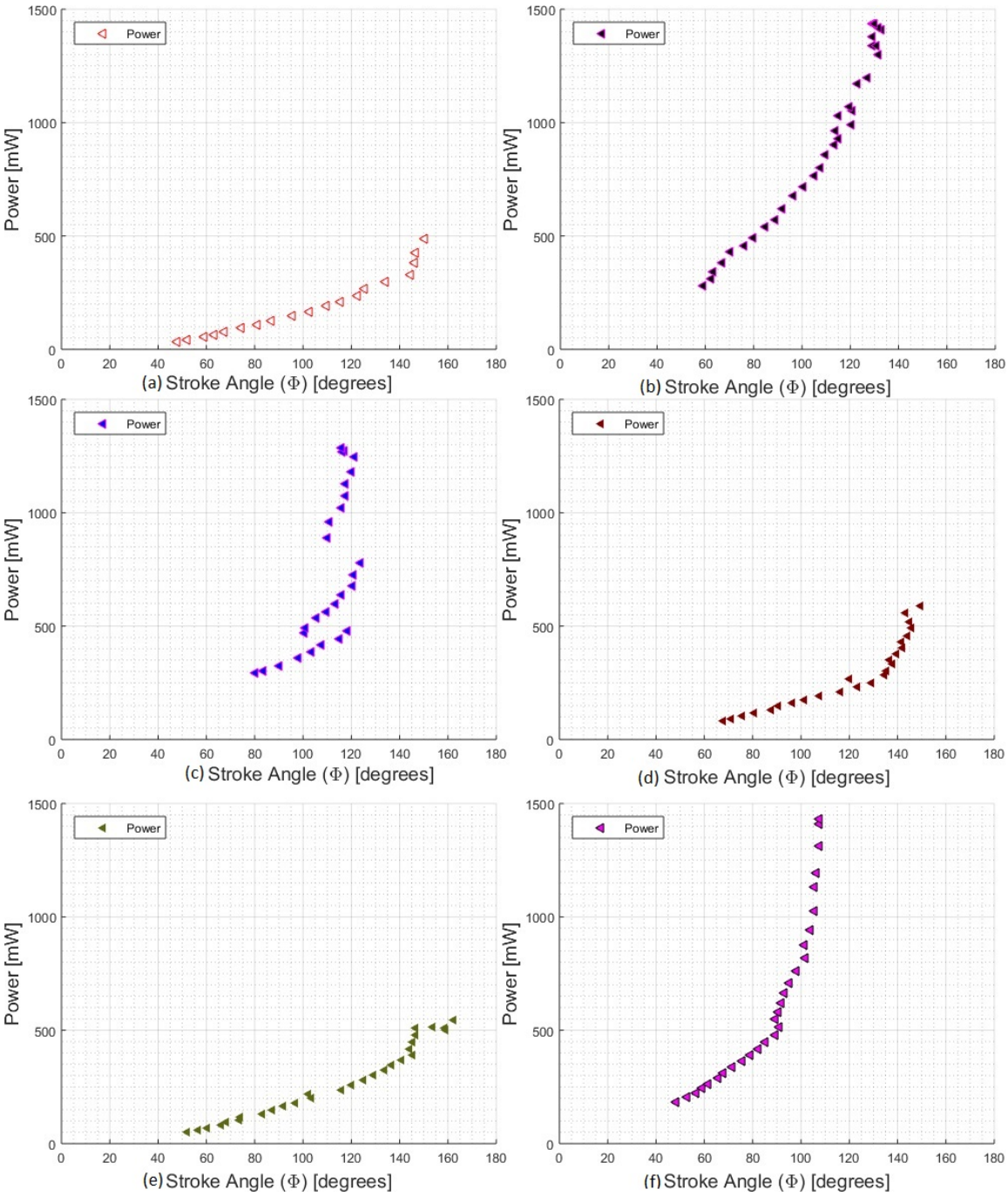

Figure 45. Power: 50 mm 17.29 Hz Wing with 12.5 μm Linkage, 55 mm 22.794 Hz Wing With 50 μm Linkage and 45 Degree Angle Stop, 60 mm 19.65-20.44 Hz Wing with 50 μm Linkage, 65 mm 11 Hz Wing with 25 μm Linkage, 70 mm 9.43 Hz Wing with 25 μm Linkage, 70 mm 15.72 Hz Wing with 50 μm Linkage

Table 4 compares the vertical force and power consumption of the original wing to the two best improved designs. At a stroke angle of 105 degrees, the new designs increased the vertical force by 96% and 188%, while the power consumption increased by 340% and 473%. It is unclear how much of the increase in power can be attributed to overcoming drag, rather than overcoming the inertia of the thicker Kapton.

Table 4. Vertical Force and Power Consumption of Original Design vs Two Best Improved Designs at 105 Degree Stroke Angle

Wing Length (mm)	4-Bar Linakge Thickness (μm)	Natural Frequency (Hz)	Normalized Wingtip Velocity	Vertical Force (mg F)	Power (mW)
50	12.5	17.29	1.0	417	174
55	50	22.794	1.44	817	766
70	50	15.72	1.25	1200	997

A clear advantage to increasing the size of the wing, rather than simply increasing the natural frequency of a 50 mm wing, was a longer service life and smoother flapping motion. The original wing flapping at higher frequencies had choppy flapping motion and quick failure at the passive rotation joint. In comparison, the 65 and 70 mm wings flapped through a full driving amplitude sweep without breaking. Therefore, testing has definitively shown increasing the size of the wing while forestalling the drop in natural frequency is a preferable means of increasing vertical force compared to simply increasing the flapping frequency of a 50 mm wing.

4.6 Nano-17 Extension Cord

The vacuum tests, taken to calculate Reynolds number, took place with extension cords used to attach the Nano-17 to the NI Box. The use of these extension cords led to a reduction in the precision of the force and moment data being collected. To

ascertain the effect the extension cord had on data collection, a single wing was tested at various driving amplitudes with and without the extension cord attached. The wing was flapped at a certain driving amplitude with the extension cord, and then flapped again at the same driving amplitude without the extension cord to compare the two configuration. Figure 46 shows the differences in forces and moments measured with and without the extension cord. The differences in measured side force, yaw moment, pitch moment, and roll moment showed no particular pattern, suggesting that when mean values are considered, the data taken with the extension cable is as accurate as the data taken without the extension cable.

The vertical force and axial force show a very slight bias towards positive values. However, great variability exists at different driving amplitudes, and the vertical force and axial force graphs in Figure 46 seem to show no pattern besides the small positive bias. This suggests that despite the extension cord reducing the precision of the measurements taken from the Nano-17, the average values are still a largely accurate reflection of the forces and moments.

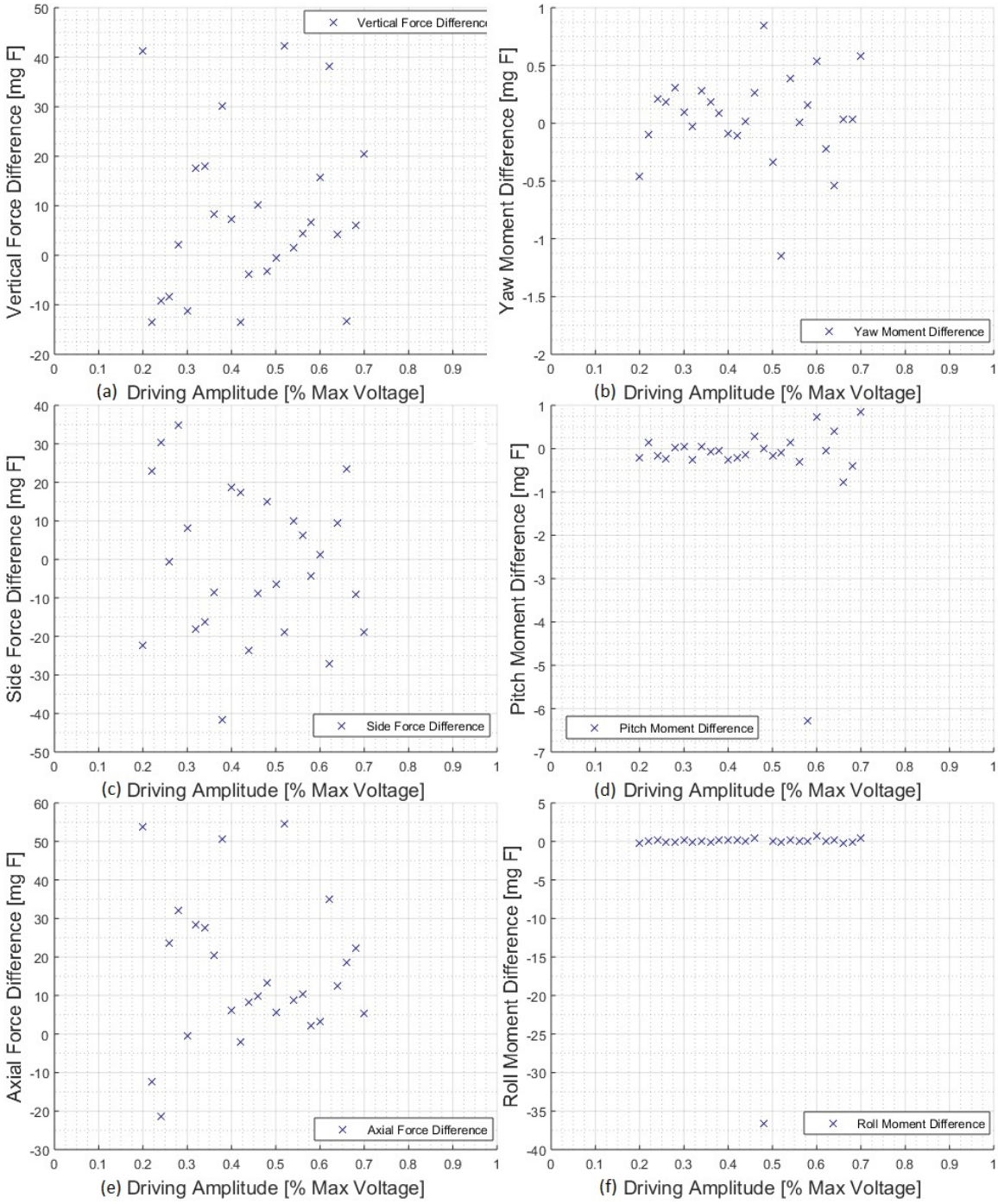

Figure 46. Difference in Vertical Force, Yaw Moment, Side Force, Pitch Moment, Axial Force, and Roll Moment of 50 mm Wing With and Without an Extension Cord, with the Extension Cord Value Subtracted From the Non-Extension Cord Value

4.7 Vacuum Tests

In an effort to examine the effect of altering the Reynolds number of the wing, air density tests were conducted at values of 85, 70, 55, and 25% of atmospheric pressure. To account for the inherent differences in the individual wing specimens, each wing was first flapped at five or six discrete driving amplitudes at atmospheric pressure to provide reference values. The number of test points was limited to five or six for the atmospheric testing because a full driving amplitude sweep would have led to the wing breaking before it could be used for flapping under partial vacuum conditions. Figures 47, 48, and 49 give the forces, moments, and power measurements for the five partial vacuum tests.

There were a few notable patterns. The stroke angle did not necessarily increase linearly with the driving amplitude, as will be shown graphically later in this chapter. At a narrow band of driving amplitudes, the movement within the 4-bar linkage would interfere with the general flapping motion, leading to undesirable flapping patterns. These patterns included such phenomena as the stroke angle cyclically varying from one flap to the next or the upstroke behaving differently from the downstroke. This behavior most likely arose because the reduction in air density led to a corresponding reduction in the damping effect provided by the air. The only way to prevent these phenomena was to bias the flapping in a particular direction until the undesirable flapping motion stopped. This successfully prevented the undesirable flapping patterns but did result in asymmetric flapping, as well as a non-linear relationship between driving amplitude and stroke angle.

There was a clear pattern of vertical force increasing at a slower rate under partial vacuum as stroke angle was increased, with the maximum stroke angle occurring at lower driving amplitudes. There was also a pattern of power consumption decreasing with decreasing air density, due to the decrease in drag. The power data under partial

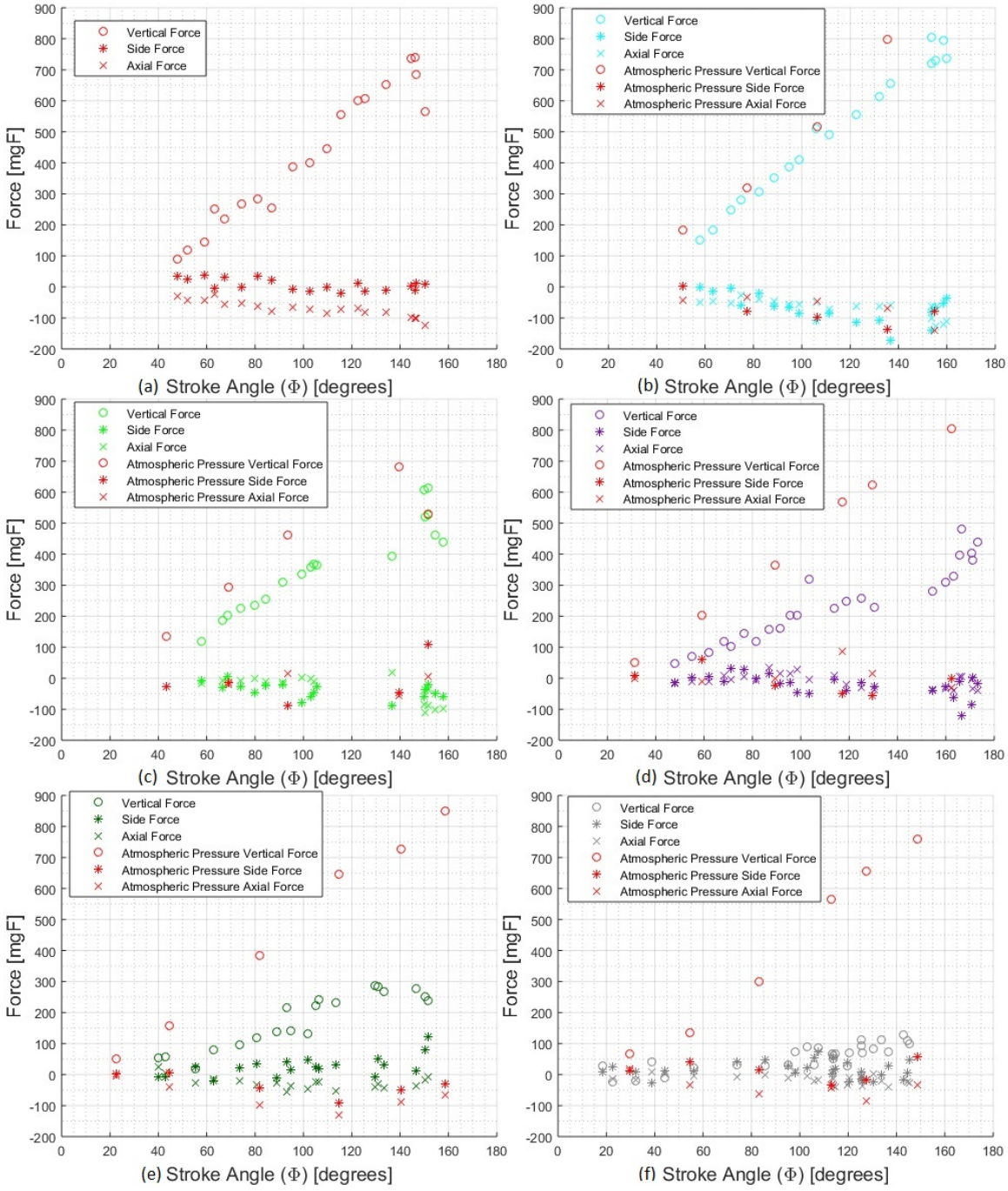

Figure 47. Forces of 50 mm Wing at 100% atm and 17.29 Hz, 85% atm and 18.84 Hz, 70% atm and 18.86 Hz, 55% atm and 16.51 Hz, 40% atm and 18.08 Hz, and 25% atm and 18.05 Hz

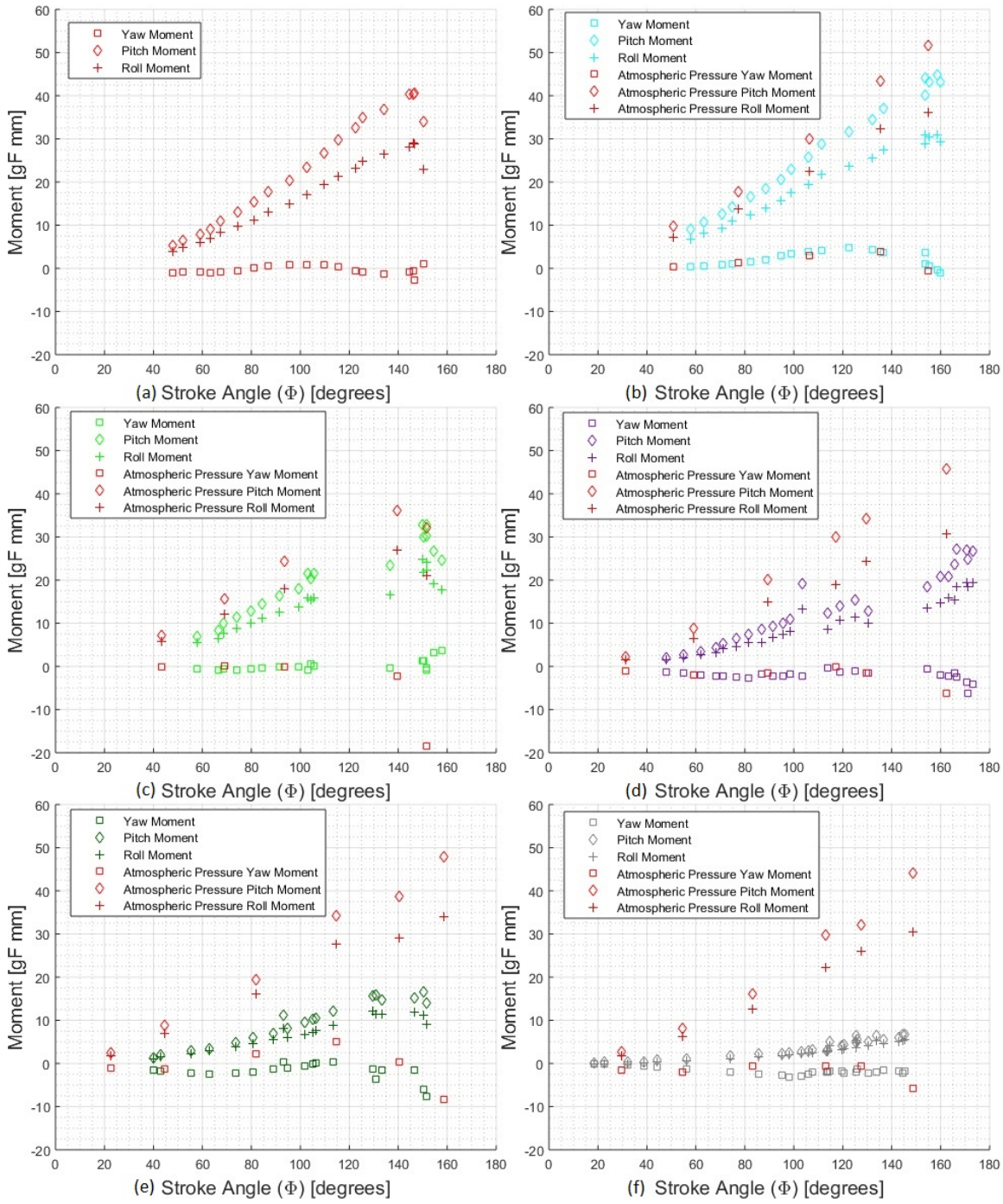

Figure 48. Moments of 50 mm Wing at 100% atm and 17.29 Hz, 85% atm and 18.84 Hz, 70% atm and 18.86 Hz, 55% atm and 16.51 Hz, 40% atm and 18.08 Hz, and 25% atm and 18.05 Hz

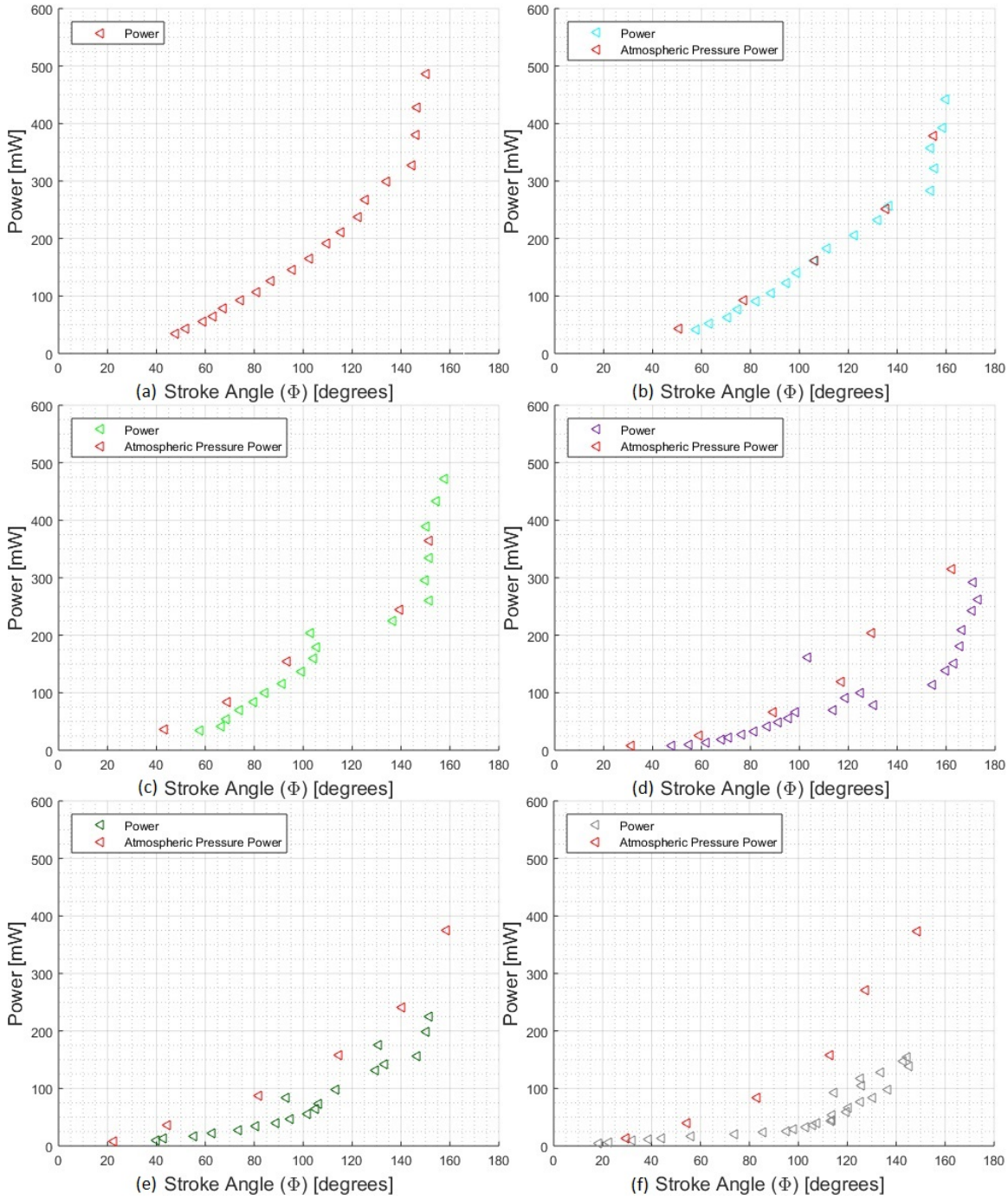

Figure 49. Power of 50 mm Wing at 100% atm and 17.29 Hz, 85% atm and 18.84 Hz, 70% atm and 18.86 Hz, 55% atm and 16.51 Hz, 40% atm and 18.08 Hz, and 25% atm and 18.05 Hz

vacuum was more scattered than expected, due to the previously delineated issue of a non linear relationship between driving amplitude and stroke angle.

Although this data was primarily collected for Reynolds number effect analysis, other useful information can also be determined from this data. For example, at high altitudes and high temperatures, the density of air can reach the air densities tested at in this research, to include 55% of atmospheric air density. Such atmospheric conditions can occur in areas such as the Tora Bora region of Afghanistan, where altitudes can reach 14,000 feet or over 4200 meters, and temperatures exceed 90 degrees Fahrenheit, which is approximately 305 Kelvin. These tests show lower air density leads to a decrease in vertical force, and a decrease in power consumption. This suggests a FWMAV's lift capabilities must be over-designed at sea level for it to remain operational in high altitude, high temperature environments. Otherwise, it would fail to fly under such conditions, rendering it useless.

4.8 Near Absolute Vacuum Test

A test was conducted at the lowest attainable air pressure, which was 4.3 torr, to determine the purely inertial behavior of the biomimetic wing. 4.3 torr is equivalent to 573 Pa, or 0.57% of atmospheric pressure. Figures 50, 51, and 52 compare the forces, moments, and power consumption of the wing under near absolute vacuum to the wing behavior under atmospheric pressure. Figure 50 shows under purely inertial movement, the 50 mm wing produces negligible cycle-averaged forces. Most of the test points occur at stroke angles between 90 and 125 degrees, as a driving amplitude sweep between 0.05 and 0.3 led to the wing flapping primarily in that particular stroke angle range. In this range of stroke angles the vertical force would randomly vacillate between -40 and 40 mg F, while the original wing in atmospheric conditions produced vertical forces increasing linearly from 365 to 600 mg F. The negligible

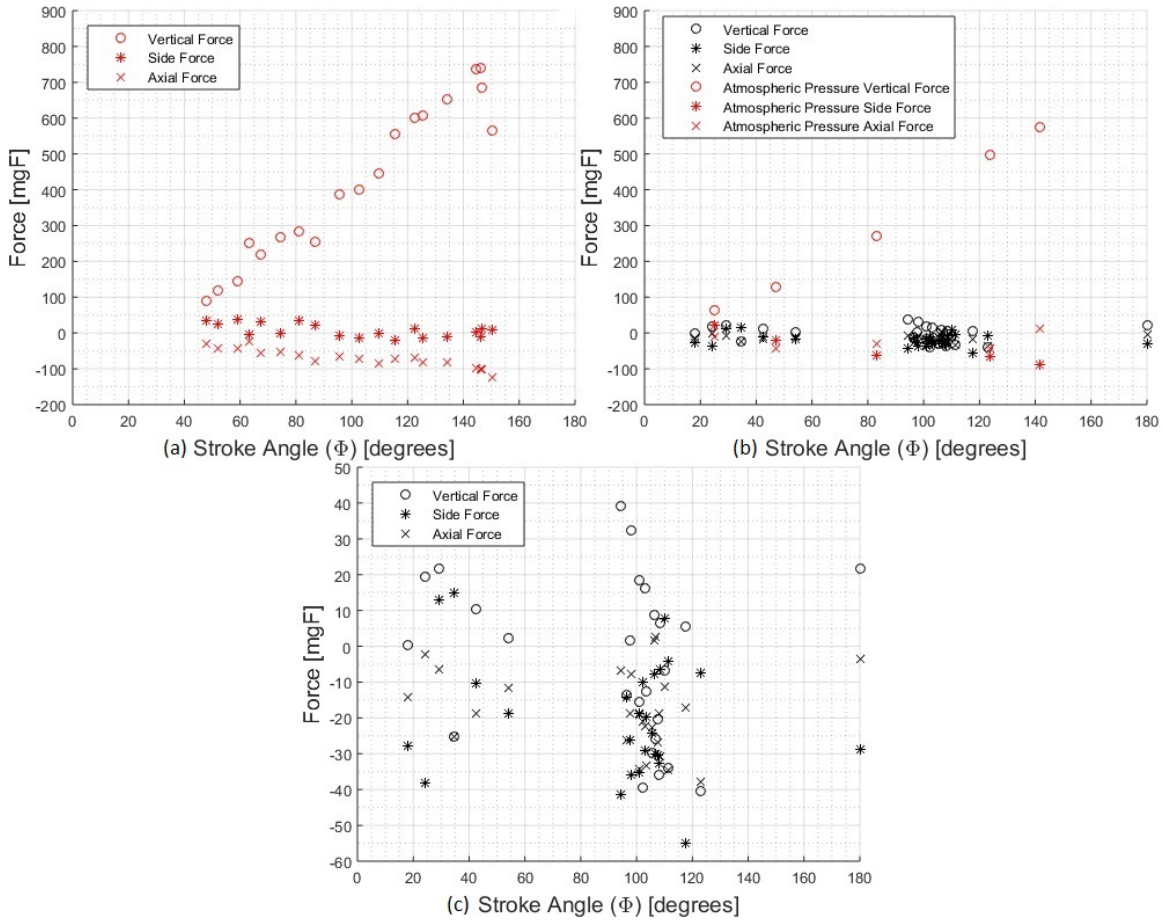

Figure 50. Comparison of Forces of 50 mm Wing at 100% atm and 17.29 Hz, 0.57% atm and 17.29 Hz, and 0.57% atm and 17.29 Hz with Altered Y-Axis Range

cycle-averaged forces produced by the wing under purely inertial movement reveal the force data collected for the biomimetic wing truly reflects the aerodynamic forces of the wing. The data is not altered by either the effects of the wing movement itself, or the movement of the vibrating piezo. The moments, pictured in Figure 51, show slightly more of a pattern. There is a roughly linear relationship between stroke angle and roll moment. However, the maximum roll moment under vacuum was 1.15 gF mm, compared to a maximum roll moment of 26.01 gF mm for the same wing under atmospheric pressure. Thus, even the maximum roll moment under vacuum was only 4.4% of the maximum roll moment under atmospheric pressure. The same general

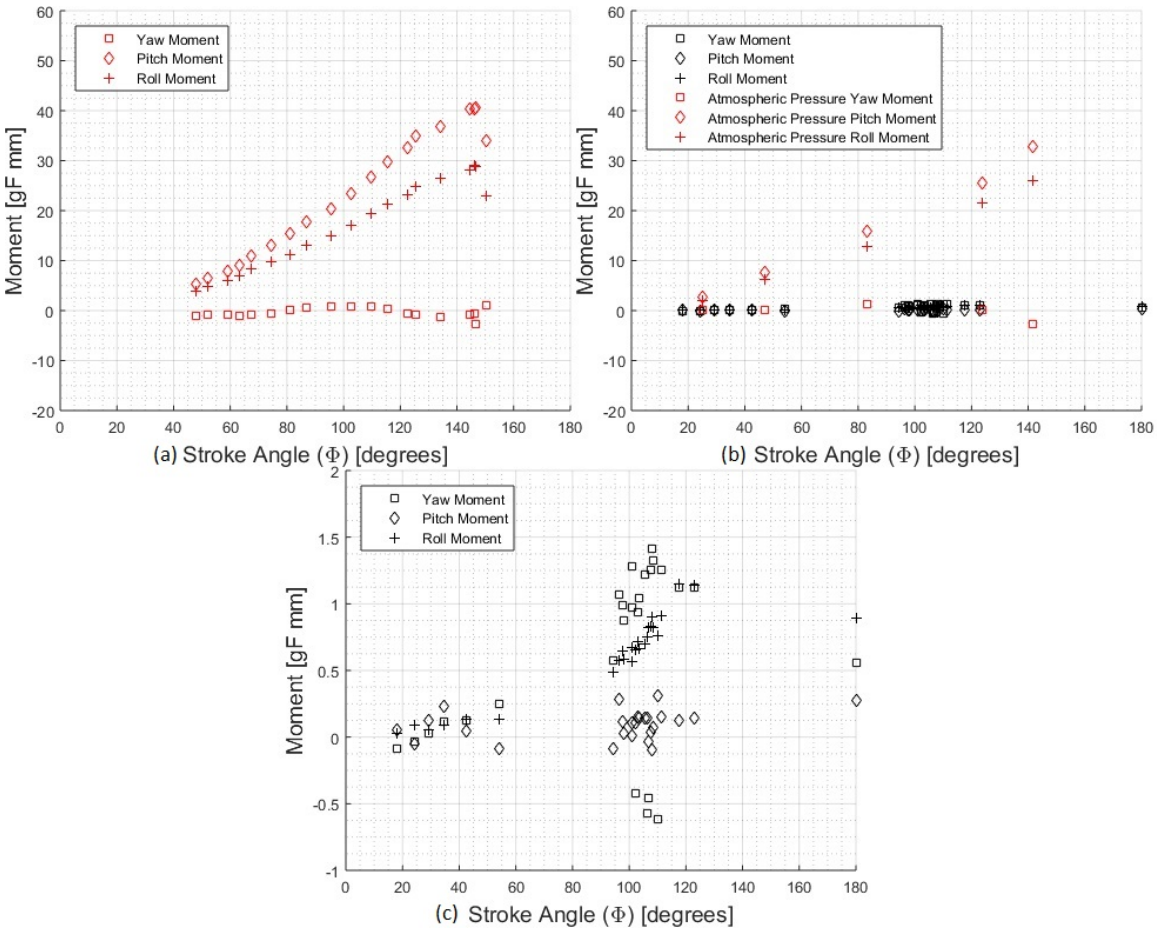

Figure 51. Comparison of Moments of 50 mm Wing at 100% atm and 17.29 Hz, 0.57% atm and 17.29 Hz, and 0.57% atm and 17.29 Hz with Altered Y-Axis Range

pattern arose with moments as with forces, with negligible cycle-averaged moments measured under purely inertial motion. The lack of forces and moments produced by the wing and the piezo suggest future researchers can use data collected by past researchers while utilizing new piezo designs. The use of a piezo of differing weight or dimensions will not necessitate any inertial correction to previous force and moment data.

Figure 52 compares the power consumption of the wing under atmospheric pressure and near vacuum pressure. A distinct s-shape exists for the vacuum power curve,

which is the result of a large portion of the driving amplitude sweep occurring under a narrow stroke angle range. The maximum power consumption was 70 mW at a stroke angle of 180 degrees under vacuum conditions, while the original wing had a power consumption of 487 mW at a stroke angle of 150 degrees.

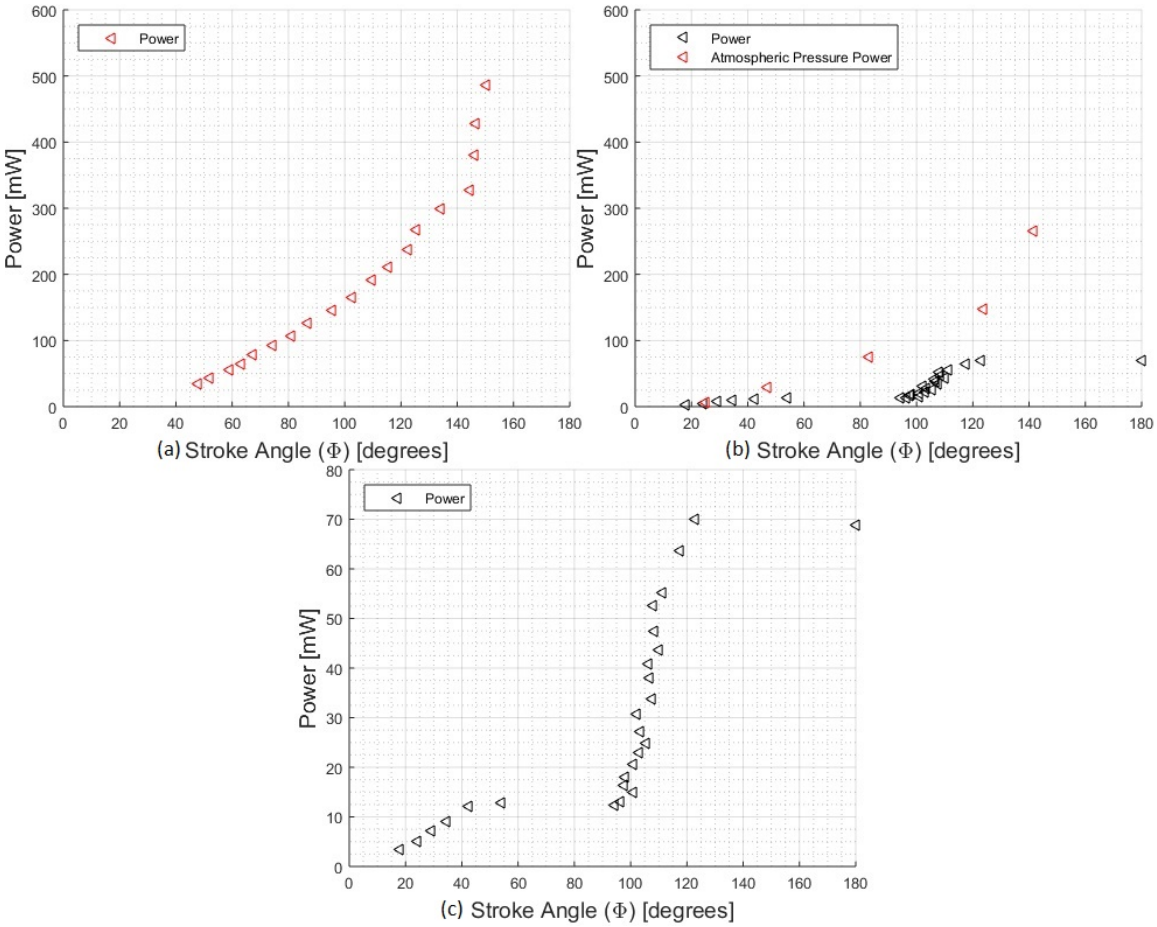

Figure 52. Comparison of Power of 50 mm Wing at 100% atm and 17.29 Hz, 0.57% atm and 17.29 Hz, and 0.57% atm and 17.29 Hz with Altered Y-Axis Range

The dramatic increase in power consumption seen with increasing stroke angle in most of the atmospheric tests can be attributed to the wings' interaction with the air, rather than an increase in the kinetic energy of the wing. At a stroke angle of 150 degrees, the vacuum test consumed 14.6% of the power consumed for the atmospheric

pressure test. Although there are small energy savings made by decreasing the weight of the wing, most of the energy consumption is inextricably tied to the production of aerodynamic forces.

4.9 Reynolds Number

Equation 8 provides the formulation for Reynolds number. The dynamic viscosity was calculated with Sutherland's Law, which calculates the viscosity of the air using the temperature in comparison to a reference viscosity (μ_{ref}), reference temperature (T_{ref}), and a constant (χ), which are all known values for air [21].

$$\mu = \mu_{ref}(\frac{T}{T_{ref}})^{1/2}\frac{1+\frac{\chi}{T_{ref}}}{1+\frac{\chi}{T}} \tag{13}$$

The Reynolds number ranges from 1.58 for the near absolute vacuum test to 3168 for the 55 mm wing flapping at 22.79 Hz at a 130 degree stroke angle. For each test point the Reynolds number is compared to both the vertical force and the nondimensionalized vertical force coefficient. The nondimensionalized vertical force equation is shown below.

$$Cv = \frac{VerticalForce}{qS} \tag{14}$$

$$q = \frac{1}{2}\rho V^2 \tag{15}$$

$$Cv = \frac{VerticalForce}{\frac{1}{2}\rho V^2 S} \tag{16}$$

The nondimensionalized vertical force compares the vertical force produced to the dynamic pressure (q) and planform area (S) of the wing. Figure 53 shows the

Reynolds number data for the original 50, 55, and 60 mm wings.

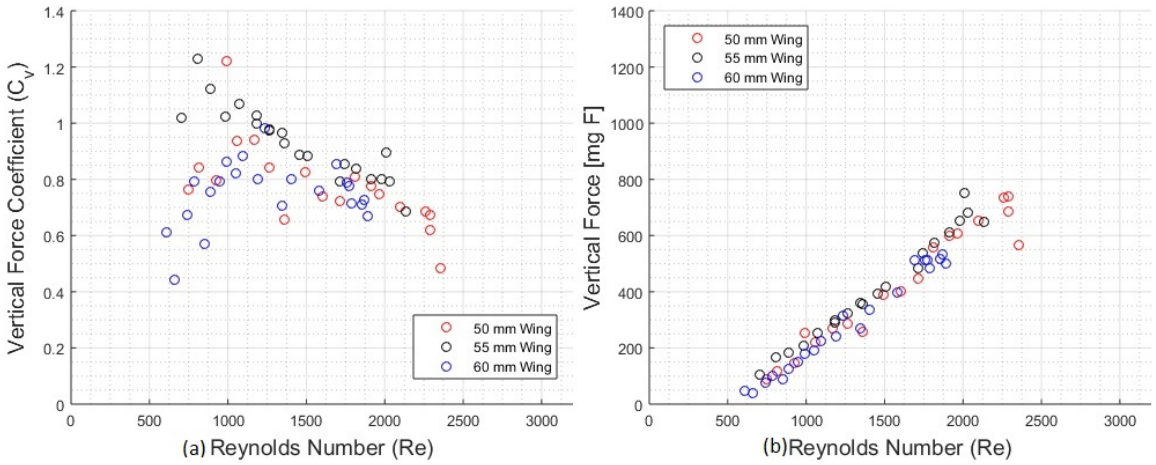

Figure 53. Reynolds Number Data of 50, 55, and 60 mm Wings with Original Linkages. Vertical Force is Shown on the Left, and Vertical Force is Shown on the Right

The vertical force coefficient peaks at 1.22 for the 50 mm wing at Re=990, at 1.23 for the 55 mm wing at Re=805, and at 0.98 for the 60 mm wing at Re=1236. There is a clear pattern of the coefficient rising sharply, peaking at between 805 and 1236, and then steadily declining. This suggests at a certain point the dynamic pressure and wing area increase at a greater rate than the vertical force. The vertical force graph shows a clear overlap between the data of all three wings, which suggests the vertical force linearly correlates with the Reynolds number. The overlap suggests Reynolds number can be used to directly predict the vertical force capabilities of a wing, regardless of the wing length or natural frequency. Figure 54, shown below, compares the 50 mm wing behavior with the three separate linkages.

The 50 mm wing with the 50 μm linkage shows atypical behavior. This particular wings has much lower vertical force coefficient values as well as much lower vertical force values. Although the 12.5 μm linkage and 25 μm linkage 50 mm wings both have overlapping data points for vertical force, the 50 μm linkage has a much shallower curve, meaning the vertical force increases more slowly as Reynolds number increases.

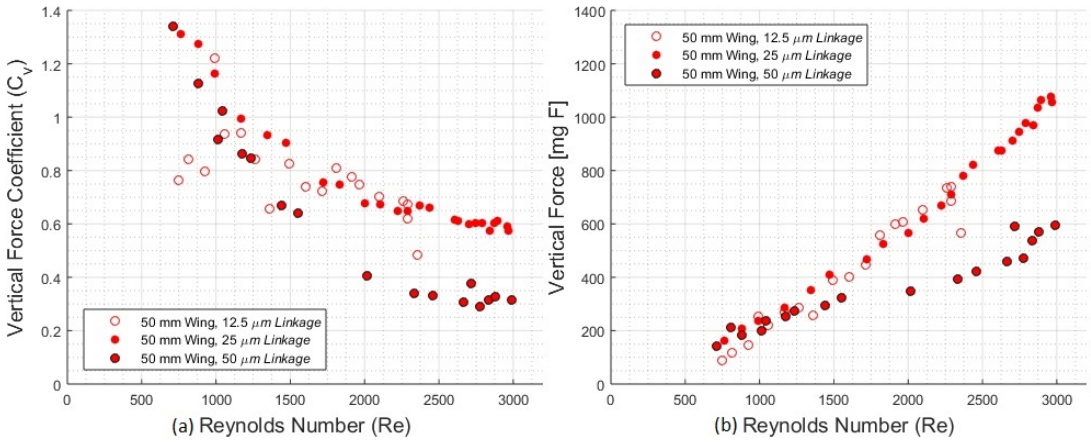

Figure 54. Reynolds Number Data of 50 mm Wing with Three Separate Linkages. Vertical Force is Shown on the Left, and Vertical Force is Shown on the Right

This is in line with the previously shown data comparing the three linkage designs, wherein the 50 μm design led to degraded performance despite a higher wingtip velocity. Figure 55 shows the Reynolds number data for the longer wing designs with thicker linkages.

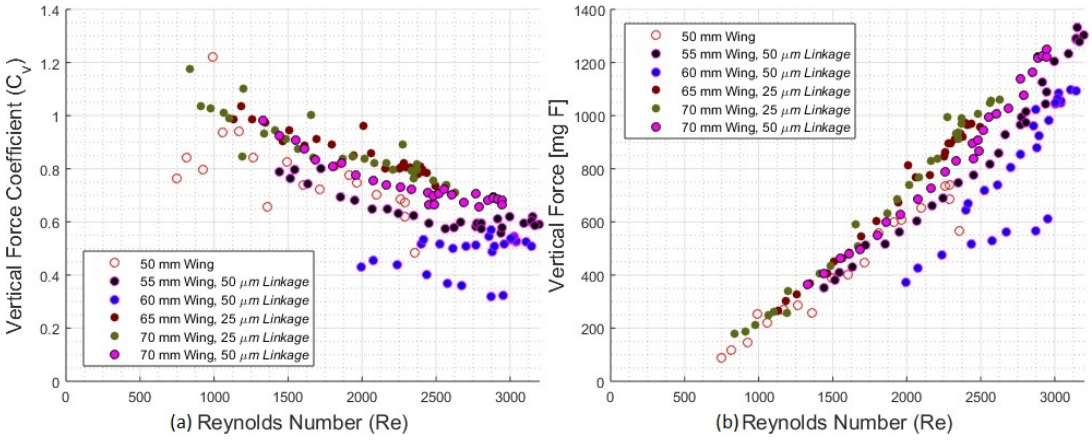

Figure 55. Reynolds Number Data of Wings of Various Sizes and Linkages at Atmospheric Pressure. Vertical Force is Shown on the Left, and Vertical Force is Shown on the Right

The same general pattern is seen, with C_v maximimzing at about Re=1000 after

which it steadily decreases. The vertical force graph shows the same pattern as before with a large amount of overlap, with the exception of the 60 mm wing. The 60 mm wing behavior can be attributed to the use of multiple wings which operated under various flapping frequencies, temperatures, and angles of attack. Figure 56 shows the Reynolds number data for the partial vacuum tests.

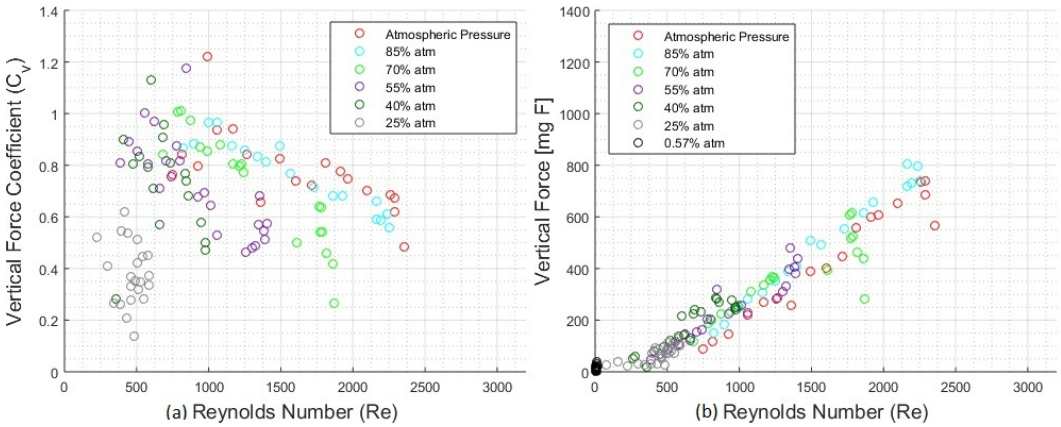

Figure 56. Reynolds Number Data of Vacuum Tests. Vertical Force is Shown on the Left, and Vertical Force is Shown on the Right

The vertical force graph again shows a clear trend of Reynolds number and vertical force correlating regardless of specific test conditions. The C_v graph, however, is much less coherent than even the previous C_v graphs. However, the same general pattern of C_v peaking between Re=500 and Re=1200 continues. For 85% atm, C_v reaches 0.966 at Re=1059. For 70% atm, C_v reaches 1.01 at Re=810. For 55% atm, C_v reaches 1.18 at Re=841. For 40% atm, C_v reaches 1.13 at Re=602. At 25% of atmospheric pressure, no clear pattern exists except the Reynolds number clustering near Re=500. The 0.57% atm data, and portions of the 25% and 40% data, were removed from the C_v graph, because at extremely low air densities the C_v values would become too high. Figure 57 combines all of the previously shown graphs and thereby presents every test point together. The C_v shows a large variability for a given Reynolds number. There

is, however, a rough trend of C_v peaking at a Reynolds number between 500 and 1200. The vertical force, on the other hand, clearly correlates with the Reynolds number for almost all tests points.

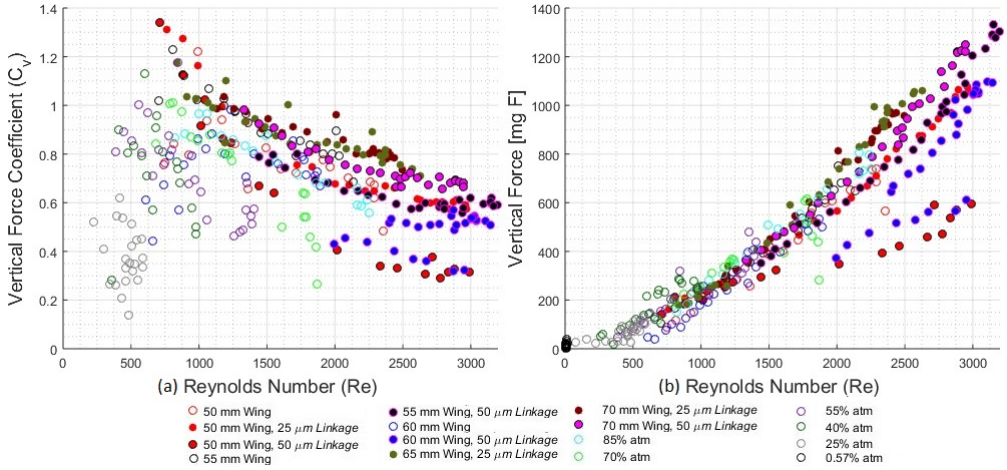

Figure 57. Reynolds Number Data of All Test Points. Vertical Force is Shown on the Left, and Vertical Force is Shown on the Right

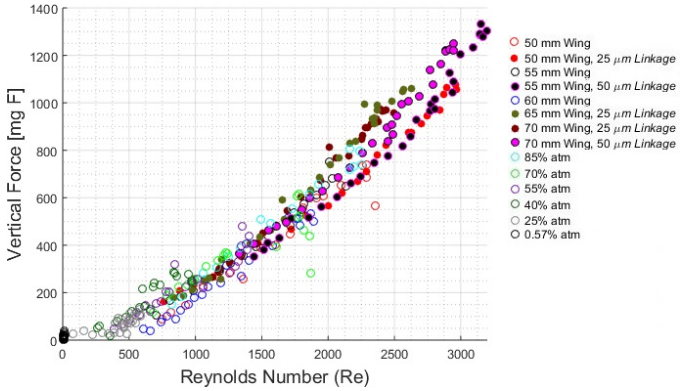

Figure 58. Reynolds Number vs Vertical Force for All Test Cases Except the 60 mm Wing With the 50 μm Linkage and 50 mm Wing With the 50 μm Linkage

Figure 58 shows the same graph with two outlying test conditions removed. The correlation between Reynolds number and vertical force becomes even more clear, showing the best way to increase the vertical force production of a wing is to increase the Reynolds number. The Reynolds number correlates with the following wing characteristics:

$$Re \propto \frac{fR^2}{\text{Æ}R} \tag{17}$$

Research has shown the decrease in frequency associated with an increase in wing length can be attenuated by increasing the stiffness to mass ratio of the flapper joint system.

4.10 Stroke Angle Measurement and Symmetry

The previous chapter details the process used to achieve symmetric flapping for all tests. The tables in the Appendix show the symmetry data for all tests. This includes comparisons of the up and down stroke angles as well as the total stroke angle and difference in stroke angle.

For wings flapping under atmospheric pressure, the difference between upstroke and downstroke angle remained under 5 degrees for most driving amplitudes. At the highest driving amplitudes the asymmetry increased, as the carbon fiber flapper base prevented the wing from flapping beyond 72.5 degrees on the downstroke. This led to an upstroke bias for the highest stroke angles. For the tests conducted under the highest driving amplitudes, the wing would routinely hit the carbon fiber base, which ultimately led to wing failure. However, this had a negligible effect on the vertical force of the wing, as long as the total stroke angle increases in a linear fashion.

Wings flapped under partial vacuum tended to fail to flap properly under a certain range of driving amplitudes. This occurred because the reduction in damping provided by the air led to the 4-bar linkage interfering with the flapping motion of

the wing. This would lead to various irregular flapping patterns. In these conditions proper flapping returned when the wing was biased in a certain direction, which led to sinusoidal, yet asymmetric flapping. This led to the notable asymmetry at those driving amplitudes. For example, the wing at 25% of atmospheric pressure has extremely asymmetric flapping from a driving amplitude of 0.275 to 0.35. As in the case of the variable sized wings, the total stroke angle continued to increase in a roughly linear fashion, meaning that there was a biasing of the flapping concurrent with an desired increase in stroke angle.

The near absolute vacuum test provided the most non linear results. The stroke angle increased steadily from a driving amplitude of 0.05 to 0.1, and then jumped suddenly from 54 to 94 degrees at a driving amplitude of 0.11. The stroke angle then proceeded to increase in extremely small increments until the driving amplitude reached 0.3, at which point it jumped another 67 degrees. The difference in upstroke and downstroke remained small when the wing was increasing stroke angle in small increments, while the asymmetry was greater at very high and very low driving amplitudes. This pattern again shows that the 4-bar linkage does not operate properly under atypical air densities. This is understnadable, as the linkage was designed for flapping at atmospheric pressures.

The stroke angle was also calculated automatically using the MATLAB code developed by DeLuca, using the OptoNCDT displacement sensor and Equation 5 [5]. This method of calculation is useful for giving a rough estimate of the behavior of the wing during tests. However, in practice there is clear difference between both the stroke angle, and the asymmetry measured by the displacement sensor. There are several possible reasons for this. The displacement sensor makes the most accurate stroke angle calculations when the laser is pointed at the tip of the piezo. Quite often the laser would be pointed a few centimeters below the tip of the piezo, usually to

avoid pointing at excess bonding adhesive. Also, the 4-bar linkage in practice does not always move according to design. The piezo also would not always be attached perfectly perpendicularly with the top of the 4-bar linkage.

For these reasons it is more accurate to use the stroke angles directly measured by video footage. However, an operational FWMAV would not have the capacity to externally monitor its motion in such a fashion, and instead would rely on the displacement of the actuator to kinematically estimate its stroke angle. Figure 59 compares the optical and kinematic stroke angles of the 50, 55, and 60 mm wings.

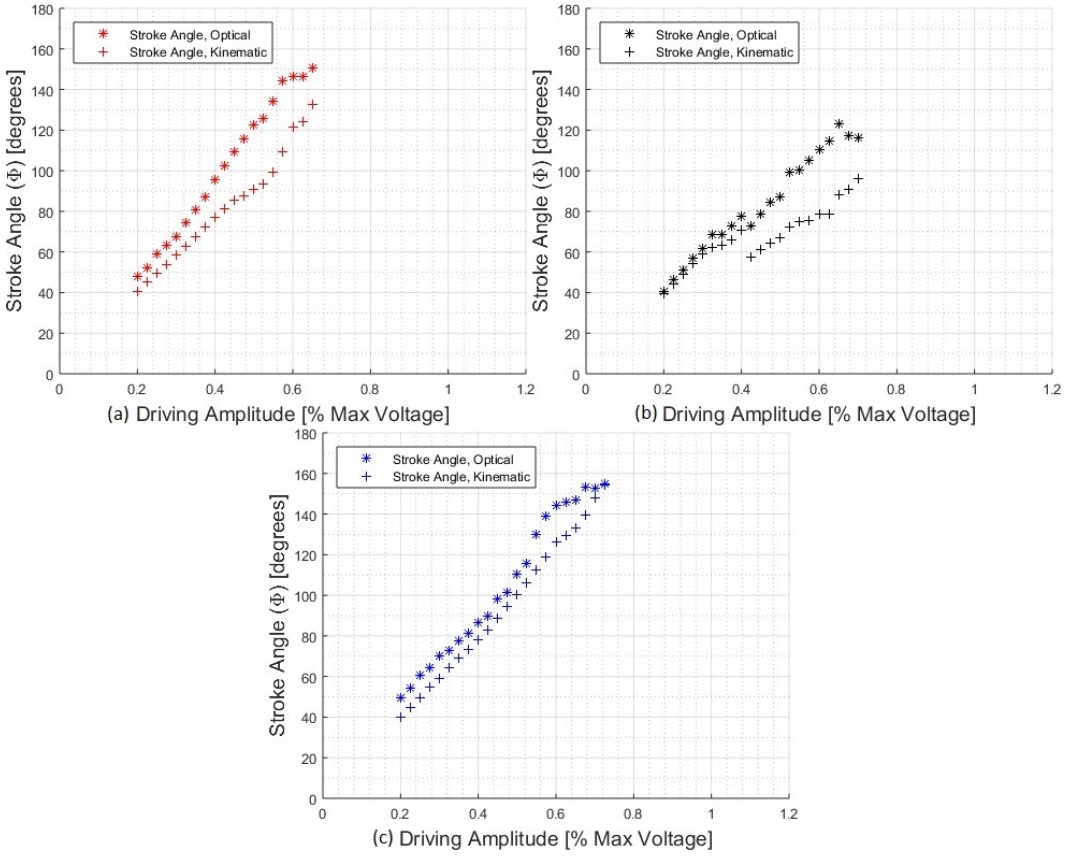

Figure 59. Driving Amplitude vs Optical and Kinematic Stroke Angle of 50 mm 17.29 Hz Wing, 55 mm 15.72 Hz Wing, and 60 mm 9.44 Wing

There is a clear pattern of the kinematic stroke angle calculation under-predicting the true stroke angle, although the extent of this discrepancy seems to vary. Figure 60 compares the two stroke angles for the case of the three separate 4-bar linkages. The same pattern continues, with the difference between kinematic and optical stroke

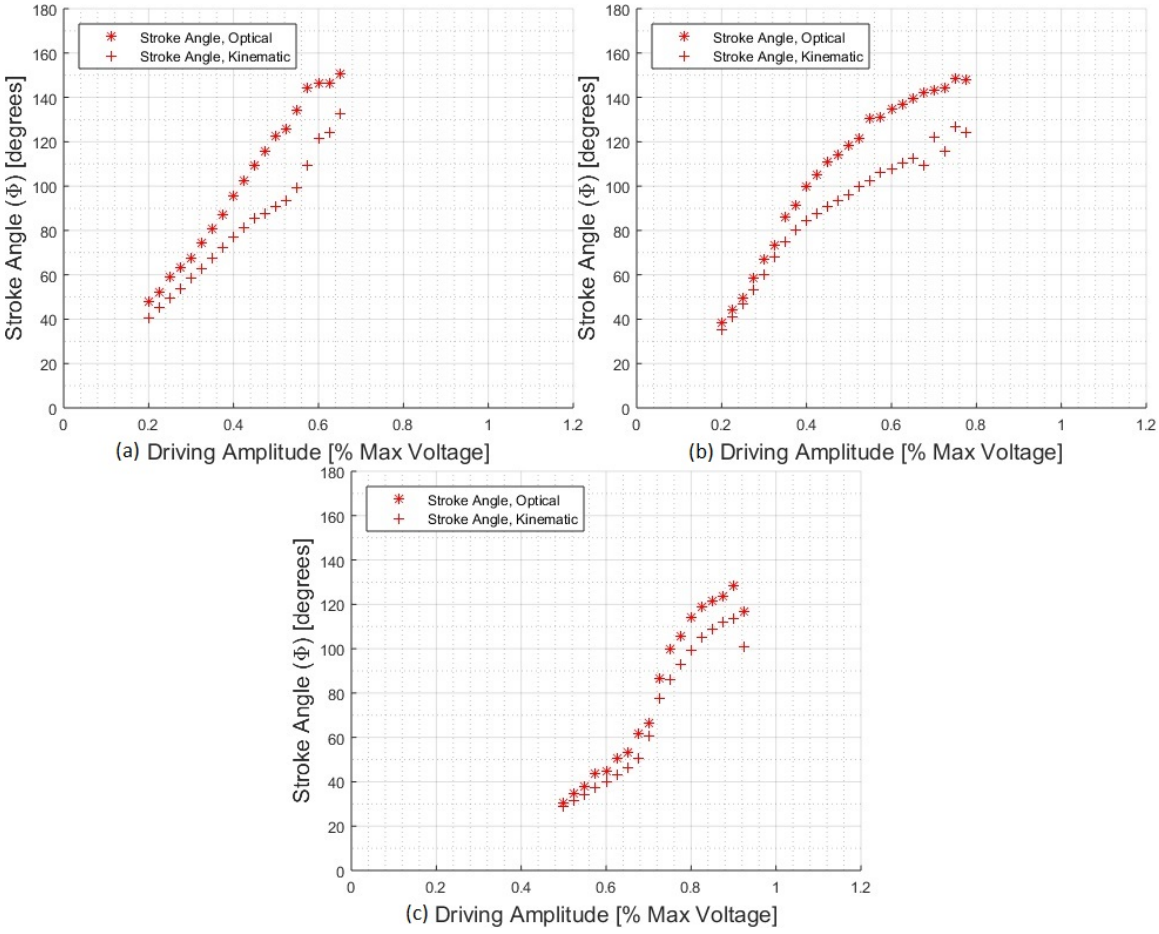

Figure 60. Driving Amplitude vs Optical and Kinematic Stroke Angle of 50 mm Wing with 12.5 μm Thick Kapton Linkage Flapping at 17.29 Hz, 25 μm Thick Kapton Linkage Flapping at 22 Hz, and 50 μm Thick Kapton Linkage Flapping at 25.9 Hz

angle becoming greater as the stroke angle is increased. Figure 61 compares the stroke angle calculations of wings of varying lengths and linkage thicknesses, while Figure 62 compares the stroke angle calculations for the partial vacuum tests.

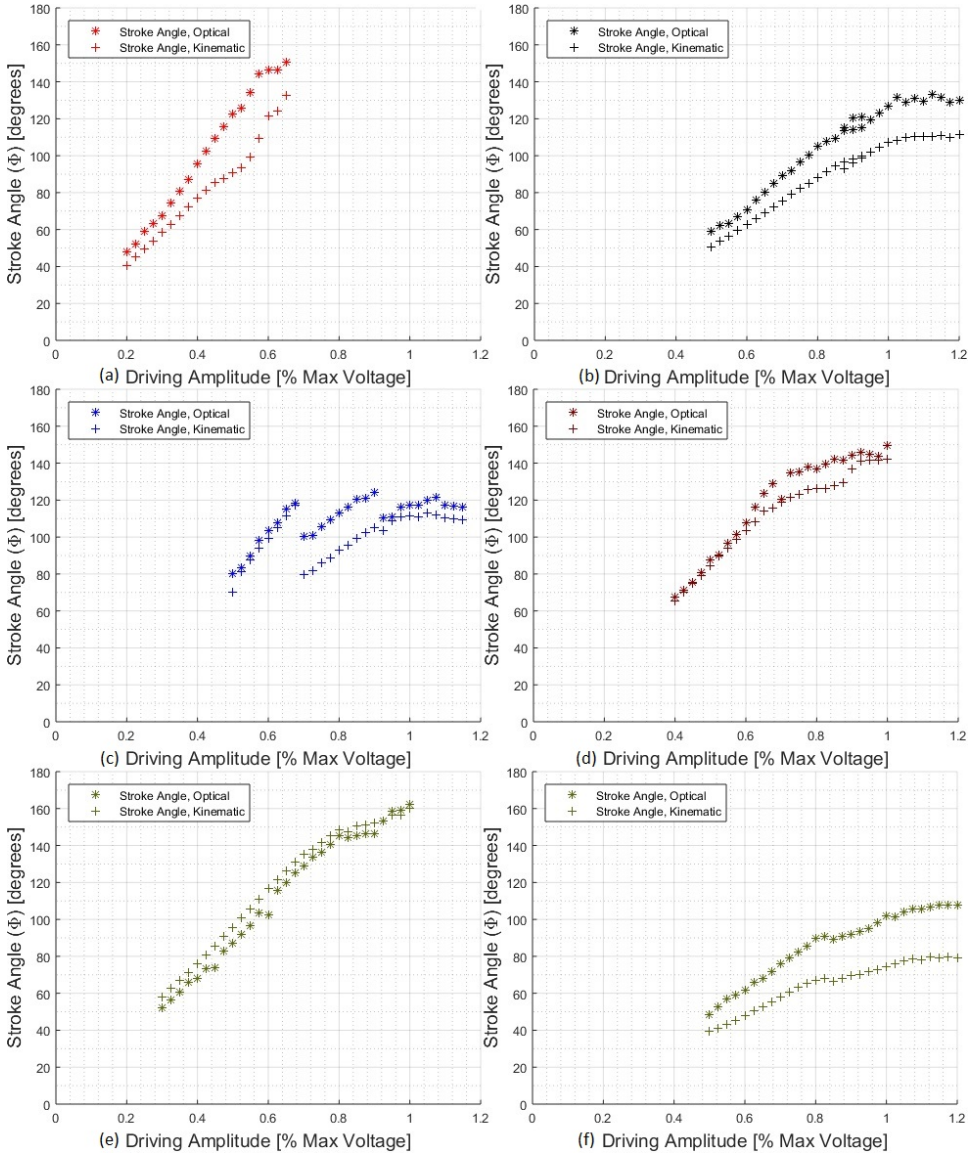

Figure 61. Driving Amplitude vs Optical and Kinematic Stroke Angle: 50 mm 17.29 Hz Wing with 12.5 μm Linkage, 55 mm 22.794 Hz Wing With 50 μm Linkage and 45 Degree Angle Stop, 60 mm 19.65-20.44 Hz Wing with 50 μm Linkage, 65 mm 11 Hz Wing with 25 μm Linkage, 70 mm 9.43 Hz Wing with 25 μm Linkage, 70 mm 15.72 Hz Wing with 50 μm Linkage

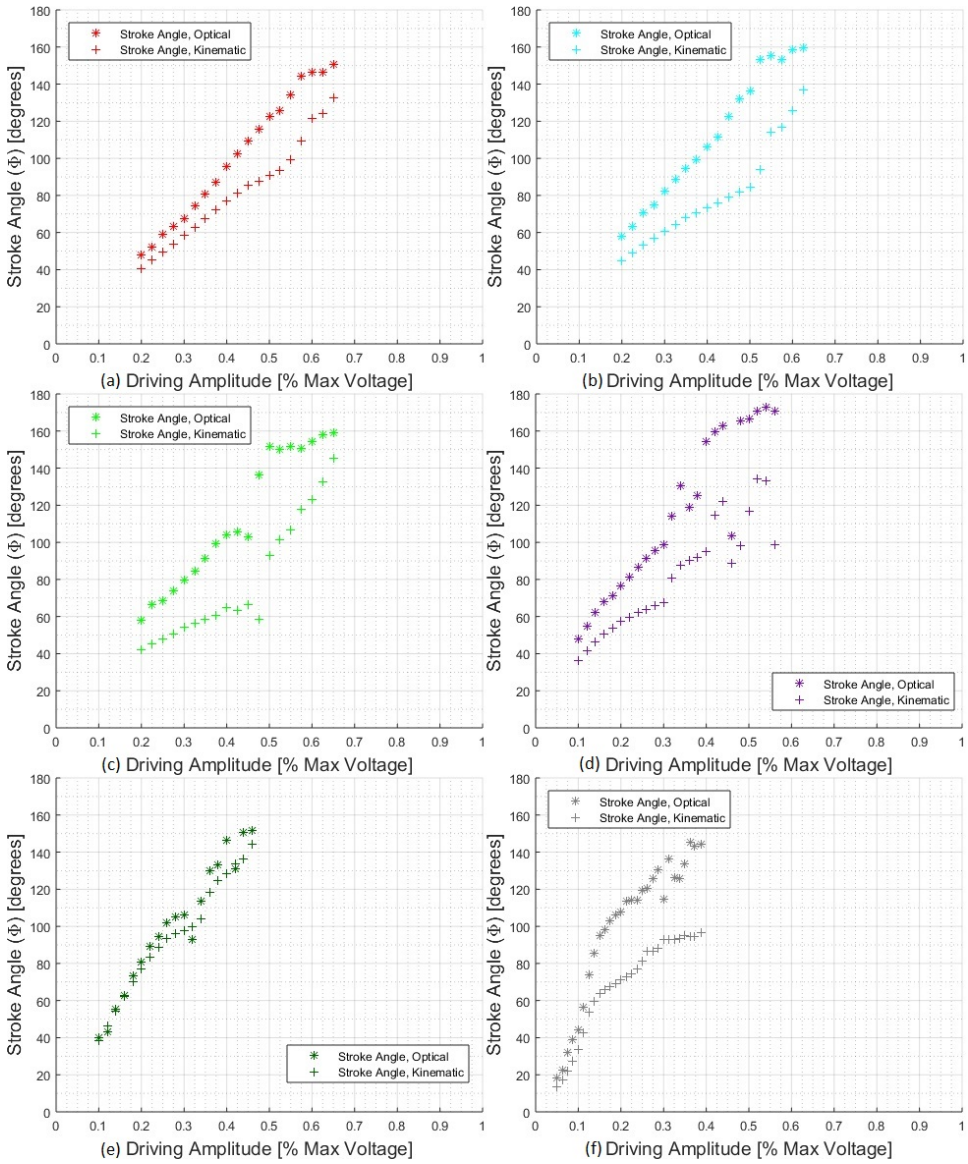

Figure 62. Driving Amplitude vs Optical and Kinematic Stroke Angle: 50 mm Wing at 100% atm and 17.29 Hz, 85% atm and 18.84 Hz, 70% atm and 18.86 Hz, 55% atm and 16.51 Hz, 40% atm and 18.08 Hz, and 25% atm and 18.05 Hz

For the 70 mm wing with the 25 μm linkage the kinematic equation overestimates the stroke angle, whereas for all other wings the reverse is true. Furthermore, the optical and kinematic stroke angles are very close for that particular design. For the vacuum tests, the correlation between the kinematic and optical stroke angles shows no clear trend. For certain cases, such as the 70% and 85% atm tests, there is a large discrepancy between the two stroke angles. However, for the 40% atm test, the two values are very close. Because the 4-bar linkage did not always operate properly under partial vacuum, the kinematic equation is less likely to correctly predict wing behavior. The stroke angle graphs for the partial vacuum tests do show the effects of biasing the wing at certain driving amplitudes to avoid non-sinusoidal flapping. This biasing had the effect of drastically increasing the stroke angle at those particular driving amplitudes, which is why the stroke angle abruptly jumps up for certain wings, to include the 70% and 55% atm tests. Figure 63 shows the two stroke angles for the 0.57% atm test. In this case the two stroke angles are relatively close. The graph also shows the previously mentioned nonlinear behavior.

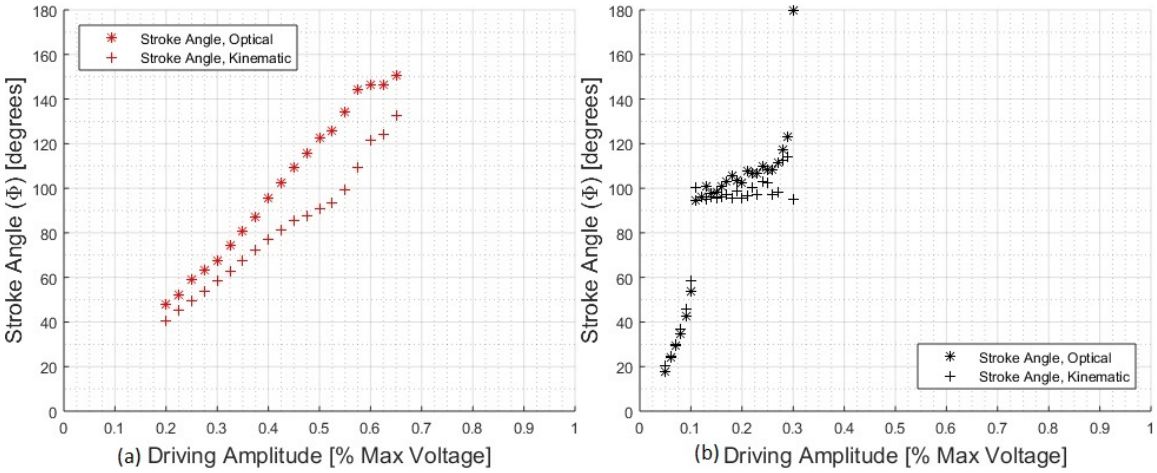

Figure 63. Driving Amplitude vs Optical and Kinematic Stroke Angle of 50 mm Wing at 100% atm and 17.29 Hz, 0.57% atm and 17.29 Hz, and 0.57% atm and 17.29 Hz with Altered Y-Axis Range

4.11 Chapter Summary

The testing conducted has given several results. First, increasing the size of the wings does lead to an increase in lift, although the 4-bar linkage must be modified to prevent the drop in natural frequency which inevitably accompanies an increase in the length and weight of the wing. Second, partial vacuum tests show the vertical force decreases as air density decreases, while the driving amplitude and power required to achieve a certain stroke angle are decreased. This suggests a FWMAV would underperform in high temperature, high altitude environments. Third, the test at absolute vacuum provided useful information regarding the power, force, and moments involved with the wing flapping under purely inertial motion. The power data shows the vast majority of the wing's power is involved with producing forces and counteracting drag, rather than powering the movement of the wing itself. The force and moment data shows very little effect from pure inertial wing motion, suggesting all of the Nano-17 data can be attributed to aerodynamic effects. Fourth, the Reynolds number has been definitively shown to have a direct linear correlation with the vertical force. The non-dimensionalized vertical force coefficient shows less of a consistent relationship with Reynolds number, although it does tend to maximize at a Reynolds number of between 500 and 1200.

V. Conclusion

5.1 Summary

The research conducted and presented in this document represents a significant contribution to the understanding of the aerodynamics of the *Manduca Sexta* inspired biomimetic wing. Valuable data was collected and various conclusions were reached regarding flapping wing flight. The goal of the testing was the following:

The objective of this research is to gain further understanding of the aerodynamics of the Manduca Sexta wing by measuring the performance of the wing in variable air density tests and with varying wing spans.

The research process involved several steps. First, a thorough literature review was conducted to understand the state of FWMAV technology as well as gain familiarity with the research conducted specifically at AFIT in the preceding years. The literature review provided a general outline of the advancements made in understanding the aerodynamics, stability and control, and mechanical construction of FWMAVs. The successful efforts at AFIT to produce easily fabricated biomimetic wings, characterize the aerodynamic performance of the wing, and explore open and closed loop control of FWMAVs was also studied.

After conducting the literature review it was determined several questions remained regarding the performance of the AFIT wing. Three particular questions which were raised were the effect of Reynolds number on the wing, the possibility of enlarging the wing to produce increased vertical force, and the impact the motion of the wing itself had on force and moment measurements, compared to the impact of aerodynamic effects. All three questions could be answered by separately varying the air density and characteristic length of the wing. First, tests were conducted in which the length of the wing was increased from 50 mm to 55, 60, 65, and 70 mm.

The aspect ratio of the wing was maintained so only one variable was altered for the tests. Second, tests were conducted in which the air density was indirectly altered by lowering the air pressure to 85, 70, 55, 40, 25, and 0.57% of atmospheric pressure.

The aforementioned tests provided invaluable data which addressed the issues poised in the thesis statement. The variable wing length tests showed increasing the characteristic length of the wing successfully increased the vertical force produced by the wing, but only if the flapper system was redesigned to counter the drop in natural frequency which initially accompanied the increase in length. Simply increasing the length of the wing while maintaining a constant aspect ratio led to the wings flapping at lower natural frequencies. The 65 and 70 mm wings flapped at such lower frequencies that negligible vertical force was produced, despite the increase in surface area. Using thicker Kapton in the 4-bar linkage led to an increase in the natural frequency of the system, which when combined with the larger wings led to superior vertical force production, at the const of power consumption.

The test conducted near absolute vacuum proved the measured forces and moments could be almost completely attributed to the wing's interaction with the air, rather than the kinetic energy of the wing's movement. Under purely inertial wing motion, the Nano-17 force/moment transducer measured negligible force and moment production, while power consumption also remained low even at the maximum stroke angle.

Finally, the Reynolds number data collected with the variable air density and characteristic length tests showed a clear linear correlation between Reynolds number and vertical force production. This data suggests future researchers can simply use the characteristic length and natural frequency of a given wing to quickly estimate the potential vertical force production, rather than spending several hours conducting tests. This will provide invaluable time savings in future FWMAV design efforts.

5.2 Research Conclusions

The previously mentioned steps were used to answer the questions at hand regarding flapping wing behavior. Additional insights were also made. The conclusions reached are described below in detail.

1. Does increasing the length of the wing while maintaining aspect ratio lead to an increase in vertical force?

Simply increasing the length of the wing initially leads to a slight increase in vertical force, but with further increases in length leads to a decrease in vertical force. This decrease in vertical force can be attributed to the drop in natural frequency which accompanies the increase in length of the wing. The 50 mm wing flapped at 17.29 Hz, the 55 mm wing at 15.72 Hz, the 60 mm wing at 9.43 Hz, the 65 mm wing at 8.0 Hz, and the 70 mm wing at 6.5 Hz. The 55 mm wing produced 16.7% more vertical force at a stroke angle of 120 degrees. The 60 mm wing produced 41.7% less vertical force at a stroke angle of 120 degrees. The 65 and 70 mm wings produced negligible vertical force at the maximum achievable stroke angle.

2. Does increasing the flapping frequency of the original 50 mm wing lead to an increase in vertical force?

Increasing the thickness of the Kapton in the 4-bar linkage of the flapper system leads to an increase in the system stiffness and hence an increase in natural frequency. Increasing the Kapton stiffness from 12.5 μm to 25 μm while maintaining the original wing length increased the natural frequency from 17.29 Hz to 22 Hz. Increasing the Kapton stiffness from 12.5 μm to 50 μm while maintaining the original wing length increased the natural frequency from 17.29 Hz to 25.9 Hz. The wing flapping at 22 Hz produced 33.3% more vertical force at a stroke angle of 120 degrees. The wing flapping at 25.9 Hz produced 16.7% less vertical force at a stroke angle of 120 degrees. The wing flapping at 22 Hz had a 11.1% increase in power consumption at a stroke

angle of 120 degrees. The wing flapping at 25.9 Hz had a 322.2% increasein power consumption at a stroke angle of 120 degrees.

The decrease in vertical force seen with the 15.9 Hz wing can be attributed to a degradation in the flapping motion of the wing. The angle of attack of the wing approached nearly 0 degrees, and a significant vertical bouncing motion occurs. The increase in power consumption seen with this design may have been due to the power required to bend the thicker Kapton joints. It remains unclear whether the same pattern of increased power consumption would be seen if alternative methods of increasing natural frequency were used.

3. Does increasing the size of the wings while utilizing thicker Kapton in the 4-bar linkage lead to an increase in vertical force?

Combining larger wings with a modified 4-bar linkage design leads to increased vertical force production. Two designs in particular led to the greatest increase in vertical force. One was the 55 mm wing with the 50 μm thick Kapton linkage, which flapped at 22.794 Hz and utilized the 45 degree angle stop, rather than the 60 degree angle stop utilized by every other design. This design produced 96% more vertical force at a stroke angle of 105 degrees, while consuming 340% more power. The other was the 70 mm wing with the 50 μm thick Kapton linkage, which flapped at 15.72 Hz. This design produced 188% more vertical force at a stroek angle of 105 degrees, while consuming 473% more power. The larger wings produced greater vertical forces than the original wing design, and also tended to be more resistant against failure at the passive rotation joint. The increase in power consumption can be attributed to both aerodynamic interactions and the presence of thicker Kapton joints, although it is not clear which of these factors has a greater influence on the increase in power consumption.

4. Does decreasing the density of the air in which the FWMAV operates influence

its behavior in any way?

Decreasing the air density leads to a corresponding gradual decrease in the vertical force produced by the wing, as well as a gradual decrease in the power consumption. The decreased vertical force production is due to the reduced ability to produce a pressure differential between the top and bottom of the wing, while the decreased power consumption can be attributed to a decrease in drag encountered by the wing. This data suggests operational FWMAVs should be over-designed at sea level, so they may still be able to fly properly in more extreme environments. An inability to fly in low density environments would impose limits on the types of missions a FWMAV could perform.

5. What are the forces, moments, and power measurements of the wing under purely inertial motion, without any interaction with the air?

By testing the wing at 0.57% of atmospheric pressure, the behavior of the wing under purely inertial motion could be measured. Under such conditions the transducer measured virtually zero vertical, side, and axial forces. There was a similar pattern with the moments of the wing, although the roll moment did have a linear relationship with the stroke angle. However, even the maximum roll moment under inertial motion was only 4.4% of the maximum roll moment in atmospheric conditions. The maximum power consumption under inertial motion was 70 mW at a stroke angle of 180 degrees, while the original wing consumed 487 mW of power at a stroke angle of 150 degrees. The AFIT wing has been proven to be a low inertia system, in which the measured behavior of the wing can be attributed entirely to the wing's interactions with the air, rather than the motion of the wing or the piezo. This suggests reducing the weight of the wing itself is of minimal concern, due to the minimal impact the mass of the wing itself has in comparison to the wing's interaction with the air.

6. Is there a relationship between the Reynolds number of the wing and a dimen-

sionless vertical force coefficient (C_v)?

Reynolds number weakly correlates with C_v, which non-dimensionalizes vertical force with respect to dynamic pressure and planform area. C_v rises and then peaks at a Reynolds number value varying from 500 to 1200, after which it steadily declines. There is a large spread of C_v values for any particular Reynolds number value, suggesting C_v is not a useful parameter for Reynolds number analysis.

7. Is there a relationship between the Reynolds number of the wing and vertical force?

There is a clear linear relationship between Reynolds number and vertical force. The vertical force of the wing can be predicted for a given Reynolds number with an accuracy of +/- 100 mg F, which at a Reynolds number of 3000 is approximately +/- 8.3%. This suggests the performance of a wing can be quickly estimated without testing by simply knowing the natural frequency and length of the wing.

5.3 Significant Contributions

Several contributions have been made to the field of FWMAVs in the course of this work.

1. Demonstrated that the CAD images of the biomimetic *Manduca Sexta* wing designed at AFIT can be modified to create altered wing designs. This includes modifying the length and width of the wing, as well as modifying the dimensions of the passive rotation joint.

2. Showed how altering the thickness of the Kapton utilized in the 4-bar linkage alters the natural frequency of the system. Increasing the thickness of the Kapton joints leads to an increase in the natural frequency, at the expense of a slight increase in mass, an increase in power consumption, and a decrease in stroke angle range.

3. Demonstrated the ability to produce superior vertical force and longer service

life through the combination of larger wings and modified 4-bar linkages. The 65 and 70 mm wings were tested without the passive rotation joint breaking, suggesting larger wings with stiffer passive rotation joints flapping at slightly lower frequencies are a superior design to the original wing.

4. Operationalized the vacuum chamber used to conduct variable air density tests. During the course of this research an extension cable for the optoNCDT 1800 was obtained and attached to the vacuum chamber, supplementing the extension cables for the Nano-17 and the piezo. In addition, tests were conducted to verify the accuracy of the Nano-17 extension cable. Finally, procedures were established for conducting tests at a given air pressure in the vacuum chamber. The vacuum chamber remains operational for use by future researchers.

5. Showed how FWMAV performance changes in response to air density variations. Future researchers can use this data to predict the drop in performance experienced by a given FWMAV in varying air conditions, which will be invaluable in the design process.

6. Demonstrated the lack of significant forces and moments measured under purely inertial motion. This means researchers will be able to use modified piezos with the AFIT wing and still be able to confidently reference past data, since neither the motion of the wing nor the piezo has a significant influence on the forces and moments measured by the Nano-17.

7. Demonstrated the ability to predict the vertical force of the wing using Reynolds number. More specifically, this enables researchers to predict the performance of the AFIT wing using only the wing length and flapping frequency. This will enable future researchers to quickly design and predict various wing designs without performing a full test sweep for each wing.

5.4 Recommendations for Future Research

The conducted research effort was limited, in the sense that it increased the planform area and length of the wing and subsequently thickened the Kapton in the 4-bar linkage as an attempt to maintain an adequate natural frequency. This attempt was successful, but with the undesirable effects of a decreased maximum stroke angle and lower power efficiency. Several aspects of the flapper mechanism could be altered by future researchers in order to maximize natural frequency, maximize wing area, minimize weight, and minimize power consumption.

The wing could be improved by altering the cross-sectional geometry of the veins, altering the venation pattern, changing the aspect ratio, using stiffer carbon fiber, and optimizing the passive rotation joint and angle stops. The 4-bar linkage could be improved by optimizing for the Kapton thickness and L_3 length. The piezo could be optimized by altering the length, altering the cross sectional geometry, and using a less dense material. A system level optimization effort would likely provide much greater performance for any FWMAV.

Furthermore, conducting a Reynolds number sweep by modifying the aspect ratio of the wing will provide a final and complete look at the influence Reynolds number has on the wing. If the pattern between Reynolds number and vertical force continues when aspect ratio is modified, this will provide another variable through which wing performance can be modified with predictable results.

VI. Appendix

The following tables display the stroke angle data for every test. The tables include the driving amplitude (A), bias (η), upstroke angle, downstroke angle, difference between upstroke and downstroke angle, with a positive value denoting an upstroke bias and a negative value denoting a downstroke bias, and total stroke angle (Φ).

Table 5. Driving Amplitude, Bias, and Stroke Angle of 50 mm Wing with 12.5 μm Kapton 4-Bar Linkage

A	η	Upstroke Angle	Downstroke Angle	Angle Difference	Φ (deg)
0.2	0.26	24	23.75	0.25	47.75
0.225	0.19	25	27.25	-2.25	52.25
0.25	0.18	28.75	30.5	-1.75	59.25
0.275	0.16	30	33.25	-3.25	63.25
0.3	0.13	34	33.5	0.5	67.5
0.325	0.11	37	37.5	-0.5	74.5
0.35	0.1	41	40	1	81
0.375	0.09	43.25	43.75	-0.5	87
0.4	0.085	48	47.5	0.5	95.5
0.425	0.085	50	52.5	-2.5	102.5
0.45	0.085	54.5	55	-0.5	109.5
0.475	0.089	57.5	58	-0.5	115.5
0.5	0.095	59	63.5	-4.5	122.5
0.525	0.1	60.5	65	-4.5	125.5
0.55	0.11	61.5	72.5	-11	134
0.575	0.11	72	72.5	-0.5	144.5
0.6	0.12	73.75	72.5	1.25	146.25
0.625	0.15	74	72.5	1.5	146.5
0.65	0.16	78	72.5	5.5	150.5

Table 6. Driving Amplitude, Bias, and Stroke Angle of 50 mm Wing with 25 μm Kapton 4-Bar Linkage

A	η	Upstroke Angle	Downstroke Angle	Angle Difference	Φ (deg)
0.2	-0.3	18.75	19.5	-0.75	38.25
0.225	-0.24	22.25	21.75	0.5	44
0.25	-0.2	24.5	25	-0.5	49.5
0.275	-0.17	29	29.5	-0.5	58.5
0.3	-0.17	33.5	33.5	0	67
0.325	-0.17	37	36.5	0.5	73.5
0.35	-0.18	44	42	2	86
0.375	-0.17	47	44.5	2.5	91.5
0.4	-0.17	50.5	49.5	1	100
0.425	-0.16	52.5	52.5	0	105
0.45	-0.16	57	54	3	111
0.475	-0.15	58.25	56	2.25	114.25
0.5	-0.15	60	58.25	1.75	118.25
0.525	-0.14	61.25	60.5	0.75	121.75
0.55	-0.14	66.25	64	2.25	130.25
0.575	-0.12	65.5	65.5	0	131
0.6	-0.115	68.75	66	2.75	134.75
0.625	-0.105	70.5	66.5	4	137
0.65	-0.095	69.25	70	-0.75	139.25
0.675	-0.095	72	70	2	142
0.7	-0.05	73.25	70	3.25	143.25
0.725	-0.057	72	72.5	-0.5	144.5
0.75	-0.04	75.5	72.5	2.75	148.25
0.775	-0.035	76.25	71.5	4.75	147.75

Table 7. Driving Amplitude, Bias, and Stroke Angle of 50 mm Wing with 50 μm Kapton 4-Bar Linkage

A	η	Upstroke Angle	Downstroke Angle	Angle Difference	Φ (deg)
0.5	0.1	15	15.5	-0.5	30.5
0.525	0.15	16	18.5	-2.5	34.5
0.55	0.15	17.25	20.5	-3.25	37.75
0.575	0.13	21	22.5	-1.5	43.5
0.6	0.12	23	21.75	1.25	44.75
0.625	0.11	24	26.5	-2.5	50.5
0.65	0.1	25.5	27.5	-2	53
0.675	0.09	30.25	31.5	-1.25	61.75
0.7	0.08	33.25	33.25	0	66.5
0.725	0.1	43.5	43	0.5	86.5
0.75	0.08	49.5	50.5	-1	100
0.775	0.07	54	51.5	2.5	105.5
0.8	0.05	58.5	55.75	2.75	114.25
0.825	0.02	59.5	59.5	0	119
0.85	0.01	61.5	60	1.5	121.5
0.875	-0.01	64	59.5	4.5	123.5
0.9	-0.02	66	62.25	3.75	128.25
0.925	-0.06	59	57.5	1.5	116.5

Table 8. Driving Amplitude, Bias, and Stroke Angle of 55 mm Wing with 12.5 μm Kapton 4-bar Linkage

A	η	Upstroke Angle	Downstroke Angle	Angle Difference	ϕ (deg)
0.2	0.29	20	20.75	-0.75	40.75
0.225	0.23	22	24.5	-2.5	46.5
0.25	0.19	23.75	27.5	-3.75	51.25
0.275	0.14	27.5	29.5	-2	57
0.3	0.1	30.5	31.25	-0.75	61.75
0.325	0.08	34	34.5	-0.5	68.5
0.35	0.05	32.5	36	-3.5	68.5
0.375	0.03	35	38	-3	73
0.4	0.04	37	40.5	-3.5	77.5
0.425	0.05	37	36	1	73
0.45	0.06	37.5	41	-3.5	78.5
0.475	0.05	40.5	43.75	-3.25	84.25
0.5	0.04	42.5	44.75	-2.25	87.25
0.525	0.063	49	50	-1	99
0.55	0.073	48.75	51.75	-3	100.5
0.575	0.073	50	55	-5	105
0.6	0.073	54.5	56	-1.5	110.5
0.625	0.062	52	62.5	-10.5	114.5
0.65	0.08	50.5	72.75	-22.25	123.25
0.675	0.12	45	72.5	-27.5	117.5
0.7	0.12	43.5	72.5	-29	116

Table 9. Driving Amplitude, Bias, and Stroke Angle of 55 mm Wing with 50 μm Kapton 4-Bar Linkage

A	η	Upstroke Angle	Downstroke Angle	Angle Difference	Φ (deg)
0.5	-0.05	-2	28.5	30.5	59
0.525	-0.05	0.75	31.5	30.75	62.25
0.55	-0.05	1.75	32.5	30.75	63.25
0.575	-0.05	1	34	33	67
0.6	-0.02	0.5	35.5	35	70.5
0.625	-0.03	2	39	37	76
0.65	-0.03	1	40.5	39.5	80
0.675	-0.03	2	43.5	41.5	85
0.7	-0.03	2	45.5	43.5	89
0.725	-0.035	0	46	46	92
0.75	-0.035	-0.5	48	48.5	96.5
0.775	-0.035	0.5	50.5	50	100.5
0.8	-0.037	0	52.5	52.5	105
0.825	-0.038	0.5	54	53.5	107.5
0.85	-0.043	1.5	55.5	54	109.5
0.875	-0.043	3.5	58.5	55	113.5
0.9	-0.043	2	58	56	114
0.925	-0.043	0	57.5	57.5	115
0.875	0.005	2	58.5	56.5	115
0.9	0.002	1.5	61	59.5	120.5
0.925	0	2	61.5	59.5	121
0.95	-0.043	3.5	61.5	58	119.5
0.975	-0.003	2	62.5	60.5	123
1.0	-0.003	1	64	63	127
1.025	-0.001	0.5	66	65.5	131.5
1.05	0.005	2	65.5	63.5	129
1.075	0.008	3	67	64	131
1.1	0.03	2.75	66	63.25	129.25
1.125	0.05	2	67.5	65.5	133
1.15	0.05	2.5	67	64.5	131.5
1.175	0.09	3	66	63	129
1.2	0.1	0	65	65	130

Table 10. Driving Amplitude, Bias, and Stroke Angle of 60 mm Wing with 12.5 μm Kapton 4-Bar Linkage

A	η	Upstroke Angle	Downstroke Angle	Angle Difference	Φ (deg)
0.2	-0.02	24	25.75	-1.75	43.75
0.225	-0.03	27	27.25	-0.25	54.25
0.25	-0.04	30	30.75	-0.75	60.75
0.275	-0.05	32	32.5	-0.5	64.5
0.3	-0.05	35	35	0	70
0.325	-0.05	37	36	1	73
0.35	-0.06	39.75	37.75	2	77.5
0.375	-0.06	41	40.5	0.5	81.5
0.4	-0.06	43.5	43	0.5	86.5
0.425	-0.06	44.5	45.5	-1	90
0.45	-0.058	49	49	0	98
0.475	-0.061	50.5	51	-0.5	101.5
0.5	-0.06	54.5	56	-1.5	110.5
0.525	-0.06	56.75	58.75	-2	115.5
0.55	-0.059	63.5	66.5	-3	130
0.575	-0.059	69.5	69.5	0	139
0.6	-0.06	73	71.25	1.75	144.25
0.625	-0.06	75	70.75	4.25	145.75
0.65	-0.06	76.5	70.5	6	147
0.675	-0.06	82	71.25	10.75	153.25
0.7	-0.06	81	71.5	9.5	152.5
0.725	-0.06	82.5	72.5	10	155

Table 11. Driving Amplitude, Bias, and Stroke Angle of 60 mm Wing with 50 μm Kapton 4-Bar Linkage

A	η	Upstroke Angle	Downstroke Angle	Angle Difference	Φ (deg)
0.5	0.15	39	41.25	-2.25	80.25
0.525	0.07	42	41.5	0.5	83.5
0.55	0.05	45	45	0	90
0.575	0.06	48	50	-2	98
0.6	0.04	51	52.5	-1.5	103.5
0.625	0.04	53	54.5	-1.5	107.5
0.65	0.02	58.5	56.75	1.75	115.25
0.675	0.02	60.5	58	2.5	118.5
0.7	-0.1	49	51.5	-2.5	100.5
0.725	-0.13	51.5	49.5	2	101
0.75	-0.13	53.25	52.5	0.75	105.75
0.775	-0.13	53.5	56	-2.5	109.5
0.8	-0.13	57	56.25	0.75	113.25
0.825	-0.14	59	57	2	116
0.85	-0.15	61	59.5	1.5	120.5
0.875	-0.15	61	60	1	121
0.9	-0.15	63.5	60.5	3	124
0.925	-0.1	56	54.25	1.75	110.25
0.95	-0.07	56	55	1	111
0.975	-0.06	59	57	2	116
1.0	-0.06	58	59.5	-1.5	117.5
1.025	-0.08	58	59.5	-1.5	117.5
1.05	-0.065	58	62	-4	120
1.075	-0.065	60.5	61	-0.5	121.5
1.1	-0.05	59	58	1	117
1.125	-0.03	56.5	60	-3.5	116.5
1.15	-0.02	58.5	57.5	1	116

Table 12. Driving Amplitude, Bias, and Stroke Angle of 65 mm Wing with 25 μm Kapton 4-Bar Linkage

A	η	Upstroke Angle	Downstroke Angle	Angle Difference	Φ (deg)
0.4	-0.23	34.5	33.25	1.25	67.75
0.425	-0.2	35.25	35.75	-0.5	71
0.45	-0.2	37	38.5	-1.5	75.5
0.475	-0.2	40.5	40	0.5	80.5
0.5	-0.19	44.25	43.5	0.75	87.75
0.525	-0.18	45	45.5	-0.5	90.5
0.55	-0.18	48.5	48	0.5	96.5
0.575	-0.17	51	50.25	0.75	101.25
0.6	-0.16	54.25	53.25	1	107.5
0.625	-0.15	58.5	57.75	0.75	116.25
0.65	-0.12	62	61.5	0.5	123.5
0.675	-0.12	64.5	64.5	0	129
0.7	-0.117	60.25	60	0.25	120.25
0.725	-0.114	67.25	67.5	-0.25	134.75
0.75	-0.114	68.25	67.25	1	135.5
0.775	-0.107	70	67.75	2.25	137.75
0.8	-0.105	70.75	66	4.75	136.75
0.825	-0.1	72.25	67.25	5	139.5
0.85	-0.09	73	69.25	3.75	142.25
0.875	-0.08	73	68.75	4.25	141.75
0.9	-0.05	73.5	70.75	2.75	144.25
0.925	-0.02	73.25	72.5	0.75	145.75
0.95	-0.01	72.5	72.5	0.25	144.75
0.975	0	71	72.5	-1.5	143.5
1.0	0.02	77	72.5	4.5	149.5

Table 13. Driving Amplitude, Bias, and Stroke Angle of 70 mm Wing with 25 μm Kapton 4-Bar Linkage

A	η	Upstroke Angle	Downstroke Angle	Angle Difference	Φ (deg)
0.3	0.25	25	27	-2	52
0.325	0.2	28	28.5	-0.5	56.5
0.35	0.2	29.75	30.75	-1	60.5
0.375	0.2	32	34	-2	66
0.4	0.2	33.25	35	-1.75	68.25
0.425	0.2	36	37.5	-1.5	73.5
0.45	0.18	34	40	-6	74
0.475	0.18	40.5	42.5	-2	83
0.5	0.18	42.75	44.5	-1.75	87.25
0.525	0.17	44.5	47.5	-3	92
0.55	0.16	47.25	49.5	-2.25	96.75
0.575	0.17	50.75	52.75	-2	103.5
0.6	0.18	51.75	50.5	1.25	102.25
0.625	0.17	56.75	59	-2.25	115.75
0.65	0.175	58.5	61.5	-3	120
0.675	0.18	60.5	64.5	-4	125
0.7	0.175	61.5	67.5	-6	129
0.725	0.17	65	68.75	-3.75	133.75
0.75	0.165	66	70.5	-4.5	136.5
0.775	0.165	69	71.75	-2.75	140.75
0.8	0.162	70.5	75	-4.5	145.5
0.825	0.154	72.5	71.75	0.75	144.25
0.85	0.16	73	72.25	0.75	145.25
0.875	0.163	74	72.5	1.5	146.5
0.9	0.163	74	72.5	1.5	146.5
0.925	0.12	82	71.5	10.5	153.5
0.95	0.05	86	72.5	13.25	158.75
0.975	0.03	87	72.5	14.75	159.25
1.0	0	90	72.5	17.5	162.5

Table 14. Driving Amplitude, Bias, and Stroke Angle of 70 mm Wing with 50 μm Kapton 4-Bar Linkage

A	η	Upstroke Angle	Downstroke Angle	Angle Difference	Φ (deg)
0.5	-0.08	24	24.5	-0.5	48.5
0.525	-0.08	25.75	27	-1.25	52.75
0.55	-0.11	28	28.75	-0.75	56.75
0.575	-0.12	29.5	29.5	0	59
0.6	-0.14	31	30.5	0.5	61.5
0.625	-0.14	32.5	33.25	-0.75	65.75
0.65	-0.14	34	34	0	68
0.675	-0.15	36	35.5	0.5	71.5
0.7	-0.15	38.75	37	1.75	75.75
0.725	-0.16	39.75	39.25	0.5	79
0.75	-0.16	41.5	41	0.5	82.5
0.775	-0.17	42.75	42.5	0.25	85.25
0.8	-0.18	45	44.5	0.5	89.5
0.825	-0.18	45.25	45.75	-0.5	91
0.85	-0.19	45.5	43.75	1.75	89.25
0.875	-0.19	46	44.75	1.25	90.75
0.9	-0.19	46	46	0	92
0.925	-0.19	46.5	46.75	-0.25	93.25
0.95	-0.2	47.75	47.5	0.25	95.25
0.975	-0.2	49.5	48.75	0.75	98.25
1.0	-0.2	50.75	51.25	-0.5	102
1.025	-0.2	51.75	49.5	2.25	101.25
1.05	-0.2	52.25	51.75	0.5	104
1.075	-0.2	53.5	52	1.5	105.5
1.1	-0.2	53.75	51.75	2	105.5
1.125	-0.19	53.75	52.75	1	106.5
1.15	-0.195	54	53.75	0.25	107.75
1.175	-0.19	54.5	53.25	1.25	107.75
1.2	-0.17	55	52.75	2.25	107.75

Table 15. Driving Amplitude, Bias, and Stroke Angle of Wing at 85% of Atmospheric Pressure

A	η	Upstroke Angle	Downstroke Angle	Angle Difference	Φ (deg)
0.2	0.34	29.5	28.5	1	58
0.225	0.28	32.75	30.5	2.25	63.25
0.25	0.26	36	34.75	1.25	70.75
0.275	0.25	37.5	37.5	0	75
0.3	0.21	42	40.25	1.75	82.25
0.325	0.2	45.25	43.5	1.75	88.75
0.35	0.19	46.5	48.25	-1.75	94.75
0.375	0.18	49.5	49.5	0	99
0.4	0.17	53	53	0	106
0.425	0.16	54.25	57	-2.75	111.25
0.45	0.155	60.5	62.25	-1.75	122.75
0.475	0.153	70	62	8	132
0.5	0.15	66	70.5	-4.5	136.5
0.525	0.147	81	72.5	8.5	153.5
0.55	0.147	82.75	72.5	10.25	155.25
0.575	0.147	81	72.5	8.5	153.5
0.6	0.147	86	72.5	13.5	158.5
0.625	0.147	87.25	72.5	14.75	159.75

Table 16. Driving Amplitude, Bias, and Stroke Angle of wing at 70% of Atmospheric Pressure

A	η	Upstroke Angle	Downstroke Angle	Angle Difference	Φ (deg)
0.2	0.08	28.5	29.5	-1	58
0.225	0.08	33.5	33	0.5	66.5
0.25	0.1	34.75	34	0.75	68.75
0.275	0.12	37	37	0	74
0.3	0.14	39	40.75	-1.75	79.75
0.325	0.15	42	42.25	-0.25	84.25
0.35	0.16	45	46.5	-1.5	91.5
0.375	0.17	49.5	50	-0.5	99.5
0.4	0.19	50	54.25	-4.25	104.25
0.425	0.18	52	53.75	-1.75	105.75
0.45	0.18	54.5	48.5	6	103
0.475	0.18	68.5	68	0.5	136.5
0.5	0.18	79.25	72.5	6.75	151.75
0.525	0.18	77.5	72.5	5	150
0.55	0.18	79	72.5	6.5	151.5
0.575	0.18	78	72.5	5.5	150.5
0.6	0.18	82	72.5	9.5	154.5
0.625	0.18	85.5	72.5	13	158
0.65	0.18	86.5	72.5	14	159

Table 17. Driving Amplitude, Bias, and Stroke Angle of Wing at 55% of Atmospheric Pressure

A	η	Upstroke Angle	Downstroke Angle	Angle Difference	Φ (deg)
0.1	0.15	24.25	23.5	0.75	47.75
0.12	0.09	29	26	3	55
0.14	0.06	31.75	30.25	1.5	62
0.16	0.03	35.25	33	2.25	68.25
0.18	0.02	36.25	34.75	1.5	71
0.2	0.02	38.5	38	0.5	76.5
0.22	0.01	42.5	39	3.5	81.5
0.24	0.04	44.5	42.25	2.25	86.75
0.26	0.03	47	44.5	2.5	91.5
0.28	0.04	48.5	47	1.5	95.5
0.3	0.04	49	49.5	-0.5	98.5
0.32	0.04	56	58	-2	114
0.34	0.07	68.5	62	6.5	130.5
0.36	0.07	59	60	-1	119
0.38	0.07	68.5	56.5	12	125
0.4	0.07	82	72.5	9.5	154.5
0.42	0.07	87.25	72.5	14.75	159.75
0.44	0.07	90.5	72.5	18	163
0.46	0.07	61	42.5	18.5	103.5
0.48	0.07	93	72.5	20.5	165.5
0.5	0.07	94	72.5	21.5	166.5
0.52	0.07	98	72.5	25.5	170.5
0.54	0.07	100.5	72.5	28	173
0.56	0.07	98.5	72.5	26	171

Table 18. Driving Amplitude, Bias, and Stroke Angle of Wing at 40% of Atmospheric Pressure

A	η	Upstroke Angle	Downstroke Angle	Angle Difference	Φ (deg)
0.1	0.2	18	22	-4	40
0.12	0.04	21	22	-1	43
0.14	0	25.25	30	-4.75	55.25
0.16	-0.04	32	31	1	63
0.18	-0.04	36.5	37	-0.5	73.5
0.2	-0.04	39	41.5	-2.5	80.5
0.22	-0.04	44.5	44.5	0	89
0.24	-0.03	44.5	50.25	-5.75	94.75
0.26	0	49.25	52.5	-3.25	101.75
0.28	0	51	54	-3	105
0.3	0.01	50	56.25	-6.25	106.25
0.32	0.025	46	47	-1	93
0.34	0.04	54.5	59	-4.5	113.5
0.36	0.2	57.25	72.5	-15.25	129.75
0.38	0.2	60.75	72.5	-11.75	133.25
0.4	0.2	74	72.5	1.5	146.5
0.42	0.2	58.5	72.5	-14	131
0.44	0.2	78	72.5	5.5	150.5
0.46	0.2	79	72.5	6.5	151.5

Table 19. Driving Amplitude, Bias, and Stroke Angle of Wing at 25% of Atmospheric Pressure

A	η	Upstroke Angle	Downstroke Angle	Angle Difference	Φ (deg)
0.05	1	13.25	5	8.25	18.25
0.0625	1	13.5	9	4.5	22.5
0.075	1	16.25	16	0.25	32.25
0.0875	0.85	18.25	20.5	-2.25	38.75
0.1	0.62	22.75	21.25	1.5	44
0.1125	0.55	28	28.25	-0.25	56.25
0.125	0.55	35.5	38.5	-3	74
0.1375	0.56	41.5	44	-2.5	85.5
0.15	0.56	46.75	48.5	-1.75	95.25
0.1625	0.52	48.75	49.5	-0.75	98.25
0.175	0.51	51	52	-1	103
0.1875	0.5	53.5	52.5	1	106
0.2	0.49	54.75	53	1.75	107.75
0.2125	0.47	58	55.5	2.5	113.5
0.225	0.44	61	53	8	114
0.2375	0.46	55	59	-4	114
0.25	0.47	57.5	62	-4.5	119.5
0.2625	0.49	48	72.5	-24.5	120.5
0.275	0.5	53	72.5	-19.5	125.5
0.2875	0.5	58	72.5	-14.5	130.5
0.3	0.5	42	72.5	-30.5	114.5
0.3125	0.5	64	72.5	-8.5	136.5
0.325	0.5	53.5	72.5	-19	126
0.3375	0.5	53	72.5	-19.5	125.5
0.35	0.5	61.25	72.5	-11.25	133.75
0.3625	0.5	73	72.5	0.5	145.5
0.3725	0.5	70.5	72.5	-2	143
0.3875	0.5	72	72.5	-0.5	144.5

Table 20. Driving Amplitude, Bias, and Stroke Angle of Wing at 0.57% of Atmospheric Pressure

A	η	Upstroke Angle	Downstroke Angle	Angle Difference	Φ (deg)
0.05	1	16	2	14	18
0.06	1	16.5	7.75	8.75	24.25
0.07	1	19.25	10	9.25	29.25
0.08	1	20.25	14.25	6	34.5
0.09	1	22.5	20	2.5	42.5
0.1	0.7	28	26	2	54
0.11	0.8	47.5	46.75	0.75	94.25
0.12	0.74	48.5	47.75	0.75	96.25
0.13	0.68	49	52	-3	101
0.14	0.64	47.5	50	-2.5	97.5
0.15	0.55	47.5	50.5	-3	98
0.16	0.52	50	51	-1	101
0.17	0.49	50.5	52.5	-2	103
0.18	0.46	52.5	53	-0.5	105.5
0.19	0.43	51	52.5	-1.5	103.5
0.2	0.41	49.5	52.75	-3.25	102.25
0.21	0.39	52.5	55	-2.5	107.5
0.22	0.36	51.5	55.25	-3.75	106.75
0.23	0.34	51.5	55	-3.5	106.5
0.24	0.34	50	60	-10	110
0.25	0.31	53	55.5	-2.5	108.5
0.26	0.26	53	55	-2	108
0.27	0.285	50.25	61	-10.75	111.25
0.28	0.35	49	68.5	-19.5	117.5
0.29	0.35	52	71	-19	123
0.3	-0.2	109	71	38	180

Bibliography

1. Michael L Anderson. Design and control of flapping wing micro air vehicles. Technical report, DTIC Document, 2011.

2. Zachary R Brown. *Experimental Characterization of Wings For a Hawkmoth-Sized Micro Air Vehicle*. 2014.

3. A. Conn, S. Burgess, R. Hyde, and Chung Seng Ling. From natural flyers to the mechanical realization of a flapping wing micro air vehicle. In *Robotics and Biomimetics, 2006. ROBIO '06. IEEE International Conference on*, pages 439–444, Dec 2006.

4. James D DeLaurier and Jeremy M Harris. A study of mechanical flapping wing flight. *Aeronautical Journal*, 97:277–277, 1993.

5. Anthony M DeLuca. *Aerodynamic performance and particle image velocimetery of piezo actuated biomimetic Manduca Sexta engineered wings towards the design and application of a flapping wing flight vehicle*. 2013.

6. Charles P Ellington. Insects versus birds: the great divide. In *44th AIAA aerospace sciences meeting and exhibit*, volume 35, pages 1–6, 2006.

7. CP Ellington. The aerodynamics of hovering insect flight. i. the quasi-steady analysis. *Philosophical Transactions of the Royal Society B: Biological Sciences*, 305(1122):1–15, 1984.

8. CP Ellington. The aerodynamics of hovering insect flight. iii. kinematics. *Philosophical Transactions of the Royal Society B: Biological Sciences*, 305(1122):41–78, 1984.

9. CP Ellington. The aerodynamics of hovering insect flight. iv. aeorodynamic mechanisms. *Philosophical Transactions of the Royal Society B: Biological Sciences*, 305(1122):79–113, 1984.

10. Steven Ho, Hany Nassef, Nick Pornsinsirirak, Yu-Chong Tai, and Chih-Ming Ho. Unsteady aerodynamics and flow control for flapping wing flyers. *Progress in Aerospace Sciences*, 39(8):635–681, 2003.

11. Arthur F II Huber. Death by a thousand cuts: Micro-air vehicles in the service of air force missions.

12. KD Jones, CJ Bradshaw, J Papadopoulos, and MF Platzer. Bio-inspired design of flapping-wing micro air vehicles. *Aeronautical Journal*, 109(1098):385–394, 2005.

13. Michael Karpelson, Gu-Yeon Wei, and Robert J Wood. A review of actuation and power electronics options for flapping-wing robotic insects. In *Robotics and Automation, 2008. ICRA 2008. IEEE International Conference on*, pages 779–786. IEEE, 2008.

14. M Lasek, J Pietrucha, M Zlocka, and K Sibilski. Analogies between rotary and flapping wings from control theory point of view. In *AIAA Atmospheric Flight Mechanics Conference and Exhibit*, pages 6–9, 2001.

15. Robert K Lenzen. Development of optimized piezoelectric bending actuators for use in an insect sized flapping wing micro air vehicle. Technical report, DTIC Document, 2013.

16. Garrison J Lindholm and Richard G Cobb. Closed-loop control of a constrained, resonant-flapping micro air vehicle. *AIAA Journal*, 52(8):1616–1623, 2014.

17. Department of Defense. Unmanned systems integrated roadmap: Fy2013-2038.

18. Ryan P O'Hara. *The Characterization of Material Properties and Structural Dynamics of the Manduca Sexta Forewing for Application to Flapping Wing Micro Air Vehicle Design.* 2012.

19. Hiroto Tanaka, John P Whitney, and Robert J Wood. Effect of flexural and torsional wing flexibility on lift generation in hoverfly flight. *Integrative and comparative biology*, page icr051, 2011.

20. Dragos Viieru, Jian Tang, Yongsheng Lian, Hao Liu, and Wei Shyy. Flapping and flexible wing aerodynamics of low reynolds number flight vehicles. *AIAA paper*, 503:2006, 2006.

21. Walter G. Vincenti and Charles H. Kruger Jr. *Introduction to Physical Gas Dynamics.* Krieger Publishing Company, 1965.

22. JP Whitney and RJ Wood. Aeromechanics of passive rotation in flapping flight. *Journal of Fluid Mechanics*, 660:197–220, 2010.

23. Alexander P Willmott, Chardeles P Ellington, and Adrian LR Thomas. Flow visualization and unsteady aerodynamics in the flight of the hawkmoth, manduca sexta. *Philosophical Transactions of the Royal Society B: Biological Sciences*, 352(1351):303–316, 1997.

24. Robert J Wood. Design, fabrication, and analysis of a 3dof, 3cm flapping-wing mav. In *Intelligent Robots and Systems, 2007. IROS 2007. IEEE/RSJ International Conference on*, pages 1576–1581. IEEE, 2007.

REPORT DOCUMENTATION PAGE

Form Approved
OMB No. 0704–0188

The public reporting burden for this collection of information is estimated to average 1 hour per response, including the time for reviewing instructions, searching existing data sources, gathering and maintaining the data needed, and completing and reviewing the collection of information. Send comments regarding this burden estimate or any other aspect of this collection of information, including suggestions for reducing this burden to Department of Defense, Washington Headquarters Services, Directorate for Information Operations and Reports (0704–0188), 1215 Jefferson Davis Highway, Suite 1204, Arlington, VA 22202–4302. Respondents should be aware that notwithstanding any other provision of law, no person shall be subject to any penalty for failing to comply with a collection of information if it does not display a currently valid OMB control number. **PLEASE DO NOT RETURN YOUR FORM TO THE ABOVE ADDRESS.**

1. REPORT DATE *(DD–MM–YYYY)*	2. REPORT TYPE	3. DATES COVERED *(From — To)*
24–03–2016	Master's Thesis	Sept 2014 — Mar 2016

4. TITLE AND SUBTITLE

Investigation Into Reynolds Number Effects On A Biomimetic Flapping Wing

5a. CONTRACT NUMBER

5b. GRANT NUMBER

5c. PROGRAM ELEMENT NUMBER

6. AUTHOR(S)

Hope, Daniel K., Second Lieutenant, USAF

5d. PROJECT NUMBER

5e. TASK NUMBER

5f. WORK UNIT NUMBER

7. PERFORMING ORGANIZATION NAME(S) AND ADDRESS(ES)

Air Force Institute of Technology
Graduate School of Engineering and Management (AFIT/EN)
2950 Hobson Way
WPAFB OH 45433-7765

8. PERFORMING ORGANIZATION REPORT NUMBER

AFIT-ENY-MS-16-M-219

9. SPONSORING / MONITORING AGENCY NAME(S) AND ADDRESS(ES)

Air Force Research Laboratory Munitions Directorate
101 W. Eglin Blvd, Building 13
Eglin AFB, FL 32542

10. SPONSOR/MONITOR'S ACRONYM(S)

AFRL/RW

11. SPONSOR/MONITOR'S REPORT NUMBER(S)

12. DISTRIBUTION / AVAILABILITY STATEMENT

DISTRIBUTION STATEMENT A:
APPROVED FOR PUBLIC RELEASE; DISTRIBUTION UNLIMITED.

13. SUPPLEMENTARY NOTES

This work is declared a work of the U.S. Government and is not suject to copyright protection in the United States

14. ABSTRACT

This research investigated how the nature of the wing changed as a function of Reynolds number by measuring the forces produced by wings with varying characteristic lengths, tested at varying air densities.
Increasing the wing span increased the overall weight of the wing, which reduced the 1st natural frequency; and did not result in an increase in vertical force over the baseline 50 mm wing. However; if the decrease in natural frequency was counteracted by increasing the thickness of the joint material in the linkage mechanism, vertical force production did increase over the baseline wing planform. Negligible forces and moments were measured at vacuum conditions, where the wing was demonstrating purely inertial motion, revealing the flight forces measured in atmosphere are wholly limited to its interaction with the surrounding air. Lastly, there was clear correlation between Reynolds number and vertical force production, indicating Reynolds number is a suitable parameter to predict the expected lift production for a specific wing design.

15. SUBJECT TERMS

flapping wing micro Air vehicles, FWMAV, Reynolds Number, Manduca Sexta, piezoelectric actuators, biomimetic wing design

16. SECURITY CLASSIFICATION OF:			17. LIMITATION OF ABSTRACT	18. NUMBER OF PAGES	19a. NAME OF RESPONSIBLE PERSON
a. REPORT	b. ABSTRACT	c. THIS PAGE			Lt Col Anthony M. Deluca, AFIT/ENY
U	U	U	U	100	19b. TELEPHONE NUMBER *(include area code)* (937) 255-3636, x4537; Anthony.Deluca@afit.edu